AN INVESTIGATION OF THE

HEAT TRANSFER AND TRANSPORT MECHANISMS

WHICH CONTROL SURFACE WATER

DURING GLAZE ICE ACCRETION

by

STEPHEN RICHARD TURNOCK

B.A., Cambridge University

(1986)

SUBMITTED IN PARTIAL FULFILLMENT
OF THE REQUIREMENTS FOR THE
DEGREE OF

MASTER OF SCIENCE
IN AERONAUTICS AND ASTRONAUTICS

at the

MASSACHUSETTS INSTITUTE OF TECHNOLOGY

January 1988

© Massachusetts Institute of Technology 1988

Signature of Author_____
                        Department of Aeronautics and Astronautics
                                                January 15, 1988

Certified by_____
                                    Professor R. John Hansman
              Thesis Supervisor, Department of Aeronautics and
                                                     Astronautics

Accepted by_____
                                    Professor Harold Y. Wachman
                    Chairman, Department Graduate Committee

Aero

AN INVESTIGATION OF THE HEAT TRANSFER AND TRANSPORT
MECHANISMS WHICH CONTROL SURFACE WATER DURING GLAZE ICE ACCRETION
by
STEPHEN RICHARD TURNOCK
Submitted to the Department of Aeronautics and Astronautics
on January 15, 1988 in partial fulfillment of the
requirements for the Degree of Master of Science
in Aeronautics and Astronautics

ABSTRACT

The primary factors which control the behavior of unfrozen surface water during glaze ice accretion were isolated in a series of experiments. Detailed microvideo observations were made of glaze ice accretions on 1" diameter cylinders in a 6" square cross section closed-loop refrigerated wind tunnel. The tunnel was run at: a freestream velocity of 150 and 100 Kts; air temperature in the range of $-11^{\circ}C$ to $-4^{\circ}C$; a nominal centerline liquid water content between $0.7g/m^3$ and $1.2g/m^3$; and with a cloud droplet Mean Volumetric Diamter (MVD) of 30 microns. Distinct zones of surface water behavior were observed; a smooth wet zone in the stagnation region which had a uniform film of water, a rough zone where surface tension effects caused coalescence of surface water into stationary beads; and a zone where surface water ran back as rivulets. The location of the transition from the smooth to the rough zone was found to migrate with time towards the stagnation point. After 3 minutes exposure the final location of the smooth-rough transition depended on the icing cloud temperature, velocity and liquid water content which control the mass flow of water in the smooth zone. The greater the surface flow of water the further forward the transition.

Comparative tests studied the effect of substrate thermal properties, roughness and surface chemistry on ice accretion. There was an initial transient period of approximately 60 seconds when the effect of the substrate was important. How surface tension affects ice accretion by adding a surfactant to the icing tunnel cloud water supply. This reduced the water's surface tension and significantly altered the accreted glaze ice shape.

Measurements were made to determine the temperature variation of the contact angle and contact angle hysteresis of water droplets on ice. These were found to increase sharply at temperatures just below $0^{\circ}C$ explaining the high resistance to motion of water beads observed on accreting glaze ice surfaces. The maximum diameter of stationary water droplets when subject only to a surface shear stress was measured in 1' square wind tunnel. A power law relationship was found between the freestream velocity, surface resistance and the droplet diameter.

Based on this investigation the importance of surface water behavior to the glaze ice accretion process was demonstrated. A simple multi-zone model modification to the current glaze ice accretion model was proposed. The model incorporates discrete zones of surface water behavior, each with a characteristic surface roughness.

Thesis Supervisor: Professor R. John Hansman
            Title: Associate Professor of Aeronautics and
                    Astronautics

ACKNOWLEDGMENTS

TABLE OF CONTENTS

LIST OF FIGURES

Chapter One

Chapter Two

Chapter Three

Chapter Four

Chapter Five

Chapter Six

LIST OF TABLES

Chapter Four

Chapter Five

NOMENCLATURE

A	Surface Area, m^2
C	Experimentally Derived Constant
c_p	Specific Heat Capacity, J/KgK
d	Diameter of Droplet, m
D	Diffusion Coefficient, m^2/s
F	Force, N
h	Local Convective Heat Transfer Coefficient, W/m^2K
k	Thermal Conductivity, W/mK
k	Roughness Height, m
k_s	Equivalent Sand Grain Roughness, m

L_f	Latent Heat of Freezing, J/Kg
L_v	Latent Heat of Vaporisation, J/Kg
LWC	Liquid Water Content, g/m^3
$\dot{M}$	Mass Flux, Kg/s
MVD	Mean Volumetric Diameter, $*m$
P	Position, ^{o}
p	Pressure, N/m^2
Q	Heat Flux, W
r	Recovery Factor
R_f	Resistance Factor
s	Distance from leading edge, m
t	Thickness of Water Film, m
T	Temperature, ^oC
U	Velocity, m/s
w	Width of Droplet, m
z	Height of Droplet, m
η	Collection Efficiency
δ	Thermal Boundary Layer Thickness, m
ρ	Vapour Density, Kg/m^3
ν	Kinematic Viscosity, m^2/s
σ	Surface Tension, N/m
τ	Shear Stress, N/m^2
$\Delta\theta$	Contact Angle Hysteresis, ^{o}
θ	Contact Angle, ^{o}
θ_a	Advancing Contact Angle, ^{o} .
θ_r	Receding Contact Angle, ^{o}

Superscripts

$\cdot$	per unit time, /s
"	per unit area, /m^2

Subscripts

aero	Aerodynamic
aw	Adiabatic Wall
bulk	Bulk
cond	Conduction
conv	Convection
evap	Evaporation
flow	Flow
freeze	Freeze
imp	Impingment
in	In
lg	Liquid-Gas
out	Out
resis	Resistance
sg	Solid-Gas
sl	Solid-Liquid
sub	Sublimation
surf	Surface
∞	Freestream Value

Chapter One

1.1 Scope of Thesis

Roughness on a glaze ice surface is a result of the presence of unfrozen surface water. Current methods of modeling ice accretion ignore the physical behavior of this surface water. This is thought to be the reason for their poor performance in predicting glaze ice accretion. An investigation has therefore been made of how the behavior of unfrozen surface water on an accreting ice surface is controlled by the local heat transfer and the forces which govern the transport of water on the surface. The freezing of water to form ice is a complex process involving coupled heat and mass transfer. To isolate the parameters which are important to glaze ice formation and the resulting generation of surface roughness the approach of this thesis has been to conduct a series of small scale experiments whereby the effect of individual parameters could be isolated.

Chapter One gives a background discussion of the effect of ice accretion during flight and a description of the analytic and numeric methods used to predict ice formation. The limited accuracy of these methods for predicting ice accretion when there is surface water present on the ice surface is the motivation for this investigation.

Chapter Two presents an analysis of the local heat and mass transfer on an accreting ice surface. The individual terms contributing to the energy and mass flux balances are

discussed in relation to the influence of surface water. Essential to the evaluation of the ice accretion rate is the determination of the local convective heat transfer coefficient and its evaluation is examined in relation to the influence of surface roughness.

The microphysics which control the behavior of surface water and its influence on the surface transport of water is dealt with in Chapter Three. Four possible modes of surface transport are examined. The relative strength of the external forces acting on the water compared to the material surface resistance to motion forces will determine the particular mode that occurs. The possible external forces and the factors which control the surface resistance are detailed.

The surface resistance to motion of water can be characterised in terms of surface tension, contact angle and contact angle hysteresis. Measurements were, therefore, made of the contact angle and contact angle hysteresis of water on ice for a range of ice temperatures. Chapter Four details this experiment and also an experiment carried out to determine the maximum velocity required to dislodge droplets from a flat plate for a range of surface resistances and droplet diameters. The results obtained and observations from films made in the NASA Lewis Icing Research Tunnel were used to discuss how the freezing of stationary water beads generates surface roughness.

Chapter Five describes direct comparison experiments made in a small icing wind tunnel. The influence of the initial uniced surface's thermal and physical properties and also the

the effect of altering the water's surface tension were used to investigate how altering the factors which control the surface water affects the ice accretion. Microvideo recordings were made which allowed detailed observation of the process of ice accretion and subsequent analysis of the time dependent behavior of the ice surface.

Chapter Six uses the theoretical and experimental work of the proceeding chapters to develop a modification to current ice accretion models which includes the physical behavior of surface water observed in Chapters Four and Five. The controlling factors which govern the transient and steady state behaviour of the surface water for this model are discussed. A comparison is made to a typical ice accretion code used for glaze ice prediction.

Chapter seven contains an overall summary of the experimental results and conclusions made in this examination of surface water behavior during glaze ice accretion.

1.2 Icing on Aerospace Vehicles

The certification of aircraft for flight in icing conditions is both expensive and time consuming. The accuracy with which icing can be analytically modeled has direct impact on this process. Operation in icing conditions requires the detection and then removal or prevention of ice formation in areas which are sensitive to ice build up and ensure that in unprotected regions will not significantly affect aircraft performance.

The cloud conditions that give rise to icing are generally found at altitudes below 22,000 ft. The Federal Aviation Administration FAR 25 Appendix C details the meteorological envelope of air temperature, cloud liquid water content and droplet size distribution for flight certification for flight in icing conditions.

An icing cloud consists of a distribution of supercooled water droplets or ice particles of various size. The total amount of water present is termed the liquid water content LWC and is normally expressed in grammes per cubic meter. The droplet size distribution of water droplets is typically characterised by a mean volumetric diamter MVD. Measurements of the distributions of particle size and the resulting MVD found in various cloud environments have been made and these are used as a basis for modeling the icing environment. The actual distribution of droplets is stochastic are there are can be large variations in both LWC and MVD with position within icing clouds.

The operation of any aircraft in cloud at air temperatures close to freezing can potentially involve exposure to an icing environment. The severity of the effect of ice formation will depend on the class of aircraft and the flight regime within which it is operating.

The critical zones for ice formation are illustrated in figure 1-1 for a representative transport aircraft and helicopter.
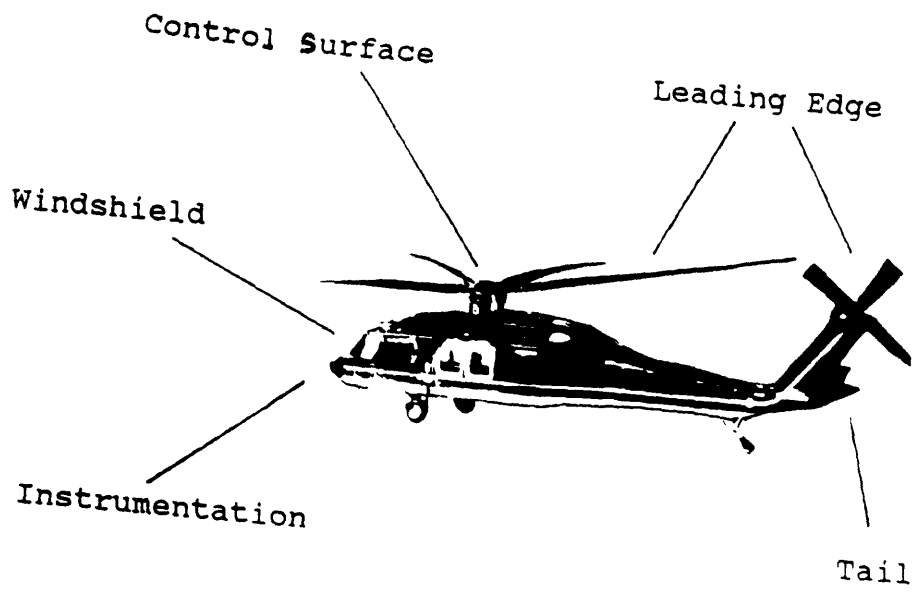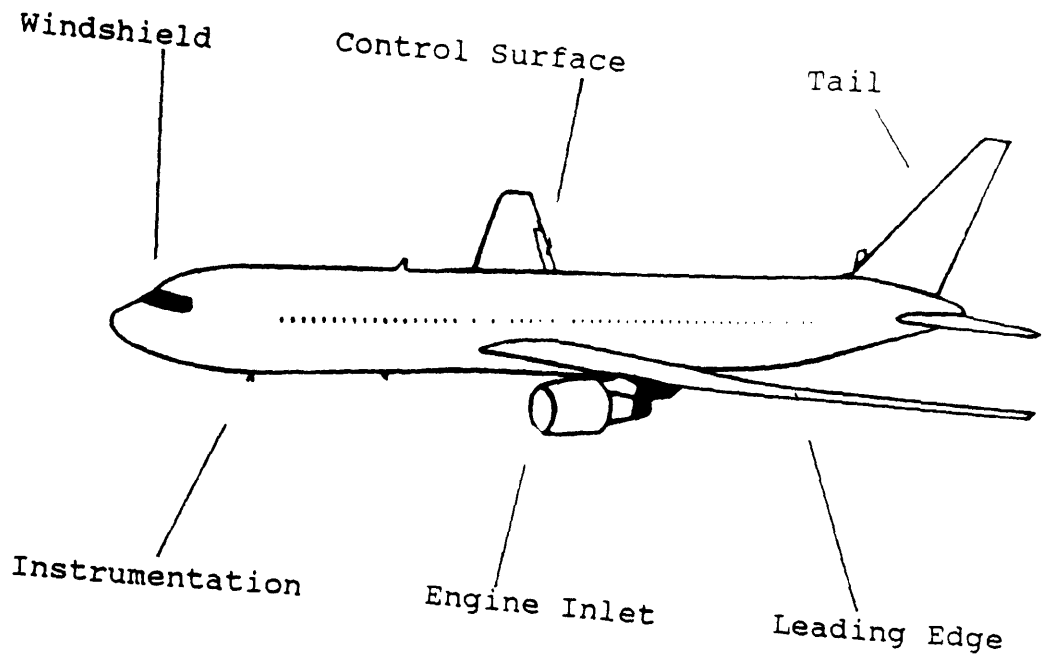
Figure 1-1   Critical Zones on Aircraft and
Rotorcraft for Ice Accretion

The major problem areas are:

(1) Engine ingestion of ice formed on the inlet cowl can seriously damage or destroy internal components leading to engine failure .

(2) Airfoil leading edge ice build up can significantly alter the stall characteristics,reduce lift and increase drag. For rotating components uneven ice build up will give rise to large out of balance forces which can potentialy cause structural failure.

(3) Control authority degradation by the locking in place of control surfaces and the formation of ice on the tail which adversly affects aircraft stability.

(4) The icing of instrumentation, windshields, and Radar may reduce the Pilots ability to fly the aircraft safely.

The ability to predict ice accretion on unprotected components and the design and evaluation of systems for the detection and removal or prevention of ice formation in the critical zones for ice accretion are the primary area in which the ability to model and artificially simulate icing is used.

1.3 Current Modeling of Ice Accretion

The initial development and testing of aircraft ice protection (passive or active) systems for use in icing conditions is conducted by wind tunnel testing, scaling from previous tests , or the analytic prediction of ice accretion using computational codes. The validity of such procedures

require that there be experimental verification between the simulated and natural conditions.

Current models [1,2] ignore the specific details of surface water behavior and the resulting surface roughness. Figure 1-2 is a schematic representation of a typical computational model of ice accretion. The correct calculation of ice accretion will require that each of the four steps; flowfield modeling, cloud droplet impingement, ice accretion rate, and ice shape generation be accurate representations of the physical process of ice formation. Errors in each process are cummulative and result in the difference between actual ice formation and the computationally predicted shape. The current methods for evaluating the first three steps are:

(1) External Flowfield

The modeling of the external flow field is evaluated using numeric solutions to the flow equations over airfoils. Panel methods [3] for solving the potential flow (inviscid, incompressible) equations using a distribution of sources or vortices located on the airfoil surface are considered adequate for calculating the velocity in the far field. However, more sophisticated methods can be used but are computationally time consuming for the extra accuracy obtained. The external flowfield is necessary for the calculation of the individual cloud droplet trajectories.

(2) Impinging Mass Flux

The mass flux of impinging supercooled water droplets arriving at the surface of a body exposed to icing conditions results from the displacements of the cloud particles
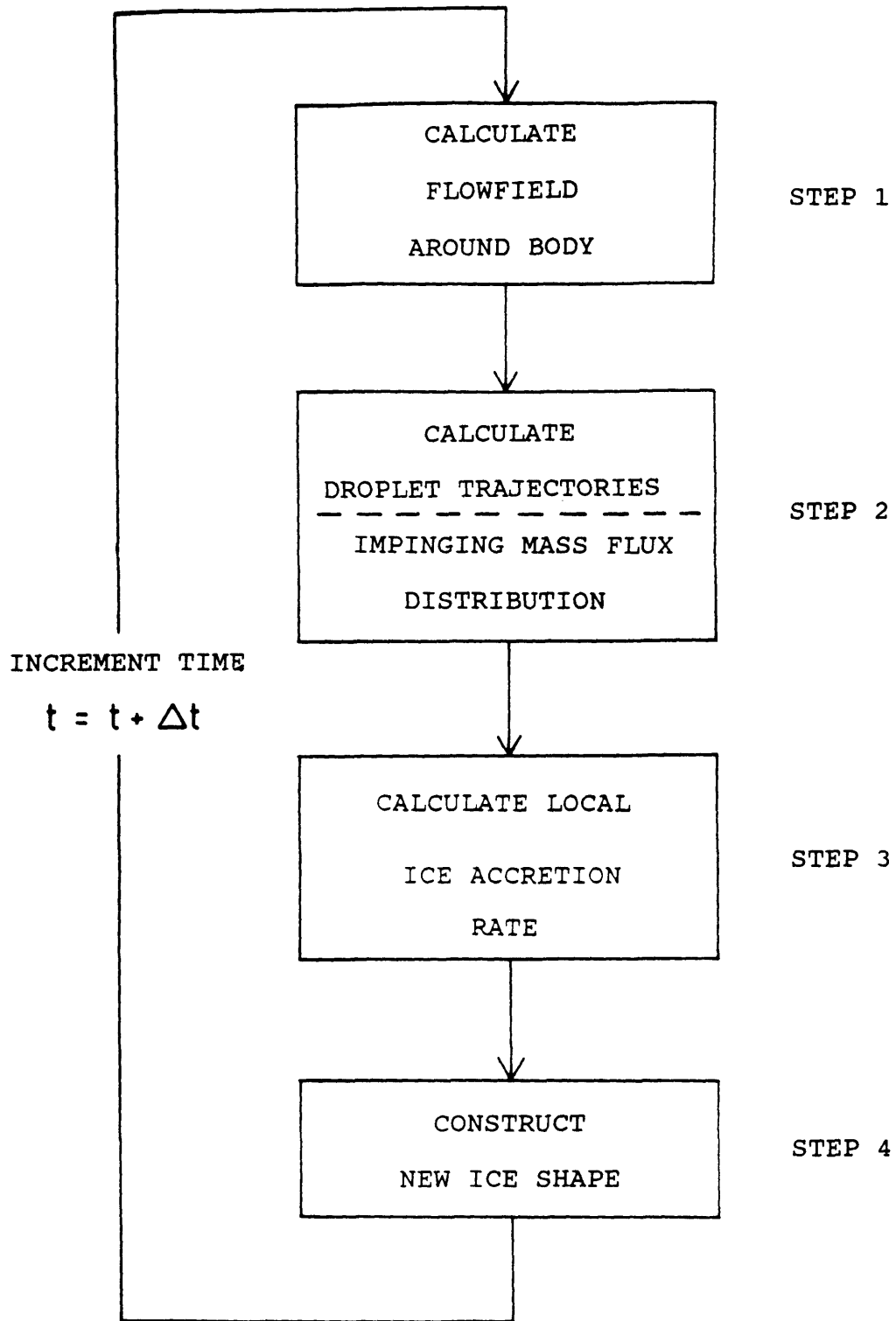
Figure 1-2   Schematic Breakdown of Analytical Ice Accretion
              Modeling Procedure

generated by the airfoils flow field. This impinging mass flux calculated by determining individual droplet trajectories to discover where or if they impinge on the body. This is described in terms of a local droplet collection efficiency. The collection efficiency is defined as the ratio of the mass flux of droplets arriving at a point on the surface to the mass flux of droplets which would pass through that position in an undisturbed flow. The collection efficiency is dependent on the droplet size distribution of cloud particles and liquid water content. The larger the mean volumetric diameter MVD and liquid water content the greater the collection efficiency.

Present computational methods of calculating the collection efficiency[4] require time consuming individual droplet trajectories to be evaluated based on assumed particle size distributions. The accuracy of such procedures, however, is good for well defined two-dimensional flowfields.

(3) Ice Accretion Rate

The local ice accretion rate is determined by the ability to remove the latent heat released by the freezing of water and the impinging mass flux of water. This requires the local heat and mass balance at the surface be evaluated. Two distinct types of ice can form, dependent on the ratio of the amount of impinging mass to the total heat transfer to remove its latent heat. If there is sufficient heat transfer to freeze all of the impinging water rime ice forms whereas if the heat transfer is insufficient to freeze the impinging

24

RIME ICE
"Cold" cloud temps. (-10°C to -30°C)
Small droplets (12μ typ.)

V_∞

Ice
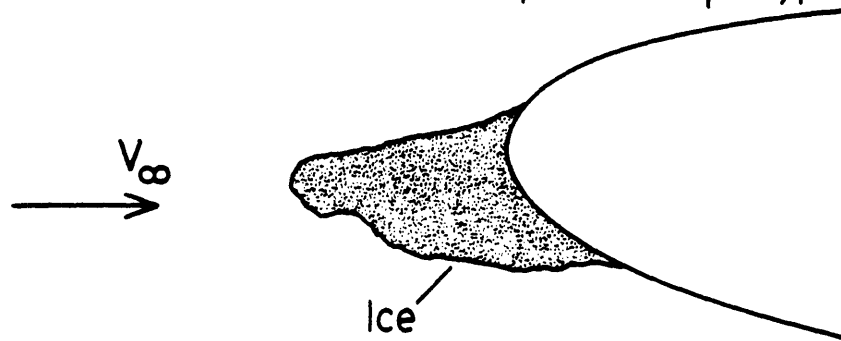
GLAZE ICE
"Warm" cloud temps. (0°C to -10°C)
Large droplets (20μ typ.)
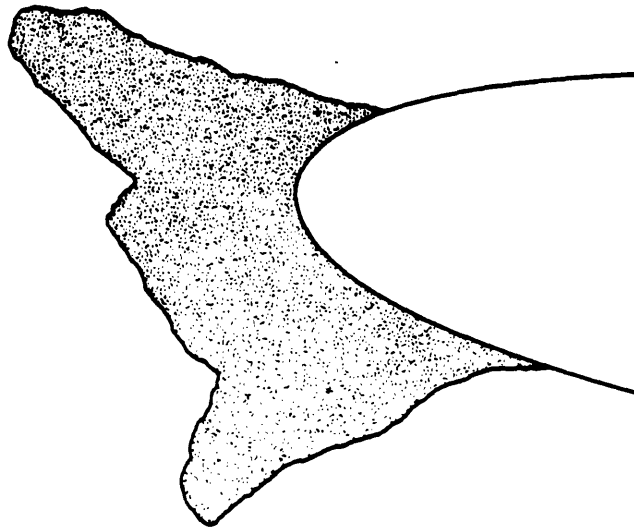
Figure 1-3   Typical "Rime" and "Glaze" Ice Formations on
NACA 0012 Airfoil [Taken from Kirby[5]]

mass glaze ice forms.

Figure 1-3 taken from Kirby[5] illustrates a comparison of typical rime and glaze ice accretions formed on a NACA 0012 airfoil.

Rime ice is formed at cold air temperatures and low liquid water contents when the heat transfer is high and the impinging mass of water is small. The resulting ice surface is dry and has a milky white appearance which is opaque. The opaqueness is caused by the rapid freezing of the water which traps dissolved air. Typically the ice so formed has a smooth profile and a low aerodynamic penalty.

For situations where the local heat transfer is insufficient to freeze all of the incoming mass of water glaze ice forms and the ice surface is described as wet. Glaze ice forms at warm temperatures close to freezing and high liquid water contents when the impinging mass of water is large. Glaze ice is typically clear in appearance. This is characteristic of slow freezing allowing air to dissociate out of solution. The ice shape is uneven and has a rough surface texture, commonly a "doublehorn" shape can be formed which has a large aerodynamic penalty.

1.3.1 Modeling of Rime Ice

For Rime ice, where the impinging supercooled droplets effectively freeze on impact there is considerable simplication possible. As all the incoming water freezes at its point of impact the problem of ice shape prediction

TEMP (°C)	LWC (g/m³)	MVD (μ)	VEL (m/s)
-26·1	1·02	12	52·1

Experiment (IRT)   Calculated (LEWICE)
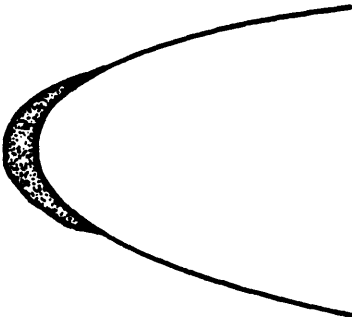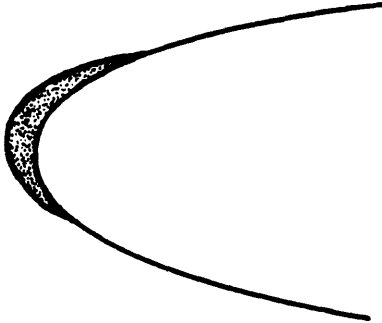
Accreted   Ice   Shape   After   2 Minutes   Exposure
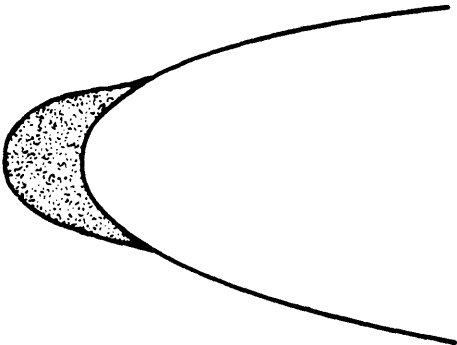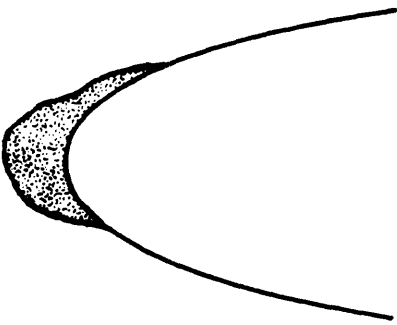
After   5 Minutes

Figure 1-4   Comparison of Experimentally Measured Airfoil
Ice Accretion and Analytically Predicted Ice
Growth, for Rime Ice Conditions (Taken from [5])

reduces to calculating the impinging mass flux at a given position. Figure 1-4 illustrates the good comparison between experiment and current ice accretion codes obtainable in rime ice conditions. The accuracy of ice shape prediction is determined by the accuracy with which the local collection efficiency can be evaluated.

1.3.2 Modeling of Glaze Ice

The presence of unfrozen water during glaze ice accretion, where there is insufficient heat removal to freeze all of the incoming water, requires that the local heat and mass balances be evaluated to determine the local ice accretion rate. Typical ice accretion models, such as the LEWICE code [3], ignore the specific details of unfrozen surface water behavior and use the assumption of uniform runback developed by Messinger[6] and others[7,8]. This assumes that the fraction of incoming water at a location which is not frozen on arrival runsback downstream and is considered as part of the incoming mass flux for subsequent downstream positions.

The local ice accretion rate is controlled by the ability to remove the latent heat released by the freezing water. Correct determination of glaze ice accretion will require calculation of the local convective heat transfer coefficient. It is this stage in which much of the uncertainty in present modeling occurs. Current methods of determining the heat transfer coefficent are discussed in

TEMP (°C)	LWC (g/m³)	MVD (μ)	VEL (m/s)
-14·4	0·96	37·5	93·9

Rime feathers

Experiment (IRT)

Roughness, k_S = 0·5mm

k_S = 1·0mm

k_S = 2·0mm

k_S = 4·0mm

Calculated (LEWICE)
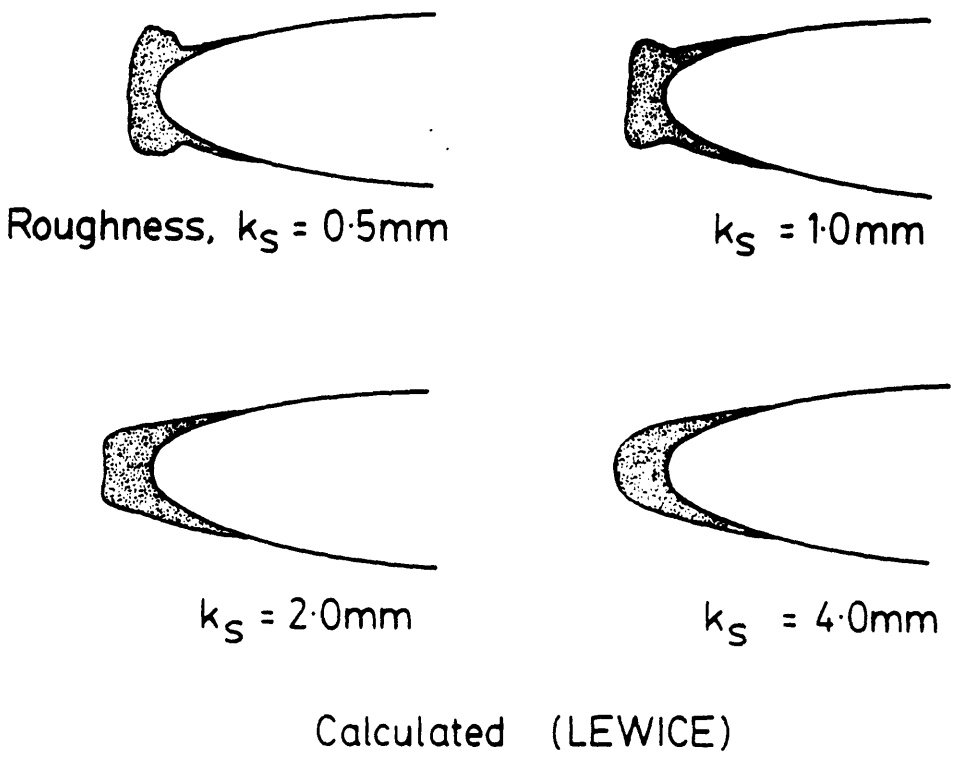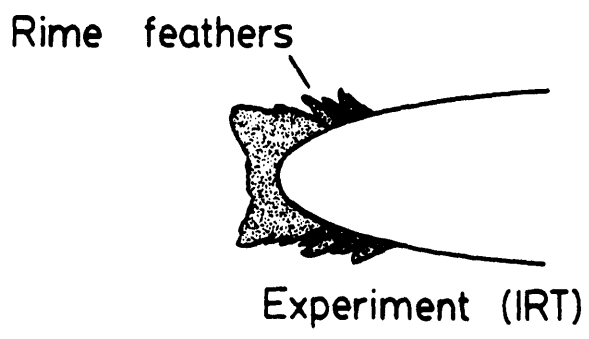
Figure 1-5   Effect of Assumed Surface Roughness on
Analytically Predicted Ice Growth, for Glaze
Ice Conditions.(taken from [5])

more detail in Section 2.4, but basically it is the roughness of the glaze ice surface which gives rise to the error. The roughness of a surface controls the transition of the boundary layer from laminar to turbulent flow and in turbulent flow enhances heat transfer. The physics of glaze ice surface roughness generation are not included in current codes. At present, the roughness of the ice surface, is treated in a simplistic or heuristic manner and is the prime source of error.

Figure 1-5 illustrates this for a typical ice accretion code [3] which currently uses a single input value for the surface roughness based on matching experimental and predicted ice shapes. The large variation in predicted glaze ice shape with the input roughness and the overall poor comparison suggest that consideration of the factors which govern surface water behavior should lead to better agreement between glaze ice accretion models and experimental results. Recent observations of actual glaze ice surface water behavior carried out by Olsen et al [9] in the NASA Lewis Icing Research Tunel indicated a variety of potential surface water modes of flow which differ from the Messinger uniform runback assmption.

Chapter Two

HEAT AND MASS TRANSFER ON A GLAZE ICE SURFACE

2.1 Introduction

The local ice accretion rate on a body exposed to icing
conditions is determined by the ability to remove the latent
heat released when water is frozen. For rime ice there is
sufficient heat transfer to freeze all the impinging water
and analysis of ice accretion simply requires the impinging
mass flux to be known. However, the formation of glaze ice
where not all the impinging water freezes on impact requires
that the local heat transfer and water flux along the surface
be evaluated. The primary mechanism of heat removal is by
convective heat transfer. The roughness of a glaze ice
surface can significantly enhance convective turbulent heat
transfer and hence control ice accretion rate.

The phase change of water to ice and the regions of
laminar, turbulent and seperated flow imply that the ice
accretion rate has to be calculated numerically by
determining the local heat and mass balances which will
control the amount of ice frozen at a given location.

The analysis of energy and mass transfer presented
below is based on previous work [1,10], however, the time
dependent terms and the conduction of heat through the ice

31

into the underlying surface are included. The subdivision of
the icing surface into a series of discrete control volumes,
as shown in figure 2-1 allows, an elemental analysis to be
carried out. The control volume formulation assures
conservation of mass and energy and allows corresponding heat
and mass balances for the individual control volumes to be
constructed. The use of such an approach is directly
applicable to computational methods for the numerical
simulation of ice accretion.
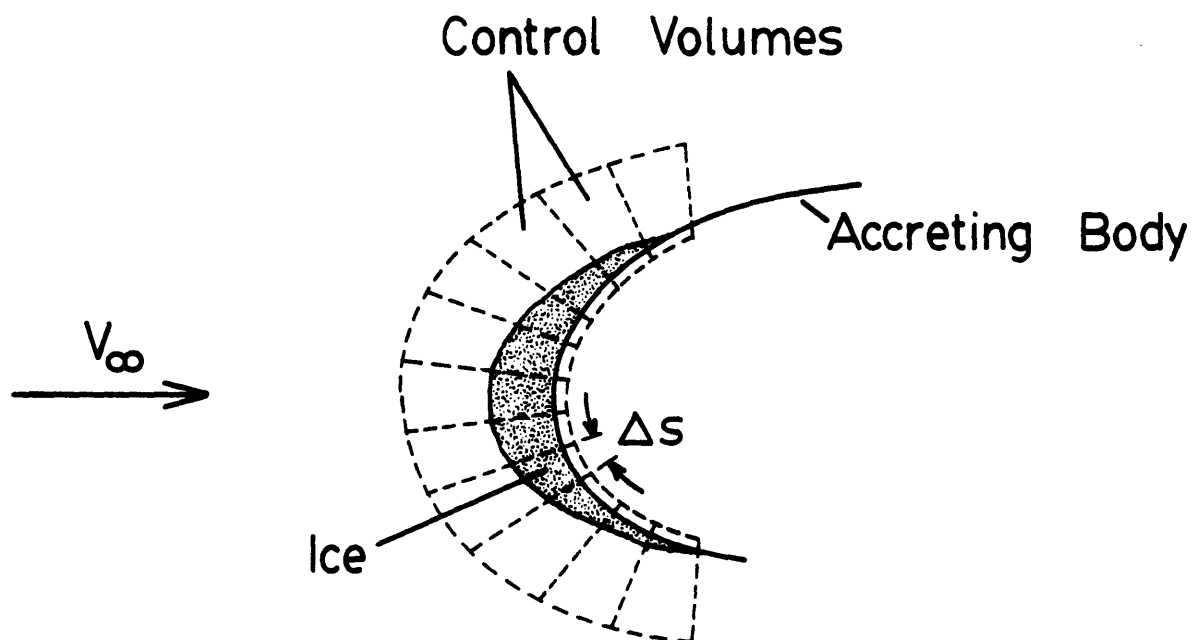
Figure 2-1   Control Volumes on Airfoil for Analytic
              Modeling

For the analysis a two dimensional steady external flow field is assumed to be altered only slowly by the accreting ice.

2.2 Mass Balance

The principle modes of liquid water mass transfer on an accreting ice surface are shown schematically in figure 2-2 which depicts mass flux into and out of a control volume. The primary source of water is the impingement of supercooled droplets. The impinging water mass flux is linearly related to the ambient liquid water content LWC, through the local droplet collection effficiency β and the freestream velocity U.

$$\dot{M}''_{imp} = \beta \ \ LWC \ \ U_\infty \tag{2-1}$$

The double prime superscript indicates the quantity is defined per unit area of the icing surface. Water also enters the control volume through mass flow along the surface depicted as $\dot{M}_{in}$ in figure 2-2.

Water leaves the control volume through surface flow $\dot{M}_{out}$ downstream and also by evaporation $\dot{M}_{evap}$. This evaporation is generally small as the ambient air has a high relative humidity in icing clouds.
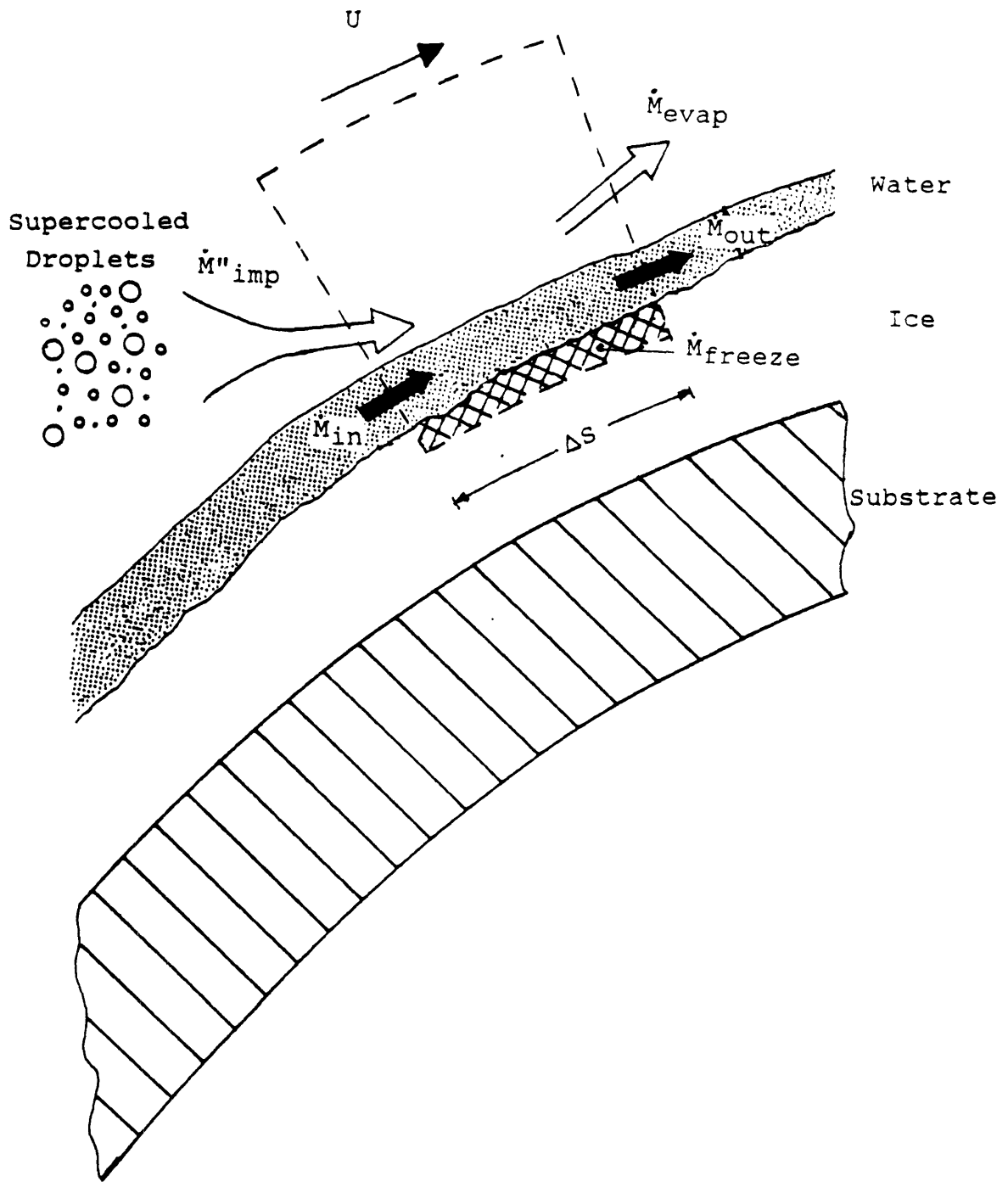
Figure 2-2   Mass Balance for a Glaze Ice Surface

$$\dot{M}^{"}_{evap} = (1/2) \; h \; D \; (\rho_{surf} - \rho_\infty) \qquad (2\text{-}2)$$

Where h is the heat transfer coefficient, D the diffusion coefficient, and ρ the vapor density.

Liquid water is removed by freezing at the water-ice interface. The freezing mass flux $\dot{M}_{freeze}$ is determined in glaze conditions by the ability to remove the latent heat of freezing released by the water-ice phase transition. This process couples the heat and mass balance and it will be discussed in Section 2.3. The total amount of unfrozen water in a given control volume may vary with time and this unsteady term is represented by $\dot{M}$ where M is the total mass of unfrozen water in the control volume at any given time.

Conservation of mass requires that the sum of all the flux terms be equal to the change in the amount of water present in the control volume. This is represented in 2-3 where A is the surface area and A' the projected area normal to the flux of impinging water droplets.

$$\dot{M} = A' \; \dot{M}^{"}_{imp} + \dot{M}_{in} - A \; \dot{M}^{"}_{freeze} - \dot{M}_{out} \qquad (2\text{-}3)$$

For rime icing conditions the convective heat transfer is sufficient to freeze all of the impinging mass flux. In this case there is no surface flow or unfrozen water and equation 2-3 reduces to:

$$A' \; \dot{M}^{"}_{imp} = A \; \dot{M}^{"}_{freeze} \qquad (2\text{-}4)$$

In glaze ice conditions, there is insufficient heat transfer to freeze all of the impinging mass flux and the surface water flow terms in 2-3 and the energy balance has to be considered to determine the local ice accretion rate $\dot{M}''_{freeze}$. Once this is known 2-3 can be solved to give the downstream surface flux $\dot{M}_{out}$ which flows into the next downstream control volume.

2.3 Energy Balance

The principle modes of heat transfer into and out of the control volume are depicted in figure 2-3. The primary source of heat is the release of latent heat of freezing Q_{freeze}. The incoming mass flux terms $\dot{M}_{imp}$ adds heat through its specific heat (assumed to be at the ambient cloud temperature) and its kinetic energy as shown in 2-5 and for a given external flowfield its value will be constant with time.

$$Q''_{imp} = \dot{M}''_{imp} (C_p T_\infty + (1/2) U_\infty^2) \qquad (2-5)$$

The surface flow terms $\dot{M}_{in}$ and $\dot{M}_{out}$ contribute similar terms, however as any unfrozen water on the surface will be at the freezing temperature ($0^\circ C$) and will have a small velocity, the net heat flux from the surface flow can be considered to be negligible.
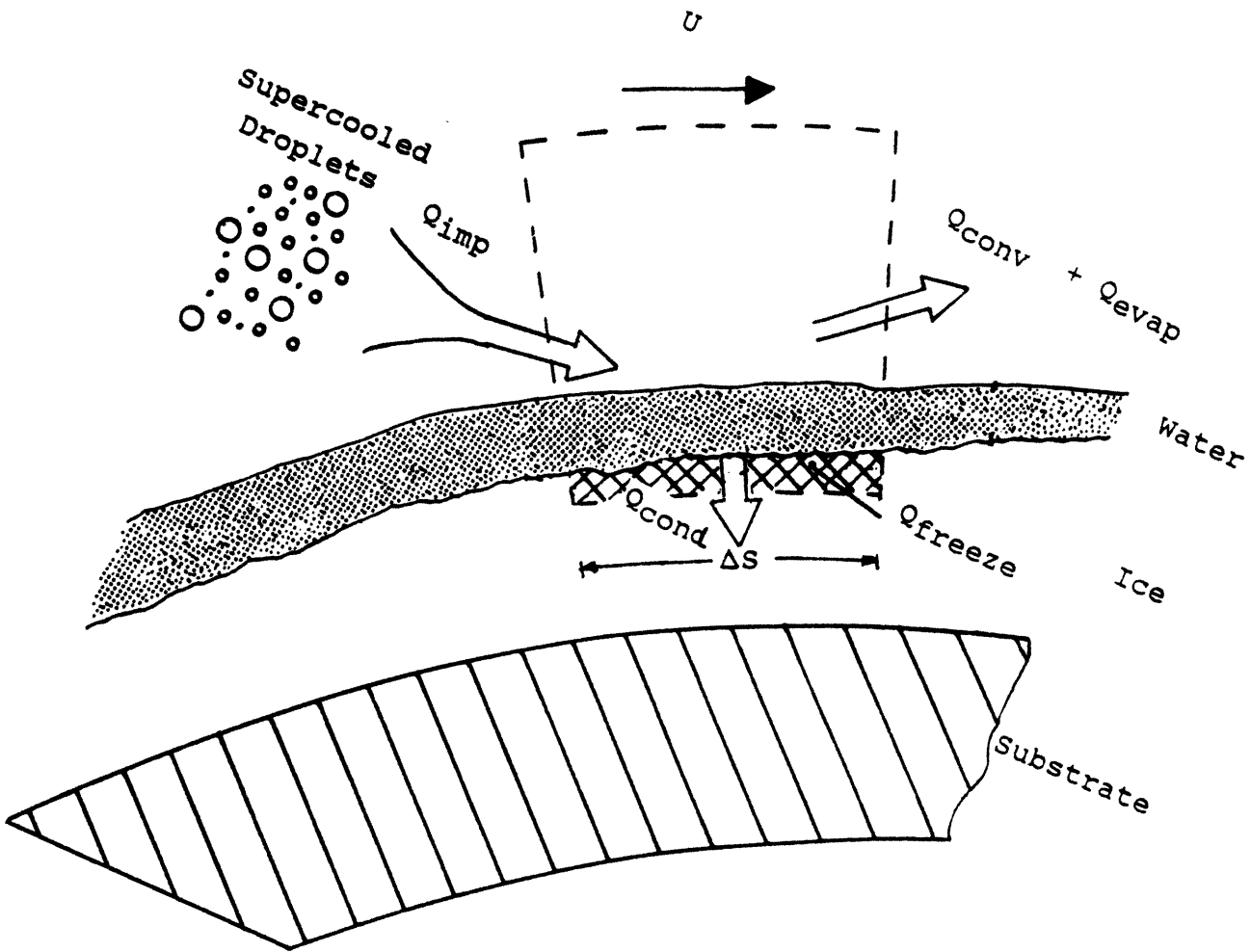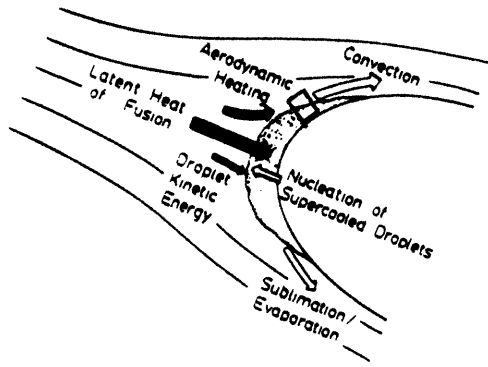
Figure 2-3

Heat Balance for Glaze Ice Surface

Labels in figure: Aerodynamic Heating, Convection, Latent Heat of Fusion, Droplet Kinetic Energy, Nucleation of Supercooled Droplets, Sublimation/Evaporation

U

Supercooled Droplets

Q_{imp}

$Q_{conv} + Q_{evap}$

Water

Q_{cond}

ΔS

Q_{freeze}

Ice

Substrate

Heat is removed from the control volume by convection into the external flow Q_{conv}, by conduction into the ice surface Q_{cond}, and evaporation Q_{evap} or for dry ice surfaces sublimation Q_{sub}. The convection can be described in terms of a heat transfer coefficient h determined by the local flow and the temperature difference between the local surface temperature T_{surf} and the adiabatic wall temperature T_{aw} which gives the convective heat flux Q_{conv} as.

$$Q''_{conv} = h \ (\ T_{surf} \ - \ T_{aw} \ ) \qquad (2-6)$$

The local surface temperature T_{surf} is held at the freezing temperature ($0^{\circ}C$) if the surface is completely wet, however, when there are dry areas of surface these will be cooled below freezing and the surface will have some average value below $0^{\circ}C$. The adiabatic wall temperature is defined [11] as that surface temperature for which identical flow conditions would give zero heat convection either away from or into the surface. It is expressed in terms of a recovery factor r based on the Prandtl number of air and the kinetic energy of the local freestream flow. In some literature the kinetic energy of the air is refered to as aerodynamic heating. It is caused by the viscous dissipation of energy which heats the air in the the boundary layer.

$$T_{aw} = \ T \ + 1/2 * (r \ / \ C_p \ ) * U^2 \qquad (2-7)$$

For evaporation or sublimation (phase change cooling) the driving force for the mass transfer away from the surface is the difference between the saturated vapor density of the ice or water surface and the local vapor density of the freestream. The mass transfer coefficient h_{mass} can be directly related using Reynolds analogy [11], to the heat transfer coefficient h.

$$h_{mass} = h \quad D/2 \tag{2-8}$$

Where D is the correct diffusion coefficient. This gives $\overset{\text{\tiny\textbullet}}{Q}_{evap}$ as equal to:

$$\overset{\text{\tiny\textbullet}}{Q}_{evap} = L_v \ h \quad D/2 \ (\ \rho_{surf} - \rho_\infty) \tag{2-9}$$

The conduction of heat Q_{cond} into the ice surface will occur if there are temperature gradients within the ice. This is represented in 2-10, where k is the thermal conductivity of the ice and dT/dn is the ice temperature gradient normal to the ice-water interface.

$$Q''_{cond} = - \ k_{ice} \ dT/dn \tag{2-10}$$

Initiallly the influence of heat conduction may be important if the temperature of the underlying surface is not at 0°C and the ice is thin so that there is a significant temperature gradient into the underlying surface. However, once the thickness of the ice increases and the underlying

surface warms this term will be negligible.

The conservation of energy requires the sum of all the heat flux terms to be zero, so for the control volume this gives, with the source terms on the right hand side:

$$Q_{evap} + Q_{conv} + Q_{cond} = Q_{freeze} + Q_{imp} \qquad (2-11)$$

The local ice accretion rate is determined by the local freezing mass flux M_{freeze} which is equal to:

$$\dot{M}_{freeze} = Q_{freeze} / L_f \qquad (2-12)$$

Where L_f is the latent heat of freezing of water. Rearranging 2-11 and neglecting the heat conduction this gives:

$$\dot{M}_{freeze} = (1/L_f)*[Q_{evap} + Q_{conv} - Q_{imp}] \qquad (2-13)$$

The importance of the heat transfer coefficient h to both Q_{evap} and Q_{conv} which are the main mechanisms of heat removal implies that calculation of $\dot{M}_{freeze}$ requires an accurate determination of the heat transfer coefficient h.

$$Q''_{evap} + Q''_{conv} =$$
$$h \{(T_{surf} - T_{aw}) + L_v D/2 (\wp_{surf} \neg \wp)\} \qquad (2-14)$$

2.4 Determination of Heat Transfer Coefficient

In glaze ice conditions the ice accretion rate is
determined by the local convective heat transfer. The heat
transfer coefficient h is defined as [11]:

$$h = \frac{k_{air} \, dT/dn}{(T_{surf} - T_{aw})} \qquad (2\text{-}15)$$

Where k_{air} is the thermal conductivity of air at T_{surf} and
dT/dn is the temperature gradient normal to the surface. The
heat flux per unit area normal to the surface divided by the
driving temperature potential. The heat flux through the
surface is equal to the thermal conductivity of the air
multiplied by the temperature gradient normal to the surface
evaluated at the surface.

For boundary layer flow the magnitude of the normal
surface temperature gradient dT/dn is proportional to the
ratio of the driving temperature potential $T_{surf} - T_{aw}$ to the
thermal boundary layer thickness δ_t This gives the heat
transfer coefficient as:

$$h \sim \frac{k_{air}}{\delta_t} \qquad (2\text{-}16)$$

In turbulent flow the thermal boundary layer and velocity

41

boundary, by Reynolds analogy [11], have approximately the same thickness and profile.

In general, the larger the freestream velocity the thinner the thermal boundary layer will be at a given position and therefore the greater the convective heat transfer. The constant of proportionality for 2-16 is dependent on the velocity profile of the boundary layer, whether the flow is laminar or turbulent, and for turbulent flows the roughness of the surface.

The engineering use of h is that it removes the necessity for explicitly calculating the local temperature gradient. For given flow conditions, empirical or analytic expressions have be found for h. The inherent danger of such an approach when applied to icing is that some of the assumptions implicit in developing these expressions for h may no longer hold.

The surface of glaze ice is rough [12] and will affect the local heat transfer[13]. The effect of surface roughness will depend on whether the boundary layer is laminar or turbulent. In laminar flow, roughness will not effect heat convection, however, it will adversly affect the stability of the laminar boundary layer and cause earlier transition [14,15] of the boundary layer to turbulent flow.

In turbulent flow the effect of surface roughness is determined by the ratio of the roughness element height k to the boundary layer thickness[16]. For k less than the thickness of the viscous sublayer of the turbulent boundary layer the roughness will have no effect and the wall can then

be considered as hydraulically smooth. Above this value of roughness height the roughness element will promote turbulent mixing in the boundary layer and can be considered as increasing the effective viscosity of the air. As the mechanisms of heat transfer and momentum transfer are similar in a turbulent boundary layer the effect of a roughness element k on the velocity boundary layer can be considered as identical to its effect on the thermal boundary layer[11] and hence heat transfer enhancement. The greater the height of roughness elements the greater the heat transfer enhancement.

The original work examining the effect of roughness on fluid flow was carried out by Nikuradse[17] who examined the effect of rough walls on flow in pipes. The effect of the individual roughness element geometry was investigated by Schlichting[18] who introduced the concept of an 'equivalent sand grain roughness' k_S which relates the effect of different roughness element geometries and densities on wall skin friction and boundary layer transition. Recent work[19] questions the usefulness of such a single parameter for describing the effect of roughness.

A non-uniform roughness formed by a stochastic process such as icing is difficult to define in a quantative manner[20]. Measures that are commonly used to describe such surfaces are the mean roughness element height K, the maximum roughness height k_{max}, and also the number of individual roughness elements per unit area. Experimental work by Bandyopadhay[21] showed that the spanwise extent of roughness elements is important to heat transfer. The smaller the

43

spanwise extent the "rougher" the surface and the greater the heat transfer.

The difficulties of modeling roughness are closely coupled to the lack of quantative understanding of the mechanisms which cause turbulence. At present the use of a single roughness height, such as the equivalent sand grain roughness, in modeling rough heat transfer enhancement is the most useful parameter available.

Current ice accretion codes such as the LEWICE code [3], use an integral boundary layer method to calculate the heat transfer coefficient on the ice surface. In this method, a Reynolds number criteria based on a single input value of roughness k_s is used to locate the transition of the boundary layer from laminar to turbulent flow. The same value of roughness is also used in the turbulent region to determine the amount of heat transfer enhancement. The value of k_s used is chosen by matching the predicted ice shape to that obtained experimentally. Other methods [22,23] to determine the heat transfer coefficient have used empirical expressions based on the measurements of heat transfer on rough surface cylinders[24] or by directly matching the heat transfer to experimentally accreted ice.

The non-physical determination of the ice surface roughness explains the poor comparison of current glaze ice accretion codes and the need for determining the micrphysical behavior of surface water and including it in ice accretion models.

Chapter Three

MICROPHYSICS OF SURFACE WATER BEHAVIOR

3.1 Introduction

The ice accretion rate $\dot{M}_{freeze}$ is controlled by the heat transfer and impinging mass. This in turn determines the mass flux $\dot{M}_{in}$ and $\dot{M}_{out}$ of water on the ice. The unfrozen water is important to the generation of a rough ice surface and hence the convective heat transfer. The surface transport of unfrozen water is controlled by the physical interaction between water and the underlying surface and the external forces be they aerodynamic or gravitational which act on the water

Recent NASA [9] high magnification observations of icing surfaces showed that there are other modes of surface transport apart from the steady state runback assumption made in current models. The particular surface transport mode will depend on the forces which act on the water. For an airfoil these forces will be due to the external boundary layer flow, gravity, and the surface resistance of the surface to motion of water. The magnitude of these forces vary with position from the leading edge.

Water on a surface can behave in a variety of ways depending on the balance of forces acting, the flow rate of water and the wettability of the surface. The four possible modes of surface transport are shown in the schematic figure 3-1. For high water flow rates and wettable (low surface resistance) surfaces the water will tend to coat the entire surface with a uniform water film. For lower flow rates or higher surface resistance there is insufficient water to maintain a thin film over the entire surface. Once a dry area appears, surface tension forces will tend to coalesce the available water into rivulets or water beads. If the surface tension and the corresponding surface resistive force become sufficiently large, water flow will cease. The water beads will remain stationary until such a time that they have either grown by coalesence, impingement or collision to such a size that the external forces overcome the droplets resistance to motion.

Thin film flow of fluids are a class of boundary layer problems which can be analysed using techniques identical to those applied to boundary layer theory. It is therefore possible to relate the thickness of water film and the total mass flow rate to the forces acting on the surface of the film and on its bulk. In quantitative terms the breakdown of a two-dimensional film flow into rivulets or beads will occur when the film thickness and mass flow rate become sufficiently small that the surface tension of the water-air

46

Thin Film

Rivulet

Bead

Stationary
Droplet
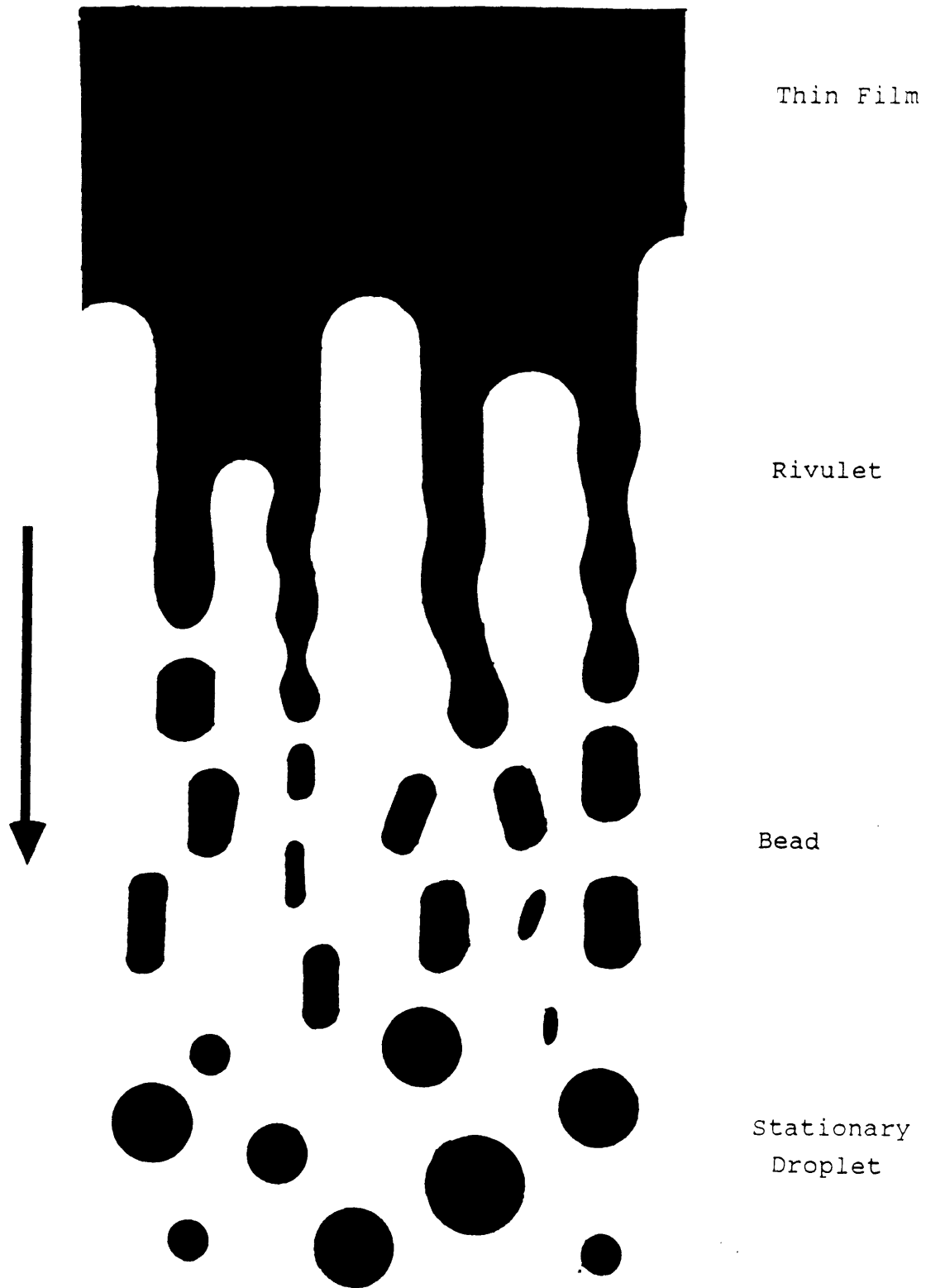
Figure 3-1   Modes of Surface Water Transport
Schematic

interface acts to reduce the total surface energy of the
water and surface and it is energetically favorable to have
dry areas of surface and a three dimensional rivulet or bead
flow. This process of film breakdown has been investigated
in relation to the appearance of hot spots in the condensate
film on condensor tubes [25]

Figure 3-2 defines a control volume for the film flow of
water along an ice surface. As described in Section 2.2 water
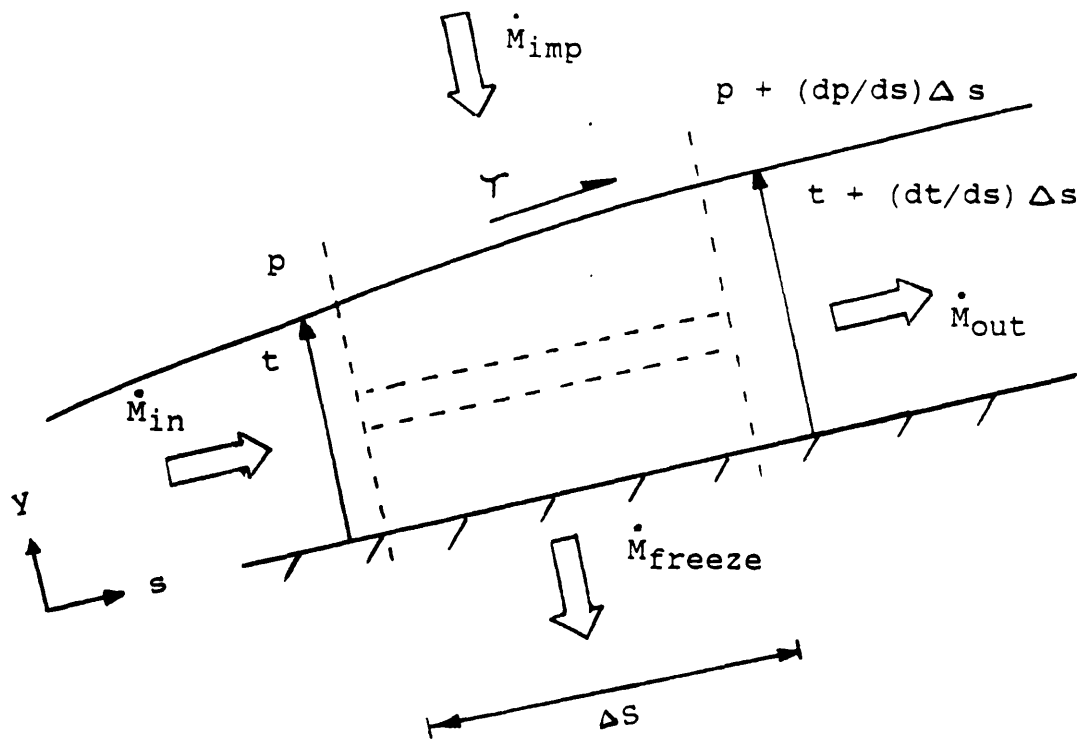
Figure 3-2   Control Volume for Film Flow of Water

48

will be removed from the film by freezing M_{freeze} and added
by the impinging supercooled droplets M''_{imp}. A surface shear
stress acting across the water-air interface, the external
streamwise pressure gradient and gravity component tangential
to the surface all act on the film of water. The analysis
detailed in Appendix I derives an expression for the change
in film thickness with downstream position s.

Near an airfoil leading edge, the pressure gradient and
surface shear stress act to move water in the downstream
direction and will cause the film to thin. The surface shear
stress driving the water film removes momentum from the
boundary layer of air. This momentum loss affects the
transition of the boundary layer. The larger the mass flux
the greater the momentum loss and the earlier boundary layer
transition will occur. Turbulent flow has a much higher
surface shear stress and dependent on the mass flow rate may
cause the film to thin rapidly and breakdown into rivulet or
bead flow.

Once breakdown of a film into rivulets seperated by dry
surface, occurs the surface resistance to motion of the edge
of the rivulet will determine the spanwise boundaries of the
rivulet and has to be considered. The magnitude of the
surface resistance of the water-surface boundary along with
the mass flow rate will determine the width and height of the
rivulet. Rivulet flow becomes unstable if the mass flow rate
is reduced or the surface resistance of the interface
increases and causes the rivulet to neck. The breakdown of a
rivulet into individual beads of water will occur either

through variations of the resistance of the three phase interface or irregularities of the surface over which the rivulet is flowing.

A bead of water will be subject to the same forces as those acting on rivulets. In addition, there will also be an additional surface resistance to motion of the leading and trailing edges of the drop. Motion will cease if this surface resistance overcomes the external driving forces acting on the bead. For surfaces which are not smooth the effect of roughness will be to increase the resistance to motion significantly.

A stationary bead may recommence downstream motion if its volume become large enough for the external forces to overcome the surface resistance of its leading and trailing edges. The volume of such a stationary water bead can be increased by collision and coalescence with other beads also in icing by the impingment of cloud droplets. If two stationary beads touch the action of surface tension to minimise surface area will cause them to coalesce into one larger droplet which may be large enough to overcome the surface resistance and move downstream. Moving beads may collide with the stationary drop and cause it to be dislodged and move downstream.

3.3 Forces Acting On Surface Water

The microphysical behavior and mode of surface transport of water on a glaze ice surface will be controlled primarily by the relative strength of the surface resistance, aerodynamic and bulk forces. Surface tension forces tend to minimize the surface area of the fluid, causing the water to coalesce into beads or rivulets. Surface resistance forces oppose motion of the fluid along the surface through the resistance of the fluid-surface-air interface to movement (contact line resistance). Bulk forces such as gravity or centripetal acceleration are solely dependent on position and act uniformly on all the water at that point. Aerodynamic forces are the result of pressure gradients and the shear stress acting at the water-air interface and are determined by the local flow field. A general expression for the forces acting on the total amount of water present at a given position is shown in 3-1 and this indicates the resulting mode of surface water transport dependent on the relative magnitude of the forces acting.

$$F_{resis} < F_{aero} + F_{bulk} : \text{Film} \qquad \text{(3-1 a)}$$

$$F_{resis} \sim F_{aero} + F_{bulk} : \text{Rivulet/Bead} \qquad \text{(3-1 b)}$$

$$F_{resis} > F_{aero} + F_{bulk} : \text{Stationary} \qquad \text{(3-1 c)}$$

When the external and surface resistance are of the same magnitude 3-1 b. The mass flow rate of water will determine whether the flow is as rivulets or beads. A high mass flow will give rise to rivulets. If there is a sudden discontinuity in surface resistance the flow may transition directly from film flow to stationary beads.

Each of the three types of force are discussed in relation to conditions on a glaze ice surface in the following sections:

3.3.1 Surface Resistance Force

The three phase interface between air-water-surface has a resistance to motion. This can be described in terms of the boundary between two phases such as water and ice possessing a surface energy. Work is required to change the interface's surface area. At a three phase interface, such as that between water, a solid surface and air there will be an overall force balance between the three interfacial surface energies. This was first described by Young [26] for an ideal surface as:

$$\sigma_{lg} \cos \theta = \sigma_{sg} - \sigma_{sl} \qquad (3\text{-}2)$$

Where the subscripts s,l,g refer to the solid, liquid and gas phase respectively, σ being the interfacial surface energy (surface tension for fluids) between two phases. The internal angle the air-water surface makes with the solid surface at

the three phase interface is termed the contact angle θ.
Figure 3-3 illustrates this for a sessile drop on a
horizontal surface.
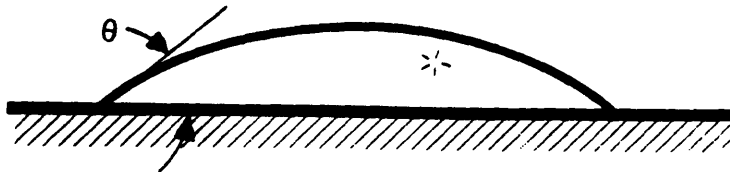
Figure 3-3   Contact Angle Definition for Sessile Drop on
             Horizontal Surface

The contact angle θ is a measure of the attraction
between water and that surface. A surface which has a low
contact angle ($<10°$) is described as wettable and has a low
resistance to fluid motion. Whereas, a high contact angle
causes droplets to bead up a characteristic of wax surfaces.

When a three phase interface is subjected to an external
force the contact angle can deviate from its equilibrium
value. This process is illustrated in figure 3-4 for a
sessile drop on an inclined plane. The maximum difference
between the advancing contact angle θ_a and receding contact
angle θ_r occurs just prior to motion and is termed the
contact angle hysteresis[27]:

53
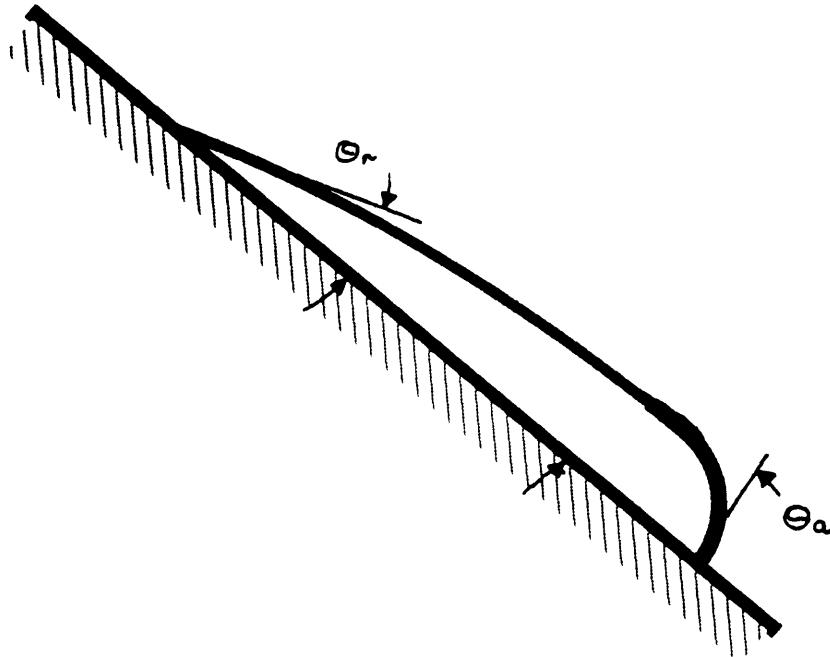
Figure 3-4   Contact Angle Hysteresis Definition for a

Sessile Drop on Inclined Plane

$$\Delta\theta = \theta_a - \theta_r \qquad (3-3)$$

Recent work by Dussan & Chow [28,29,30] has theoretically investigated the maximum shear stress or angle of inclination of the surface necessary to initiate motion of droplets for low contact angles.

The movement of a contact line (three phase interface) requires work to change the area of the three surfaces which

meet at the contact line. This requirement for energy input
gives rise to a contact line resistance force. This
resistance force can be expressed in terms of the contact
angle, contact angle hysteresis, surface tension and a
characteristic droplet dimension [28]. For a moving contact
line it will also be proportional to the velocity with which
the contact line moves. The validity of using static values
of contact angle and hysteresis is questionable for all but
low velocities [27].

The resistive force per unit length F_{line} of a contact
line can be expressed in terms of the difference from the
Young's equilibrium horizontal component of surface tension
and this is illustrated in figure 3-5:

$$F_{line} = \sigma \cos \theta_a - \sigma \cos \theta \qquad (3\text{-}4 \text{ a})$$

$$F_{line} = \sigma \cos \theta - \sigma \cos \theta_r \qquad (3\text{-}4 \text{ b})$$
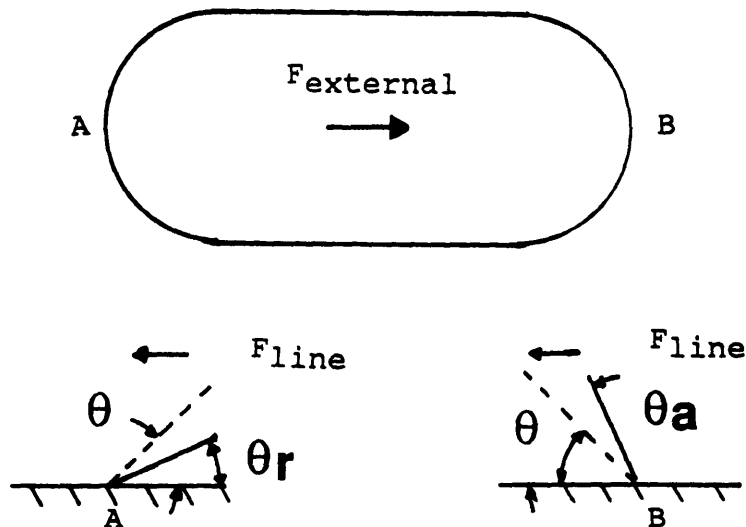
Figure 3-5   Surface Resistance of Droplet Definition sketch

For the case of a droplet which has two interfaces the total resistance will be the sum of the leading and trailing edge contact line resistances. Prior to motion a droplet has a planform similar to that defined in Figure 3-5 [30]. To first order the resistance to motion of a droplet will be:

$$F_{resis} = \sigma \ (\cos \theta_a - \cos \theta_r) \ w \qquad (3-5)$$

Where the length of both the leading and trailing edge interfaces is taken to be approximately equal to width w of the droplet, the advancing and receding contact angles are the same, and the parallel sides have no resistance to motion [30]. By considering the advancing and receding contact angles to be equal to the static equilibrium contact angle and half the contact angle hysteresis:

$$\theta_a = \theta + \Delta\theta / 2 \qquad (3\text{-}6 \ a)$$

$$\theta_r = \theta - \Delta\theta / 2 \qquad (3\text{-}6 \ b)$$

Trigonometric manipulation gives the surface resistance to motion of a droplet as:

$$F_{resis} = 2 \ w \ \sigma \ \sin \ \theta \ \sin \Delta\theta / 2 \qquad (3\text{-}7)$$

The product of sine terms will be defined as the resistance factor R_f and is a property of the surface material.

$$R_f = \sin \theta \sin \Delta\theta / 2 \qquad\qquad (3-8)$$

The surface resistance of a droplet is, therefore, proportional to the diameter of the drop, the resistance factor R_f, and the surface tension.

The dependence of the interfacial surface energies on the relative molecular strengths imply that the surface energy and hence contact line resistance will be dependent on temperature. Section 4.2 describes an experiment to determine the contact angle, contact angle hysteresis and resistance factor of water droplets on ice as a function of ice surface temperature.

3.2.2 Flow induced forces

The boundary layer flow of air over an airfoil gives rise to pressure gradients and shear stresses acting on the surface water. For high Reynolds number flow the boundary layer is thin and the external flowfield pressure gradient remains constant across the boundary layer and is the pressure gradient which acts on the surface water.

At the water surface the normal and tangential velocity of the air and water are the same (no-slip condition). If there is a tangential velocity gradient normal to the surface this will induce a shear stress acting on the interface. This shear stress is dependent on the local flowfield within the air boundary layer. The surface shear stress is continuous

across the interface[31] and will cause motion within the
water layer or bead. For individual water beads, the
pressure gradient and shear stress can be regarded as the
conventional pressure drag and skin friction. The total
aerodynamic force F_{aero} is therefore proportional to the
droplet surface area d^2 where d is the diameter of the
droplet.

On aerodynamic bodies such as airfoils the region near
the leading edge is characterised by a favorable pressure
gradient. That is, the external flow field is accelerating
and the static pressure dropping. This gives rise to a
pressure gradient acting in the downstream direction and
which is zero at that point where the external flowfield's
velocity is a minimum. The shear stress at the surface has a
minimum at the stagnation point and then again is equal to
zero when the boundary layer flow seperates. Flow
seperation, if it occurs, for bodies at modest angles of
attack, is confined to the rearward section of the airfoil.
The shear stress will, therefore, act in a downstream
direction for the region of interest for ice accretion.

3.3.3 Bulk Forces

Bulk forces in the icing problem result from the local
gravitational field or in rotating components centripetal
acceleration. The component of gravitational acceleration
acting tangential to the ice surface determines the direction
and magnitude of the driving gravity force. Its maximum

58

value will be when the surface is vertical eg. for airfoils, close to the leading edge. The centripetal acceleration always acts radially outward from the centre of rotation and is proportional to the rate of rotation and the square of the radius. The magnitude of both these bulk forces F_{bulk} is proportional to the volume of water present which for individual droplets is dependent on d^3.

The component of gravity normal to the surface will act on upper surfaces to keep the water in contact with the surface or on lower surfaces to remove it. For individual water beads the resulting shape of a bead is described[32] as either sessile or pendant respectively.

3.4 Force Balance on Water Bead

For a stationary water bead the relative strengths of the external and surface resistance forces are dependent on a characteristic dimension of the bead, such as its diameter d. The flow induced forces are proportional to the bead's surface area whereas the surface resistance is proportional to the width of the bead. Therefore, as the volume of water in the bead is increased the flow induced force F_{aero} will increase more rapidly than the surface resistance F_{resis} and at some stage will overcome the resistance and the bead will breakaway and move downstream. This critical droplet size will depend on the resistance factor R_f of the surface and the external flowfield. Section 4.3 describes an experiment to investigate this condition for droplets in a flat plate

boundary layer for a range of surface resistance factors.

Chapter Four

SURFACE RESISTANCE EXPERIMENTS

4.1 <u>Introduction</u>

Distinct roughness elements formed by the freezing of
stationary water droplets are illustrated in Figure 4-1 which
is taken from recent photographic studies of glaze ice
accreting surfaces by Olsen et al[9] in the Icing Research
Tunnel at NASA Lewis. Stationary water droplets require that
their surface resistance F_{resis} be greater than the external
driving forces. To examine the importance of surface
resistance on a glaze ice surface two simple experiments were
conducted.

The surface resistance force is dependent on the affinity
of the water for the underlying surface. It can be
characterised in terms of the resistance factor R_f defined in
3-8 which depends on the contact angle and contact angle
hysteresis. To determine the magnitude of these quantities
for water on ice experimental measurements were made for
water droplets on ice over a range of ice surface
temperatures from $-4^{\circ}C$ to $-15^{\circ}C$. The water droplets were
subject only to a gravitational force.

To examine the resistance of a water droplet to motion
small wind tunnel of the critical breakaway velocity

BIG WATER DROP ON TOP OF ICE HILL

ROUGH SURFACE SUGGESTS EXPOSED ICE

STAGNATION LINE

1000 μM
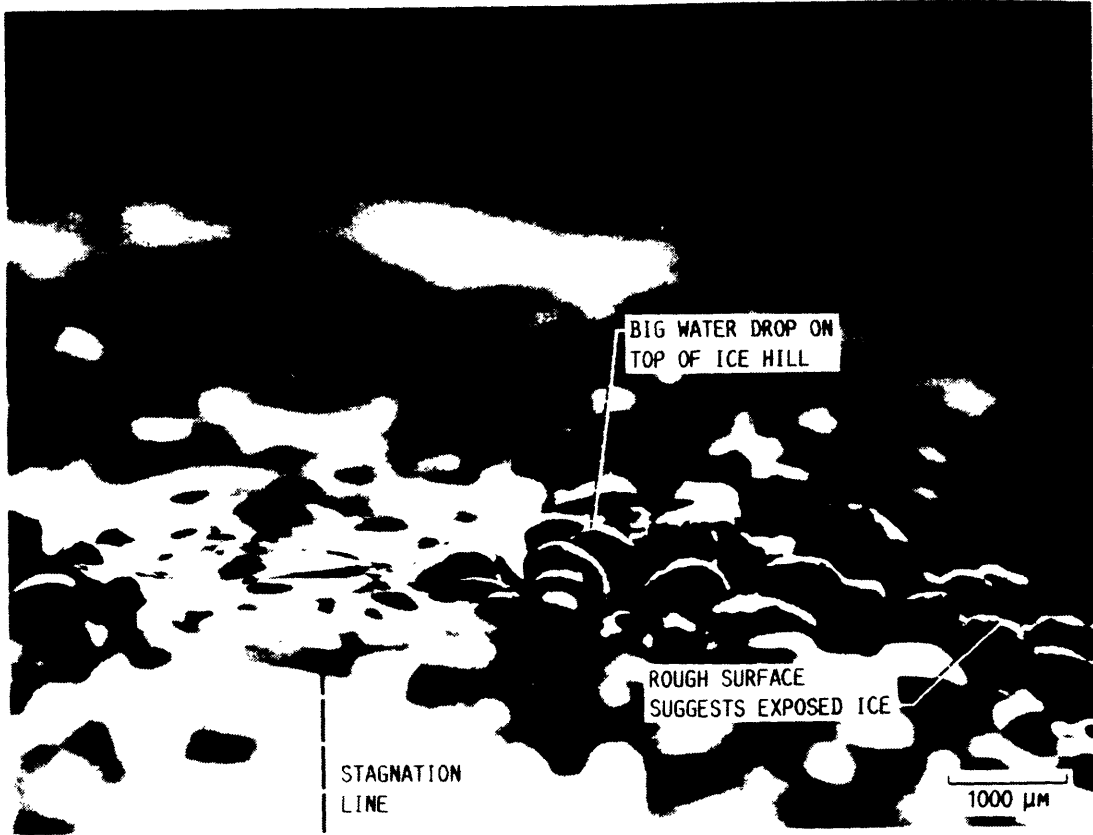
(B) 50 SEC.

Figure 4-1   Photograph of Glaze Ice Surface (taken from[9])

necessary to initiate downstream motion of a water drop. A
simple flat plate boundary layer flow was used so that the
only external force was that due to the surface shear stress.
The droplet will breakaway when this surface shear stress is
equal to the surface resistance. A range of surfaces was
therefore used to determine the effect of varying the
resistance factor.

4.2 <u>Measurement of contact angle between water and ice</u>

The contact angle and contact angle hysteresis are
important parameters in determining the behavior of water on
an ice surface. There is, however, little data available on
θ and $\Delta\theta$ for water on ice. This is partly due to experimental
difficulties working with supercooled water. Most
investigations of the surface properties of supercooled water
have concentrated on measurements of surface tension [33]. In
order to obtain working values of θ and $\Delta\theta$ a series of simple
experiments were conducted.

4.2.1 Experimental Setup

The apparatus employed in these investigations is shown
schematically in figure 4-2. A smooth layer of ice,
approximately 8mm thick, was formed· from distilled water on a
metal plate which could be set at a variety of angles with
respect to the horizontal. Pre-cooled droplets of distilled
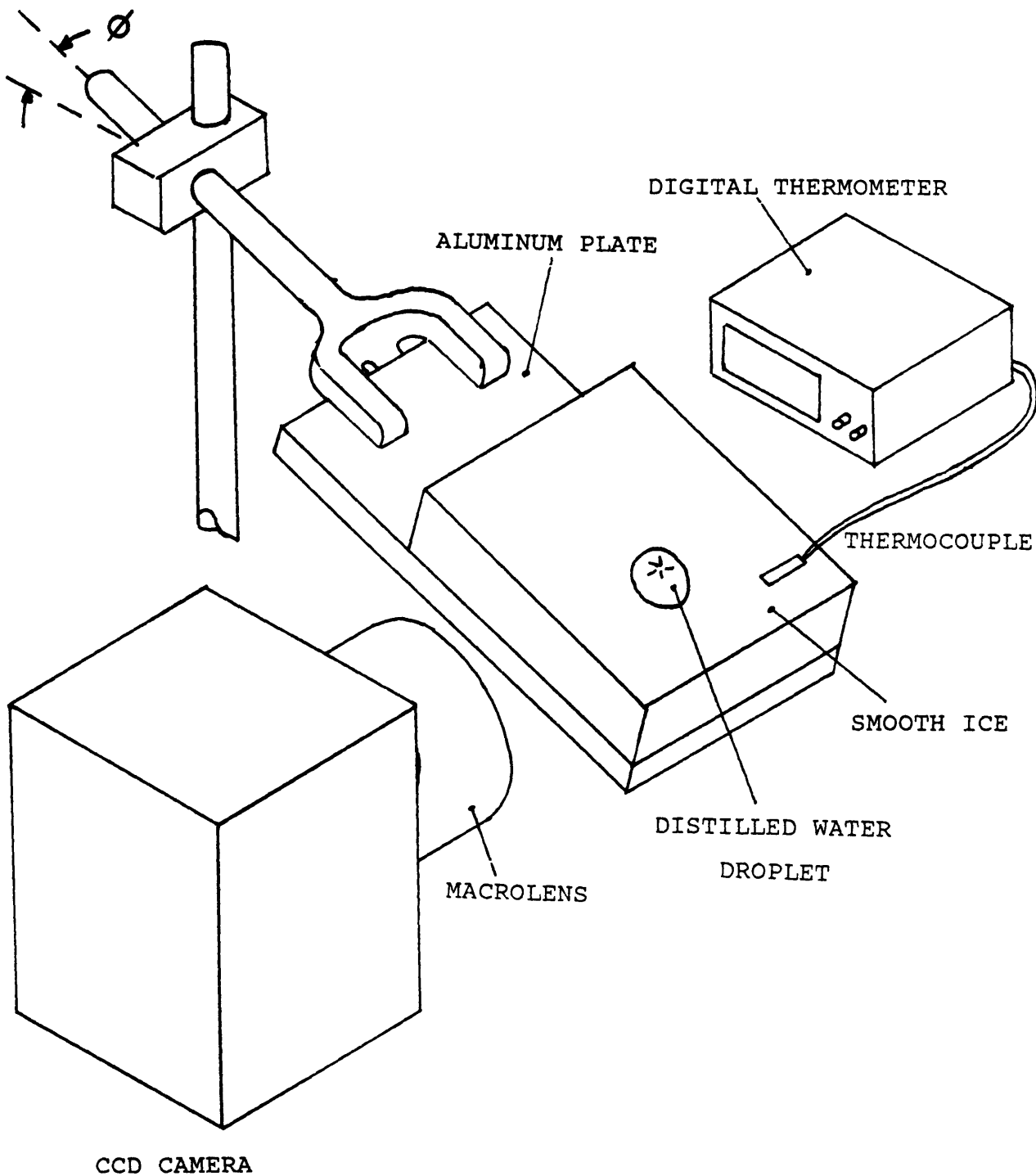
Figure 4-2   Schematic of Contact Angle Measurement Setup

water were placed on the ice surface by a syringe and their shapes were recorded by a CCD Microvideo camera oriented to view the ice surface to give a sideview of the droplet.

By use of a dark background and a diffuse light source, a sharp high-contrast image of the droplet at the ice-water interface could be obtained. This enabled contact angles to be measured to an accuracy of approximately 5°. The ice surface temperature was monitored by an Iron-Constantan thermocouple mounted in direct contact with the ice surface. The output of the thermocouple was presented on a digital display within the field of view of the video camera. This produced a simultaneous record of contact angle and surface temperature valid to within 1^OC.

Measurements of the contact angle at various ice temperatures were obtained by initially cooling the iced metal plate, in a cold box, to a temperature below the target measurement temperature. The plate was then removed from the cold box and mounted horizontally within the field of view of the camera. As the plate warmed to the target temperature, droplets were placed on the surface and their shapes recorded. Although the droplets would begin to freeze shortly after placement, the initial contact angle was preserved in the frozen drop and any transient effects could be observed in the video record. In this manner, values of the contact angle of water on ice could be obtained for a range of subfreezing temperatures.

The contact angle hysteresis measurements were made utilizing a similar procedure. However, the iced plate was

set to an angle of 30° with respect to the horizontal. Each droplets volume was increased by syringe injection until motion began, at this instant the advancing and receding contact angles and the surface temperature could be obtained from the video recording.

4.2.2 Results

The observed dependence of contact angle and contact angle hysteresis with temperature is shown in figure 4-3 and figure 4-4. Due to the low contact angle at temperatures above -4°C it was not possible to obtain accurate measurements above this temperature. However, at the freezing point, ice and water are in equilibrium so that the ice surface must be perfectly wettable, implying that both θ^c and $\Delta\theta$ are zero. These points have, therefore been included in the contact angle and hysteresis plots. They are consistent with the experimentally observed values and allow interpolation between -4°C and 0°C.

Both the contact angle and hysteresis exhibit a strong variation with temperature particularly in the vicinity of the freezing point. These results imply that the wettability of the ice surface will decrease greatly as the ice surface cools below freezing. For warm surfaces near 0°C, water will tend to spread into thin films and the ice-water contact line will have a low resistance to motion. For colder temperatures water will tend to bead into droplets which will require a higher external force to initiate fluid motion. In addition,

66
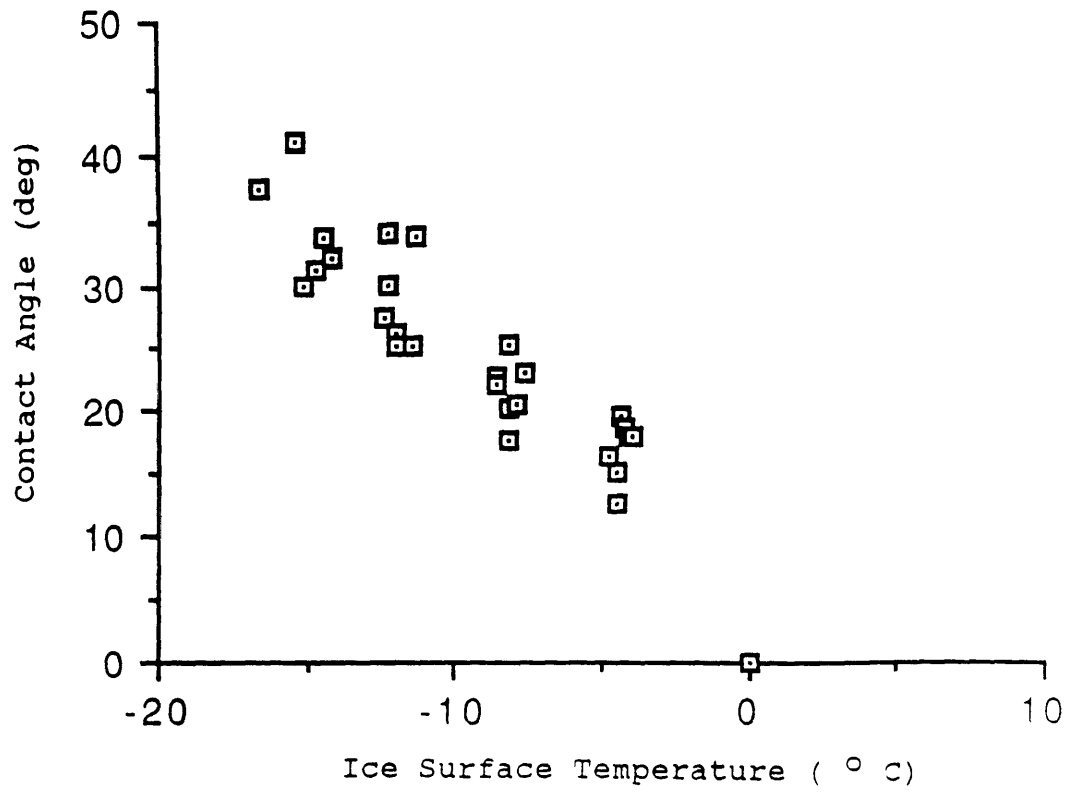
Figure 4-3   Temperature Variation of Contact Angle for Water on Ice
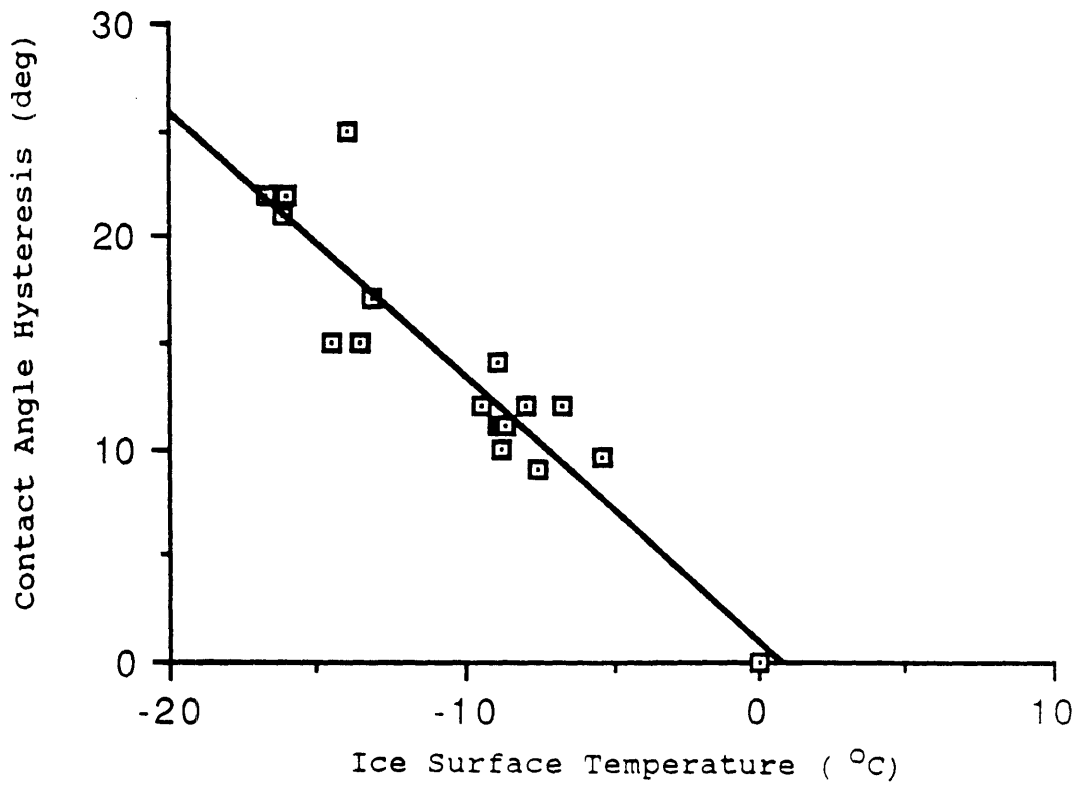
Figure 4-4   Temperature Variation of Contact Angle Hysteresis for Water on Ice

a droplet freezing on a cold surface will have a greater roughness height than an equivalent volume droplet freezing on a warmer ice surface due to the increased contact angle at colder temperatures.

Figure 4-5 plots the resistance factor R_f, defined in Section 3.3.1, against the ice surface temperature for interpolated values of contact angle and contact angle hysteresis. The strong temperature dependence of contact line resistance force indicates the potential importance of thermal gradients on an ice surface to the development of surface roughness. Small variations in the ice surface
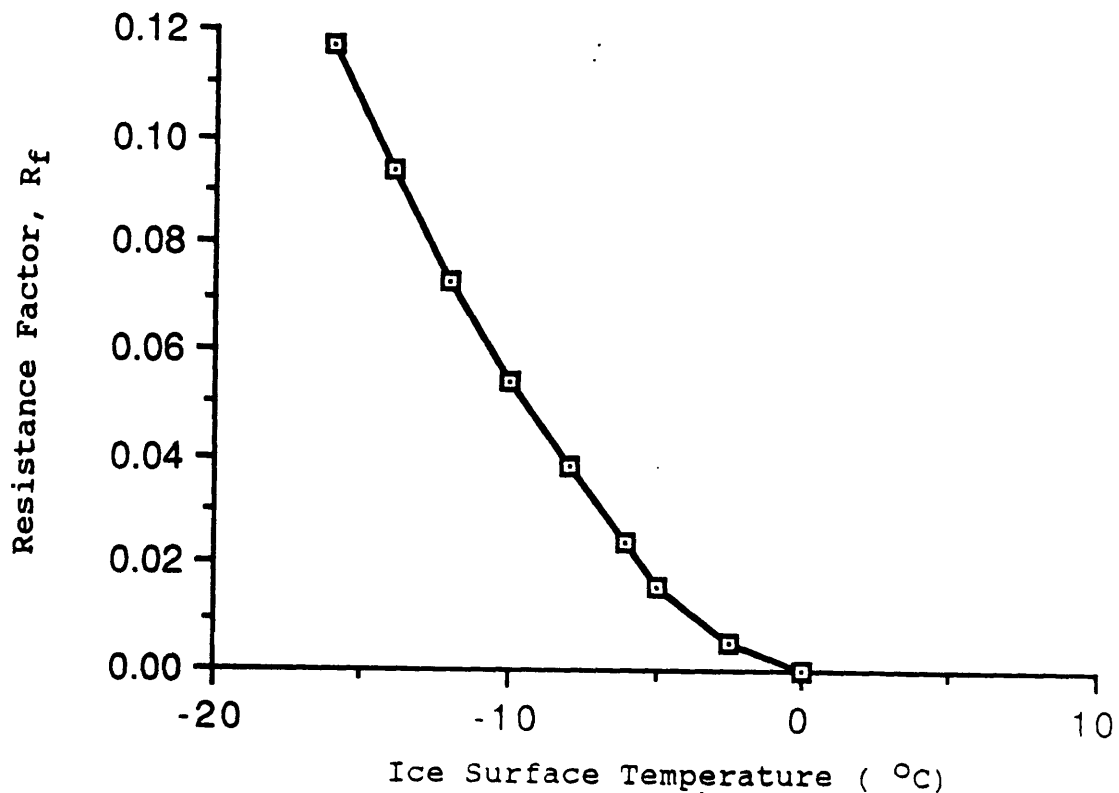
Figure 4-5   Temperature Variation of the Resistance Factor R_f for water on ice

temperature below freezing will significantly alter the mobility of water. Dry areas on a glaze ice surface will be subcooled below freezing and will impede or stop the flow of water across them. Stationary water beads surrounded by dry ice will freeze and generate a rough surface.

The investigation by Olsen et al[9] indeed showed that under certain glaze ice conditions there is a zone on the ice surface which is rough. In this zone, the roughness is generated by the gradual freezing of stationary water beads. The temperature dependence of the contact line resistance force for water beads on ice explains why water beads can remain stationary on an ice surface. The subfreezing temperature of the dry ice surrounding the water bead provides sufficient surface resistance to prevent their downstream motion.

The size of the droplets as they freeze will control the effective surface roughness for heat transfer enhancement. The stochastic nature of the process cannot be modeled exactly, however, useful information can be obtained by considering the limits which determine the maximum individual droplet height for a given location.

The temperature dependence of contact angle for water drops on ice allow the maximum height for a sessile water drop z_{max} at a given ice surface temperature to be calculated. This is shown as figure 4-6, z_{max} having been evaluated using:

$$z_{max} = (\ 2(\sigma/\rho g)(\ 1 - \cos\ \theta\ )\ )^{1/2} \qquad (4-1)$$

69
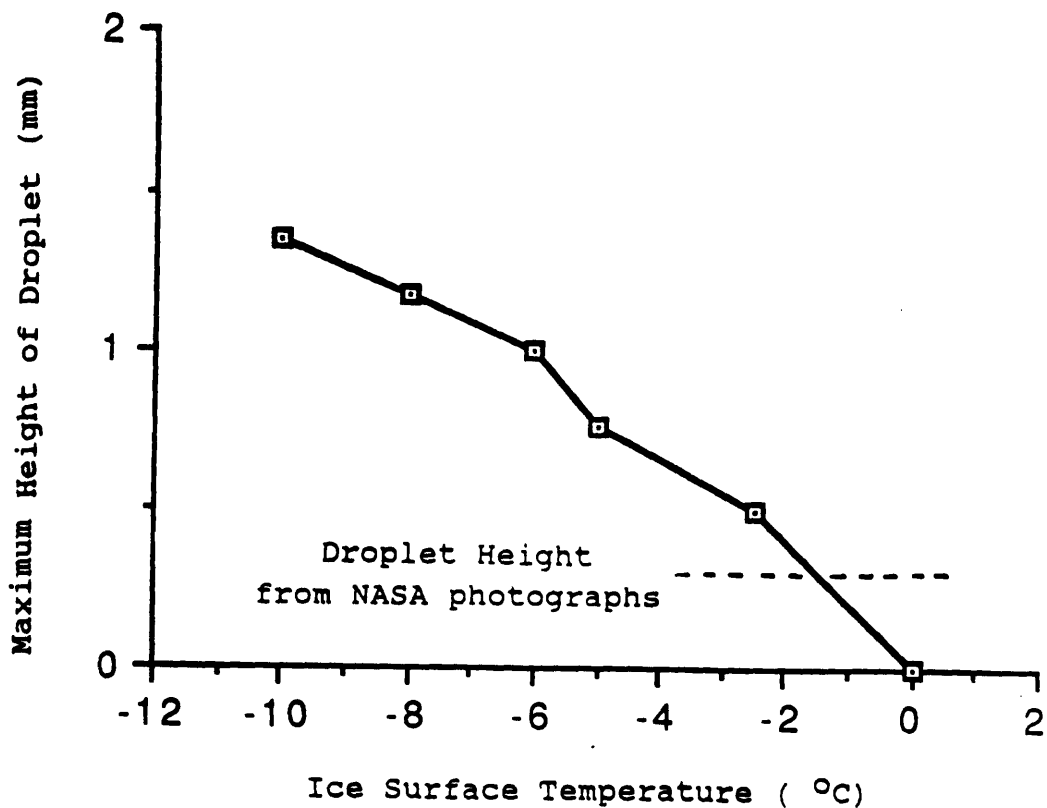
Figure 4-6   Maximum Sessile Droplet Height Variation with
              Temperature for Water on Ice

The maximum value of droplet height so generated will not
be the same as those for droplets exposed to external forces.
The external forces will deform the droplet from its static
sessile shape and alter its maximum height. However because
of the droplets constant volume the observed difference in
height from the static value will be small compared to the
overall height of the drop so that the static height should

be a reasonable approximation to the actual value. The

height of droplet predicted using this method is of the same

order as those measured from the photograph in figure 4-1 and

the values are included in figure 4-6. This would indicate

that the dry ice surface temperature is approximately $-3^{\circ}C$

which is of the same order as the freestream temperature used

in the run from which the photograph was taken.

4.3 <u>Measurements of the critical size for a water bead to</u>

<u>remain stationary when subject to a surface shear</u>

<u>stress.</u>

The behavior of water beads embedded in a boundary layer

as observed in the NASA films will depend on the forces

acting as described in Section 3.3. To examine how coalesced

water beads are stable (ie motionless) on a glaze ice

surface a simplified model was considered. A horizontal

laminar flat plate boundary layer flow was used. In this

arrangement there are no streamwise pressure gradients and

the force balance reduces to a relation between the surface

shear stress and the contact line resistance force. The

surface resistance F_{resis} is proportional to the droplet

diameter and on the resistance factor R_f determined by the

material composition of the flat plate. The external force

F_{aero} is proportional to the surface area of the bead and

dependent on the freestream velocity. For a given droplet

size there will be a critical freestream velocity for which

$F_{aero} > F_{resis}$ and the droplet will breakaway and move

downstream. By measuring this critical freestream velocity
to cause motion for different diameter droplets and for
different surfaces it is possible to investigate the
relationship between the water bead diameter, resistance
factor R_f and the freestream velocity below which the bead
will remain stationary.

4.3.1 Experimental setup & Method

The experimental investigation was conducted in the MIT
1' * 1' low turbulence wind tunnel. The experimental setup
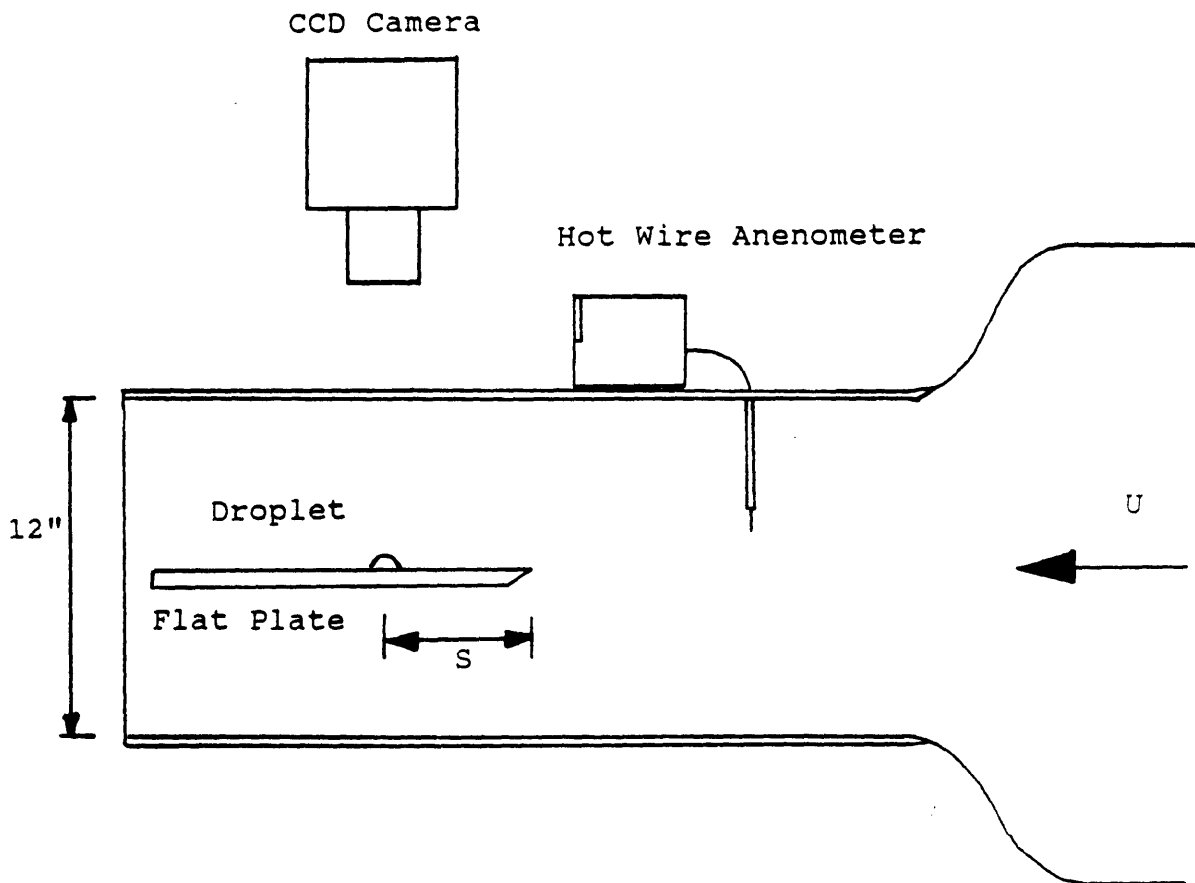
Figure 4-7   Experimental Arrangement Side View For Critical
Breakaway Droplet Size

used is shown in figure 4-7. The tunnel has a maximum

velocity of 80mph. Air speed measurements were made using a

calibrated hot wire anenometer. The flat plates used had a

sharp leading edge and were inclined at a slight negative

pitch (~3°) to prevent seperation at the leading edge. The

12" long plates were mounted at the tunnel midplane. The

combined blockage factor of the plate and mounting was less

than 5% of the tunnel cross-section. An 8mm CCD microvideo

camera with a macrolens could be mounted above or at the side

of the working section. This allowed the behavior of the

droplets prior and subsequent to motion to be observed. By

the use of two mirrors the velocity meter display was

included within the field of view of the camera.

Three different surfaces were used, the values of contact

angle and contact angle hysteresis are shown in Table 4-1.

Table 4-1   Contact Angle, Contact Angle Hysteresis, and
            Resistance Factor for Surfaces Examined

	Contact Angle	Contact Angle Hysteresis	Resistance Factor
Plexiglass	65°	22°	0.17
Aluminum	73°	38°	0.31
Matt Acrylic	62°	56°	0.42

Note that the values of R_f are high compared to those obtained for water on ice (see figure 4-5).

The aluminum surface was highly polished and the plexiglass was free of visible scratches or imperfections. Distilled water beads were placed using a micropippette at a distance of 4" from the leading edge. In some cases the droplets were placed at 8" to determine the effect of boundary layer thickness.

The droplet diameter was measured after placement using a direct read measuring telescope with a marked reticule. The droplet diameters were determined to an accuracy of 0.1mm. Any drops with non-uniform shapes due to placement were discarded. The tunnel was started and the velocity increased at a steady rate. The air speed at which the droplet started to move downstream was recorded. This process was repeated for a large number of drops with diameters in the range of 2mm to 10mm. This range was fixed by the accuracy with which droplets could be placed uniformly and measured.

4.3.2 Observations and Results

Figure 4-8 shows the critical breakaway velocity variation with diameter for the three surfaces investigated. All three curves have an inverse power law dependence on the droplet's diameter.

The single curve obtained in figure 4-9 were obtained by considering the force balance acting on a bead. The only forces acting are the surface shear stress due to the
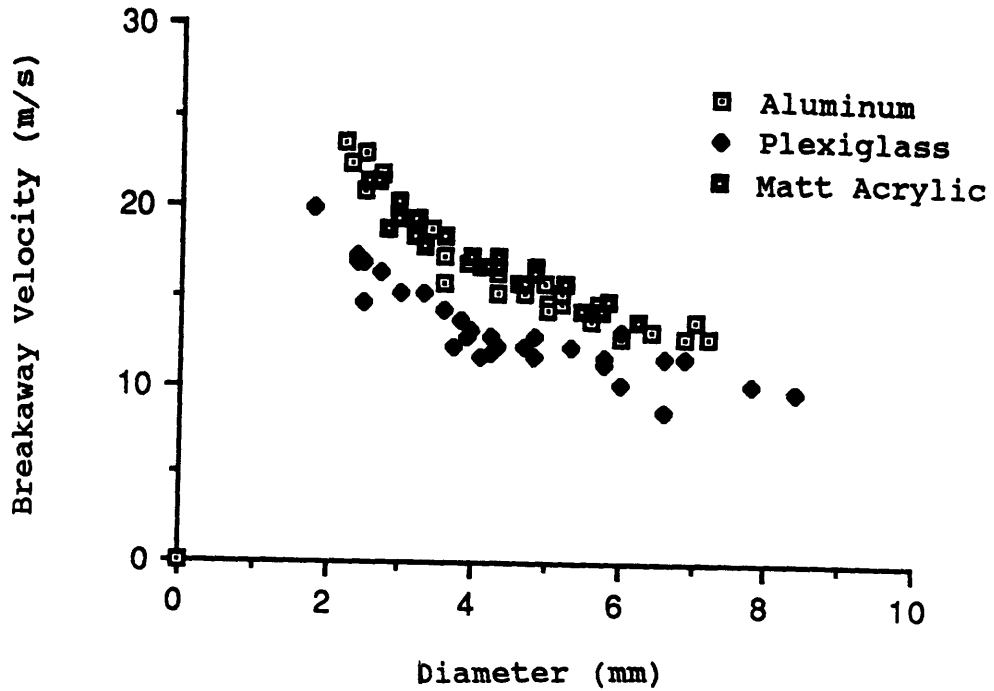
Figure 4-8   Critical Droplet Diameter Variation with
              Freestream Velocity for three surfaces
              investigated
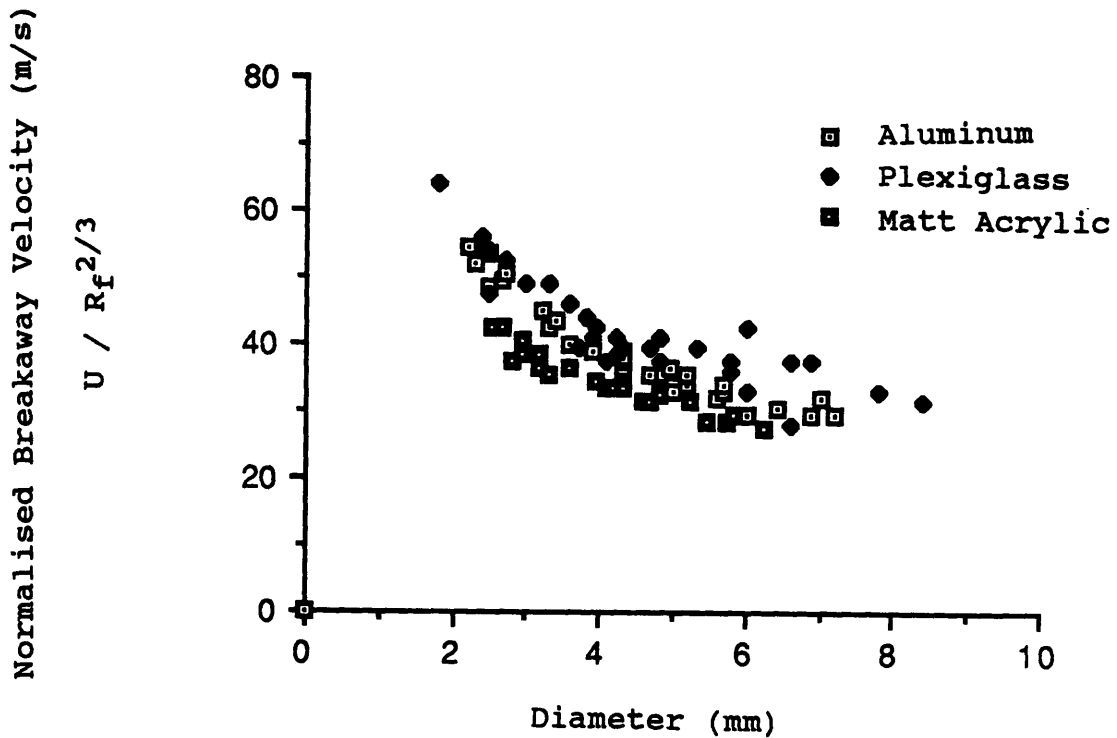
Figure 4-9   Breakaway Velocity normalised by

              Resistance Factor variation with droplet

              diameter

external flow and the contact line resistance force. The
surface shear stress is proportional to the surface area of
the bead and the velocity gradient at the surface of the
water drop. This velocity gradient can be approximated as
the value at the surface in the absence of the droplet. For
a flat plate boundary layer using Polhausen's[34] approximation
for laminar velocity profile then:

$$du/dy|_{y=0} = \frac{2 \; U^{3/2}}{5 \; (\nu s)^{1/2}}$$ (4-2)

Where s is the distance from the leading edge and the
kinematic viscosity of air. This then gives the total
aerodynamic force F_{aero} as:

$$F_{aero} \propto d^2 \; U^{3/2}$$ (4-3)

The surface resistance for a bead from section 3.3.1,
where the width of the contact line is taken to be the
droplet diameter d, is given by:

$$F_{resis} \propto 2 \; \sigma \; d \; R_f$$ (4-4)

Rearranging 4-3 and 4-4 to give the critical velocity for a
given diameter yields:

$$U_{crit} = C \left(\frac{\jmath}{d} \right)^{2/3} \left(\frac{s}{\rho \mu} \right)^{1/3} R_f^{2/3} \qquad (4\text{-}5)$$

Where C is a constant of proportionality. The data from the three surfaces of differing resistance factor, within experimental error in determining R_f collapse onto one line if the breakaway velocity is divided by $R_f^{2/3}$. The curve also show the $d^{-2/3}$ power dependence. For small values of the Resistance factor R_F the expression given as 4-5 reduces to a form similar to that derived by Dussan & Chow [30].

A value of C can be obtained from the measurements and will allow first order estimates to be made, for surfaces with a known resistance factor, of the maximum stationary droplet size for a given freestream velocity. The prediction is, however, restricted to flows where the boundary layer development is similar to that on a flat plate. The resistance factor of ice at $-5^{\circ}C$ is approximately 3% of that for the aluminum plate. This would correspond to the critical breakaway velocity for similar sized droplets being 10% of the breakaway velocity of water on aluminum. The smaller the resistance factor the smaller the critical droplet size. That is, for a glaze ice surface the colder the surface temperature the larger a droplet may grow.

Chapter Five

DIRECT COMPARISON ICING EXPERIMENTS

5.1 <u>Objective</u>

To experimentally investigate the dominant mechanisms
which control surface water behavior, it is necessary to
isolate each individual mechanism. A series of experiments
were conducted in the Data Products of New England icing wind
tunnel to examine the importance on ice accretion behavior of
the following:

(1) Thermal Properties of the uniced surface

(2) Surface Roughness of the uniced surface.

(3) Surface Resistance of the uniced surface

(4) Surface tension of the impinging water

By exposing two test articles, identical except for
either their surface roughness, thermal properties or surface
resistance to the same icing cloud it was possible to assess
the individual importance of these uniced surface parameters
on glaze ice accretion. The effect of surface tension
variation was observed by comparing two test runs where the
icing cloud variables were held constant and a surfactant was
added to the icing cloud water supply to reduce the surface
tension.

These direct comparison experiments held the geometry,

external flow field and icing cloud parameters constant. Any change in the ice accretion would therefore be due to the transient influence of the uniced surface or surface tension on the unfrozen water flow.

5.2 Experimental Setup

The tests were conducted in the Data Products of New England Icing wind Tunnel. The experimental setup is shown as figure 5-1. The tunnel was a closed loop refrigerated system with a 24" long and 6" square cross-section test area constructed from plexiglass. The test articles were 3" long, 1" outside diameter cylinders with a 1/4" bolt hole to allow assembly. Two of these cylinders were mounted horizontally and seperated by a thin circular splitter plate at the midplane of the tunnel. The splitter plate had a 1/8" cartesian grid marked on both sides to provide a scale reference for the photographic studies.

Three 8mm CCD microvideo cameras with a Macrolens for magnification were used in the photographic studies. Camera'a B and C in figure 4-1 were positioned to give grazing angle views of each cylinder. The centerline of each camera being in the same horizontal plane as the axis of the cylinder but at an angle to the cylinder axis of approximately 10°. These two camera's were focused on the cylinder leading edge close to the splitter plate. The depth of field was approximately 1". The third camera A was fixed above and upstream of the test article. The centerline of

CCD Camera A

SIDE

6"

40°

Splitter Plate

U

20"

CCD Camera C

PLAN

6"

Cylinder

U

CCD Camera B
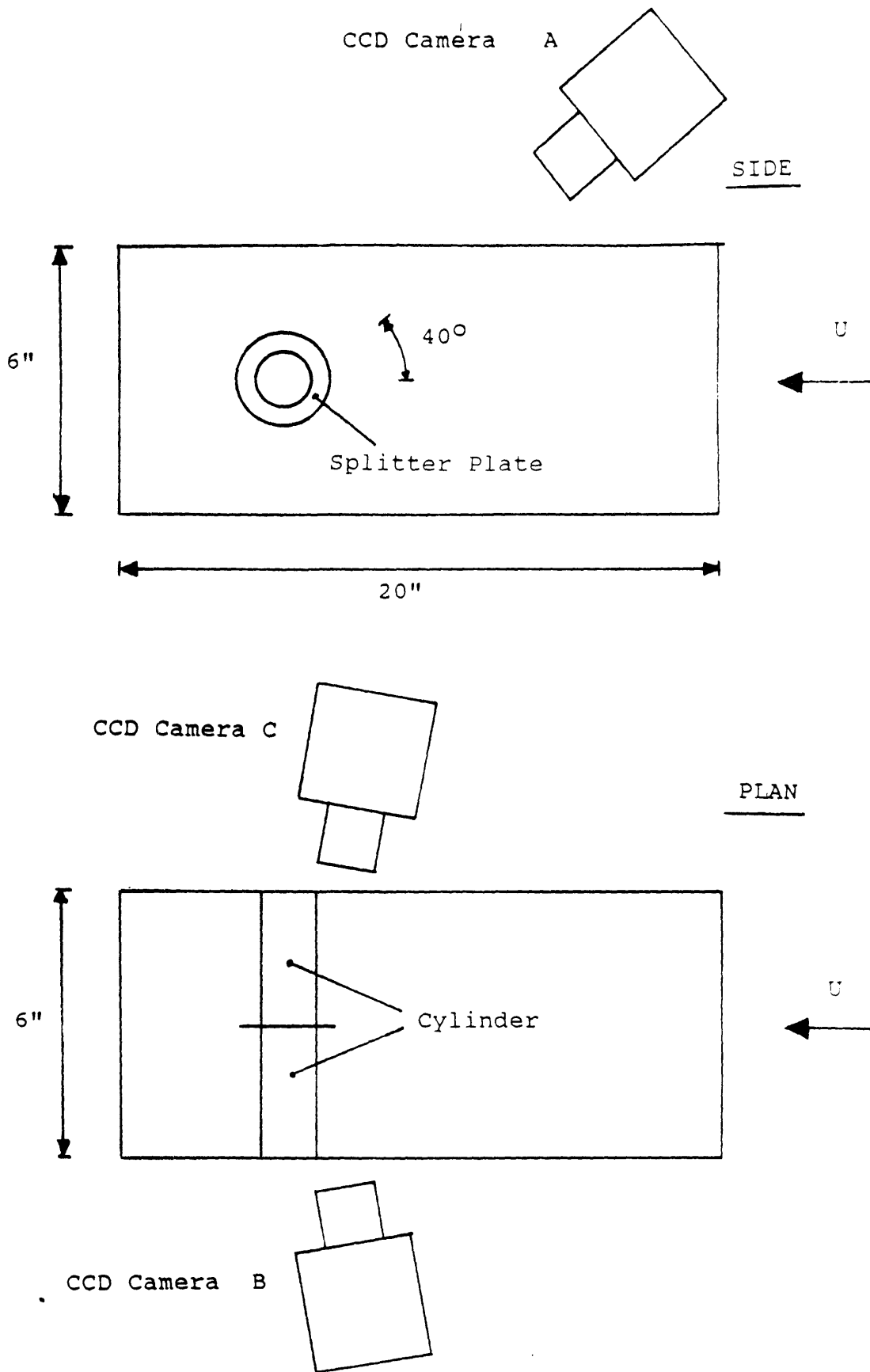
Figure 5-1   Schematic showing Side and Plan View of Experimental Set Up in Data Products Icing Wind Tunnel Test Section

the camera's optics was at an angle of 40° to the horizontal.
Camera A had the upstream face of both test articles in its
field of view. Slide photographs were also taken of
interesting features using a hand held 35mm SLR camera.
Secondary lighting was provided from the upstream end of the
working section and was adjusted to give a clear video
record.

5.3 <u>Test Conditions</u>

The icing wind tunnel was operated within a limited range
of glaze ice conditions. The freestream velocity could be
set at a series of discrete values and adjusted slightly
around these values. In the tests conducted velocities of
100Kts and 150Kts were used. The airstream temperature could
be lowered to a minimum of -10°C (dependent on external
atmospheric conditions). Tests were run at air temperatures
in the range of -4°C to -10°C. In steady operation, the air
temperature fluctuated at most by 0.6°C

The icing cloud was formed from a series of nozzles in
the tunnel chamber upstream of the test section. The
resulting icing cloud in the test section had a nominal
coverage of 50% of the tunnel crossection centered on the
centerline. Water was supplied to the nozzles by a gravity
feed. The average liquid water content of the tunnel had been
calibrated previously for the center 3" of the test area.
The mean volumetric diameter MVD of cloud droplets was
nominally 30 microns. The range of centerline averaged liquid

water contents used in these experiments were varied between
0.7 g/m^3 and 1.2 g/m^3.

To observe the actual distribution of liquid water
content across the test area the tunnel was run at the lowest
temperature possible. The spanwise ice distribution obtained
for this near rime condition (V=150 Kts , LWC=0.7g/m^3, and
T=-10.5^{o}C) is shown as figure 5-2. The ice thickness
accreted after 5 minutes exposure will be a rough indication
of the liquid water content distribution. Due to the
variation of LWC observed photographic observations were
focused on the centerline region where the ice deposit was
uniform and the liquid water calibration valid

Figure 5-2   Centerline Spanwise Ice Thickness Variation
Across Test Section

The water surface tension was altered by adding a surfactant to the cloud spray water supply. The surfactant (Kodak Photoflo 200) reduces the water's surface tension by approximately a factor of two while leaving the water's bulk properties (density, freezing temperature) unchanged. This was validated by measuring the freezing point of a Photoflo solution with a dilution of 1:200 which was the concentration used in the cloud water supply. Icing tunnel conditions were matched as closely as possible between runs with and without surfactant. Because the spray system was not specifically calibrated with Photoflo, some uncertainty exists on both liquid water content and nominal MVD values. Based on splitter plate ice accretion this uncertainty is estimated to be on the order of 5%. Photoflo runs were conducted at a liquid water content of $1g/m^3$ and for temperatures between $-9^{\circ}C$ and $-4^{\circ}C$.

A standard test procedure was used. After securing the cylinder assembly in position the tunnel was run until the air temperature and velocity had equilibrated to the desired value. All three microvideo cameras were started. The icing cloud was activated and simultaneously a strobe flash was discharged to identify the start of the icing exposure on the video record. At the end of the test run the cylinder assembly was removed and closeup slide photographs taken of the individual cylinder ice accretions. For the majority of tests the two cylinders were exposed to the icing cloud for a period of three minutes.

The video record allowed detailed observations to be made

of the surface ice development. Two types of analysis were used to obtain information from the video recording:

1) Final Ice Shape Profile

    The grazing angle camera's B and C gave a view which showed the near centerline ice profile with the scale reference cartesian grid as background. Use of a transparency fixed to a monitor allowed the final glaze ice shape to be directly traced from the video recording. The extent of the ice profile being clearly visible. The same method was used to obtain information from the overhead camera A.

2) Distinct Features on Ice Surface

    The position of distinct features on the ice surface could be measured directly from the monitor screen. Using the scale reference the angular position could then be calculated. The synchronising strobe flash at the start of the ice encounters allowed the time of exposure to be evaluated.

    A series of seventy test were conducted, the individual cloud conditions and cylinders used are listed in Appendix II. Figure 5-3 shows the spread of liquid water contents and tempertures examined for the 150Kts, 100Kts, and Photoflo test runs. The number of tests conducted allowed the repeatability of results to be examined. As icing is a stochastic process the ice profile obtained at the same conditions for two runs will not be identical, however, by examining a series of similar tests trends can be observed. Figure 5-4 illustrates the repeatability obtained for the

test conditions and setup used. It shows a comparison of two
test runs in which the icing conditons were held constant and
in which the position in the tunnel of the two test articles
was reversed. The final glaze ice shape for both test
articles are compared between the two runs. The final glaze
ice profile is also seen to be independent of the side of the
test area the test article was placed.
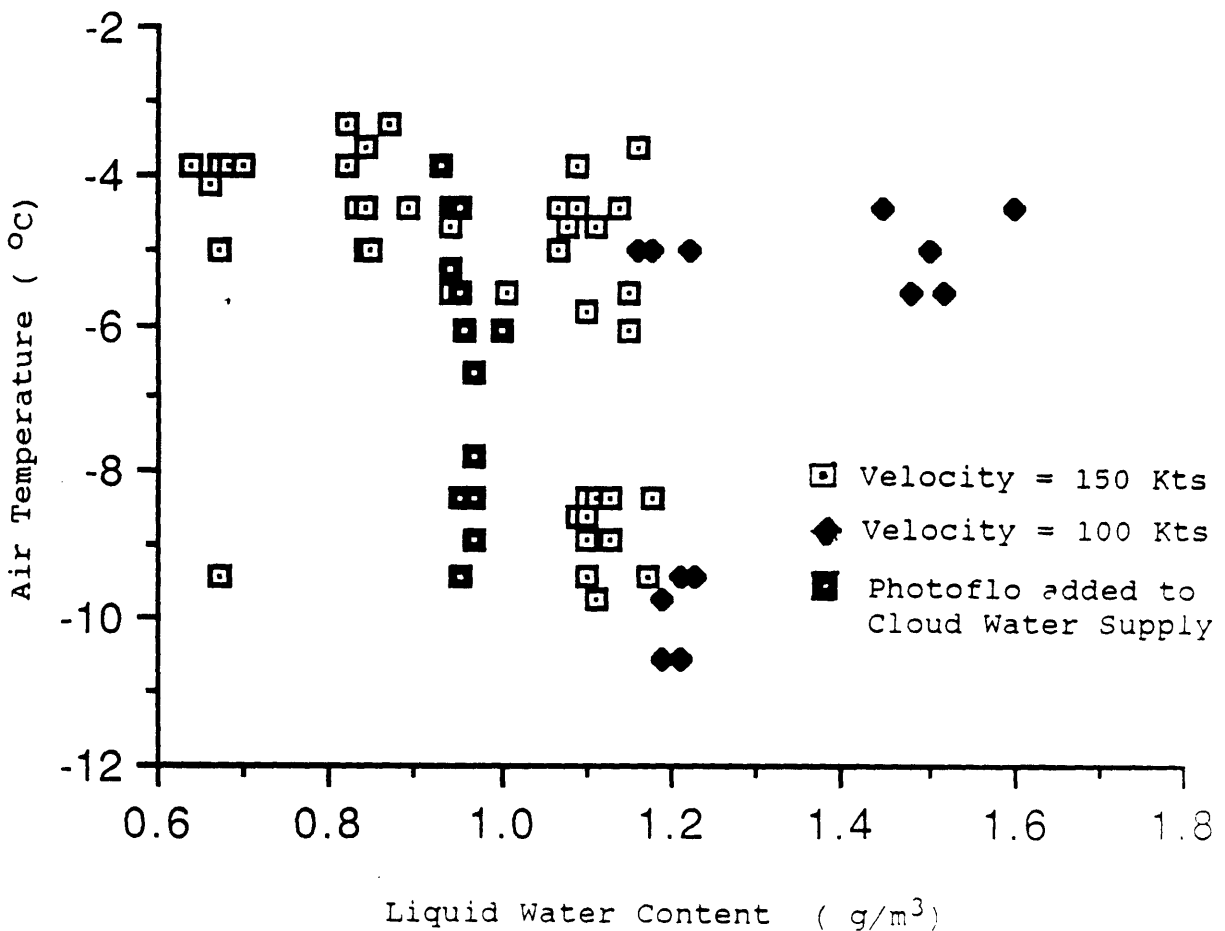
Figure 5-3   Experiment Test Runs: Range of Liquid Water
              Content and Temperature Invstigated

Test Article 1
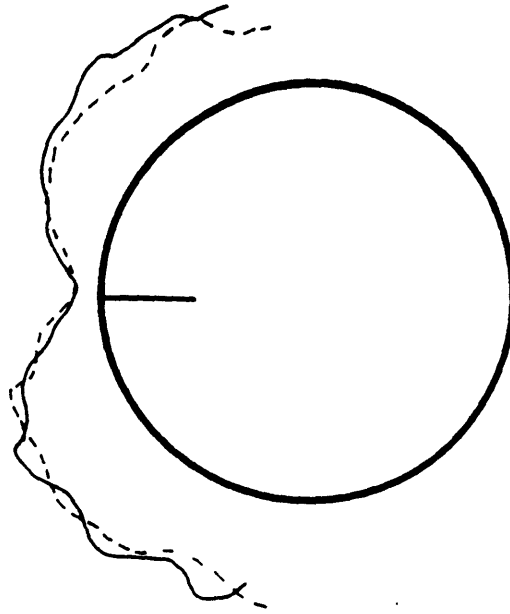
- - - - Run 1
———   Run 2

Test Article 2
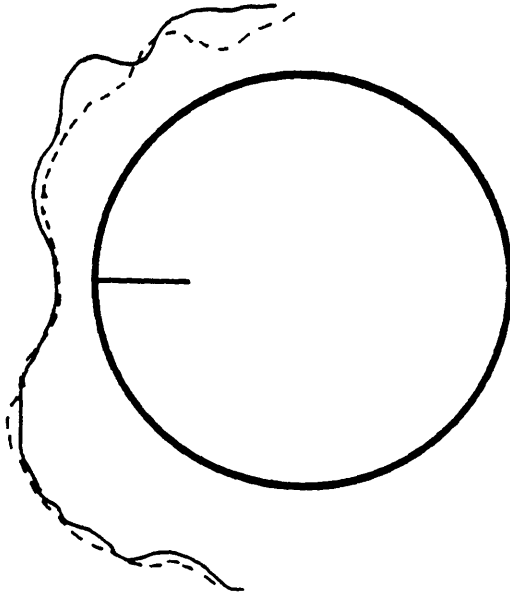
Figure 5-4   Repeatability of Final Glaze Ice Shapes for Two

Test Articles for two runs at the same

conditions

4.4 Observations of Glaze ice surface development

General observations of ice surface behavior were made at variety of icing conditions. Figure 5-5 shows two representative final glaze ice profiles for temperatures of

Runback

Rough

Smooth

$T = -4.5\ ^{O}C$

Rough

Smooth

$T = -9\ ^{O}C$
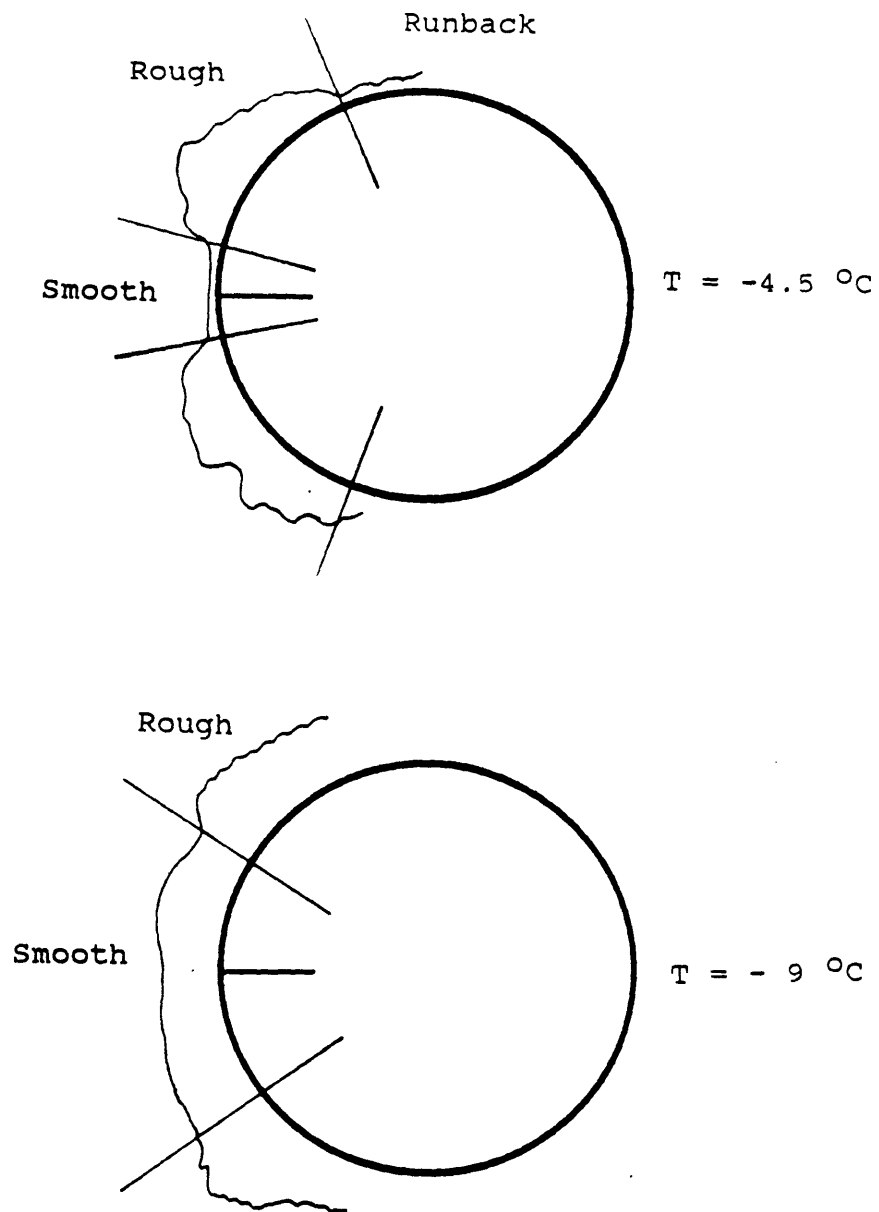
Figure 5-5   Typical Final Glaze Ice Shapes Showing Distinct Roughness Zones

-4.5°C and -9°C after a three minute exposure. During the ice accretion, three distinct types of ice surface behaviour were observed each having a characteristic roughness and identifiable boundaries. These were:

1) Smooth Zone

Close to the stagnation point, during exposure to the icing cloud the surface was observed by light reflection techniques to be uniformly wet with a thin film of water at warm temperatures. The surface in this region was smooth with no distinct roughness. The ice was translucent indicative of a slow freezing and glaze ice formation.

2) Rough Zone

At some point downstream, there was a sudden transition to a significantly rougher surface. Within this zone, there appeared to be insufficient water to maintain a uniform film. Surface tension forces dominated the water behavior. Runback did not occur, rather the water tended to coalesce into water beads as observed by Olsen et al[9]. The scale length of the roughness was typically of the order of 1mm. The transition between rough and smooth can be clearly seen in the grazing angle photograph shown as figure 4-1.

Insamuch, as there was a distinct boundary between the smooth and rough zones, this position could easily be identified on the grazing angle video recording. The angular position time history of this boundary is plotted in figure 5-6 for cold (-9°C) and warm (-4.5°C) conditions at a liquid water content of $1g/m^3$. The boundary started at
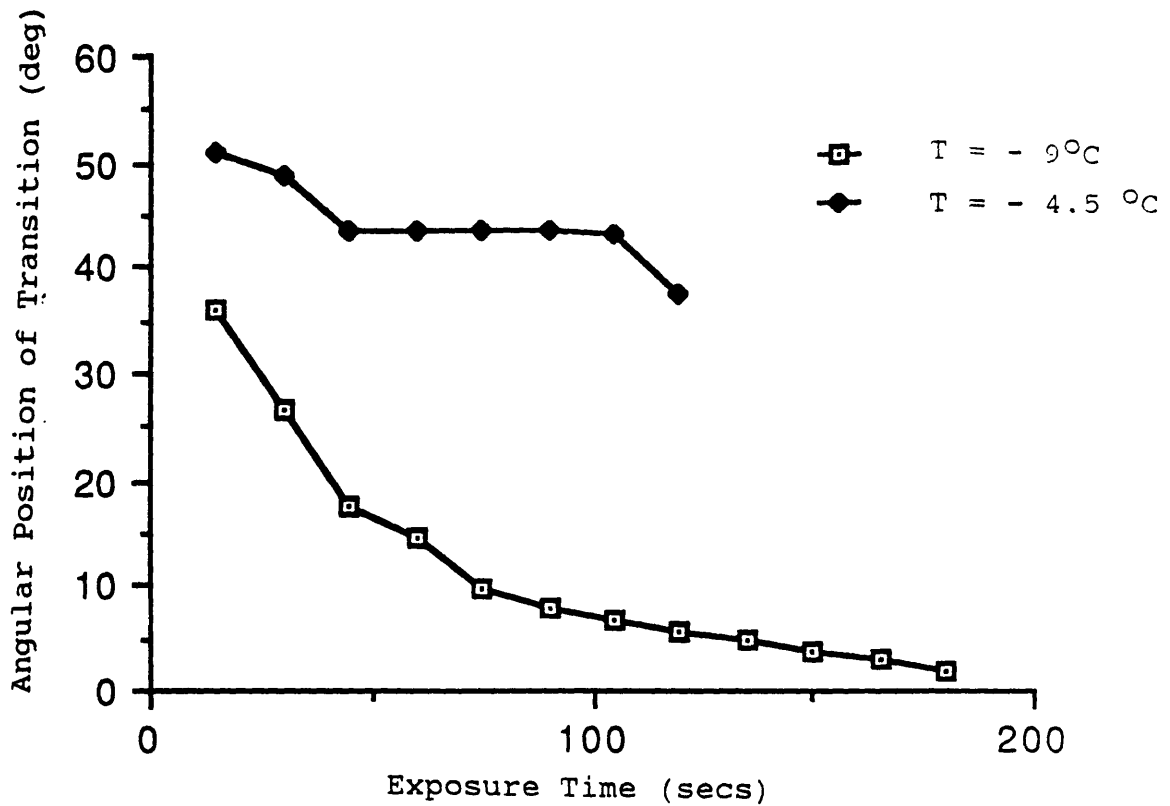
Figure 5-6   Angular Position Time History of Smooth- Rough
              Transition for Two Air Temperatures

approximately 50° and propagated rapidly towards the
stagnation region. The repeatible nature of the smooth-rough
transition's propagation towards the stagnation region
implies a distinctive underlying physical mechanism for the
transition between the surface water behavior in the rough
and smooth zones.

The ice accretion rate was observed to be enhanced in the

——— 150 Seconds
– – – 90 Seconds
—·— 30 Seconds

O Position of Transition
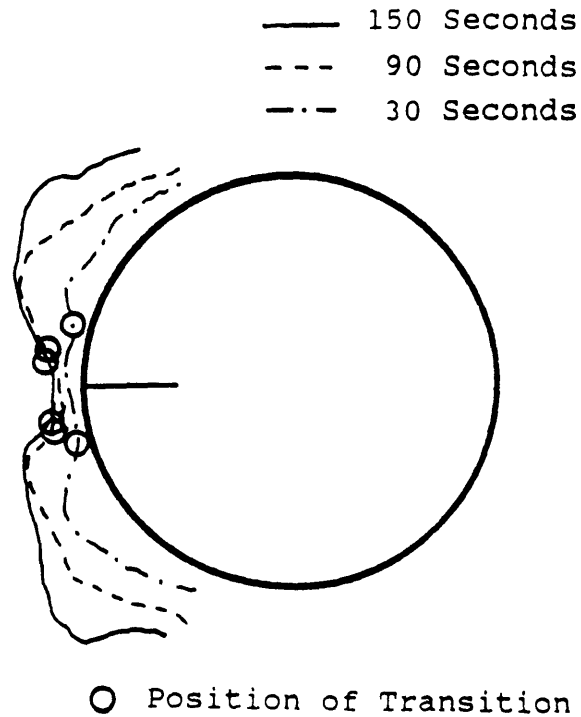
Figure 5-7   Time Development of Glaze Ice Shape

rough zone compared with the smooth zone. This can be seen
in the ice profiles of figure 5-7 taken from the video at
30,90 and 150 seconds after initial exposure to the icing
cloud. The enhanced accretion rate is thought to be due to
increased heat transfer resulting from the greater surface
roughness in this zone. In all the cases observed in this
study, the ice horns characteristic of glaze ice accretion
were found within the rough zone.

3) Runback zone

At warm temperatures a third zone was observed aft of the
rough zone. This region was characterised by streamwise

areas of ice interspersed with uniced surface. This ice was observed to form during an initial tansition period after cloud exposure. The ice was translucent and quite often frozen rivulets could be discerned. In warm conditions and at high liquid water contents, the surface water was observed to runback initially and then stagnate at the point of flow seperation. This water then slowly froze as rivulets or large coalesced water cells. Once a significant amount of ice began to form in the upstream "rough" zone no additional surface water was supplied to the runback zone and no further accretion occured.

5.5 Effect of the initial uniced surface on water behvaior

Table 5-1 lists the properties of the 9 cylinders used in the investigation of the initial uniced surface effects.

The two primary cylinders used in the thermal comparison experiments were; a copper tube with a 1/16" wall thickness to investigate fast thermal response; and a solid plexiglass rod to investigate slow thermal response. Tests were also run with a 1/8" wall thickness plexiglass tube and an aluminum cylinder. To remove the possible influence of surface resistance effects each cylinder was covered with a single coat of gloss acrylic paint. The copper cylinder had the largest thermal conductivity (394 J/KgK) and the plexiglass the lowest (17 J/KgK).

The roughness comparison used two cylinders. Both were manufactured from solid aluminum rods. One cylinder was

Table 5-1.   Thermal Properties and Surface Preperation of Test Articles used in Direct Comparison Experiments

Material/Surface

THERMAL			Thermal Conductivity k, [W/mK]	Specific Heat Capacity c_p [j/KgK]	Thermal Mass [Kj/Km]
1	Copper Tube	Gloss Acryllic	386	394	23.6
2	Aluminum	"	202	896	70
3	Plexiglass	"	16.7	1672	72.2
4	Plexiglass Tube	"	16.7	1672	34

ROUGHNESS

5 Aluminum   Polished surface using '0000' emery

6 Aluminum   Knurled element geometry as fig. 5-8

SURFACE RESISTANCE			Contact Angle	Contact Angle Hysteresis	Resistance Factor R_f
7	Aluminum	Gloss Acrylic	67°	59°	0.45
8	"	Matt Acrylic	62°	56°	0.42
9	"	Wax	68°	36°	0.28

constructed with an extremly smooth finish polished with

'0000' emery paper. The other cylinder was constructed with

a repeatable surface pattern produced by knurling the

cylinder on a lathe. The knurling process produces a pattern

of trapezoidal surface elements, an example of which is shown

as Figure 5-8. The roughness element used had a height Of

0.8mm, a width of 1mm, and a length of 2.7mm.
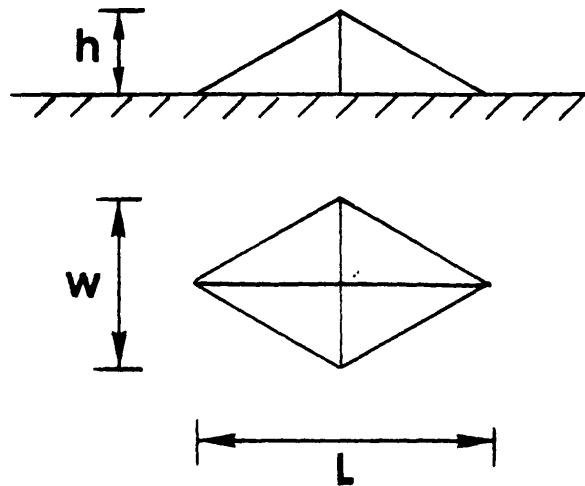
h = 0.8mm   w = 1mm   L = 2.7mm

Figure 5-8   Trapezoid Knurled Element Definition

In the examination of surface resistance, three cylinder

surfaces were used; gloss acrylic paint; flat acrylic

paint; and waxed surface. Each cylinder was manufactured

from solid aluminum. The contact angle, contact angle

hysteresis measurements and resistance factor R_f are

documented in Table 5-1. The waxed surface had the lowest

surface resistance of 0.28 and the gloss acrylic the highest of 0.45. These values were measured using the method described in Section 4.2 and should be considered as first order measurements.

5.5.1 Results

(1) Thermal Comparison

The water surface behavior after initial exposure to the icing cloud was observed to differ between the copper and the plexiglass articles. For the copper cylinder there was relatively little surface water flow prior to freezing and the initial ice surface was relatively smooth. This implies that because of the high conductivity of copper the initial water on the surface freezes more rapidly because of heat conduction into the surface Q_{cond}. For the plexiglass, bead coalescence and runback were observed prior to the initial ice formation. The gradual freezing of these beads resulted in a significantly rougher initial ice surface which is thought to be the cause of the slight difference in the accretion behavior. At cold temperatures the initial ice formed on the copper had a rime appearance indicative of rapid freezing and a high initial heat transfer.

Figure 5-9 shows a typical comparison of the final ice shape obtained after 3 minute exposures for both the copper tube and the plexiglass rod. This example was run at a temperature of -5.5°C and a liquid water content of 0.95g/m^3.

- - - Plexiglass
—— Copper

$T = -5.5\ ^\circ C$

$LWC = 0.95\ g/m^3$
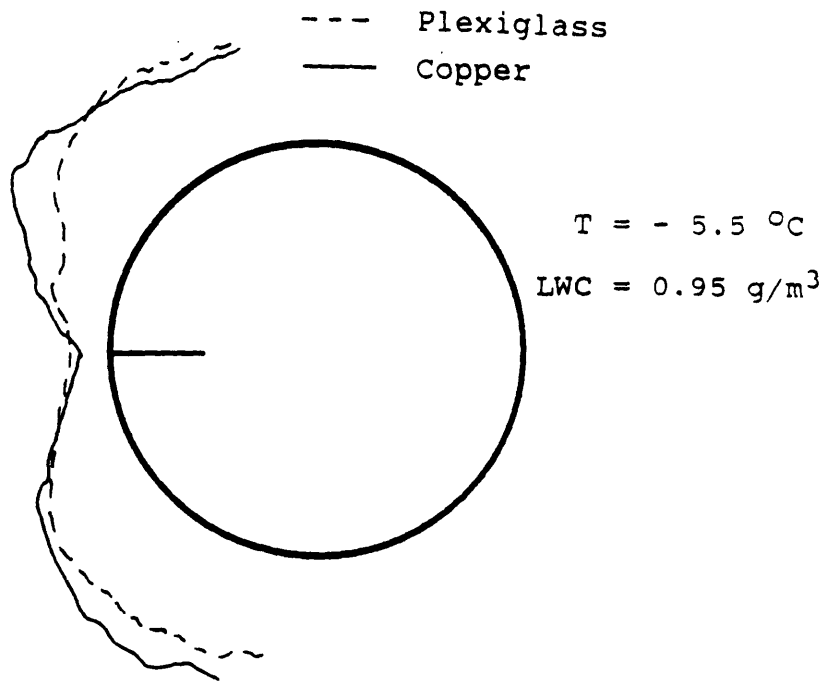
Figure 5-9   Typical Final Ice Shape Comparison for Copper
and Plexiglass Cylinders

The glaze ice horns on the copper cylinder were more sharply
defined than on the plexiglass which had a relatively flat
front surface and was slightly thicker in the stagnation
region.

The angular position of the transition between the
smooth-rough zones is shown as a function of exposure time
for these accretions in figure 5-10, the result for the
aluminum cylinder run at similar conditions is also included.
The results show a relationship between the thermal time
response of the cylinder and the rate at which the transtion

moves toward the stagnation point. For the plexiglass
cylinder with its low thermal conductivity, the smooth zone
shrinks much more rapidly than for the copper and aluminum.
The solid aluminum because of its larger thermal mass
conducts more heat than copper and consistent with the
plexiglass result its transition moves at the slowest rate.
The ice surface on the plexiglass cylinder became uniformly
rough after 45 seconds, however, the stagnation region still
appeared to have a film flow of water the reflection of light
showing it to be wet.
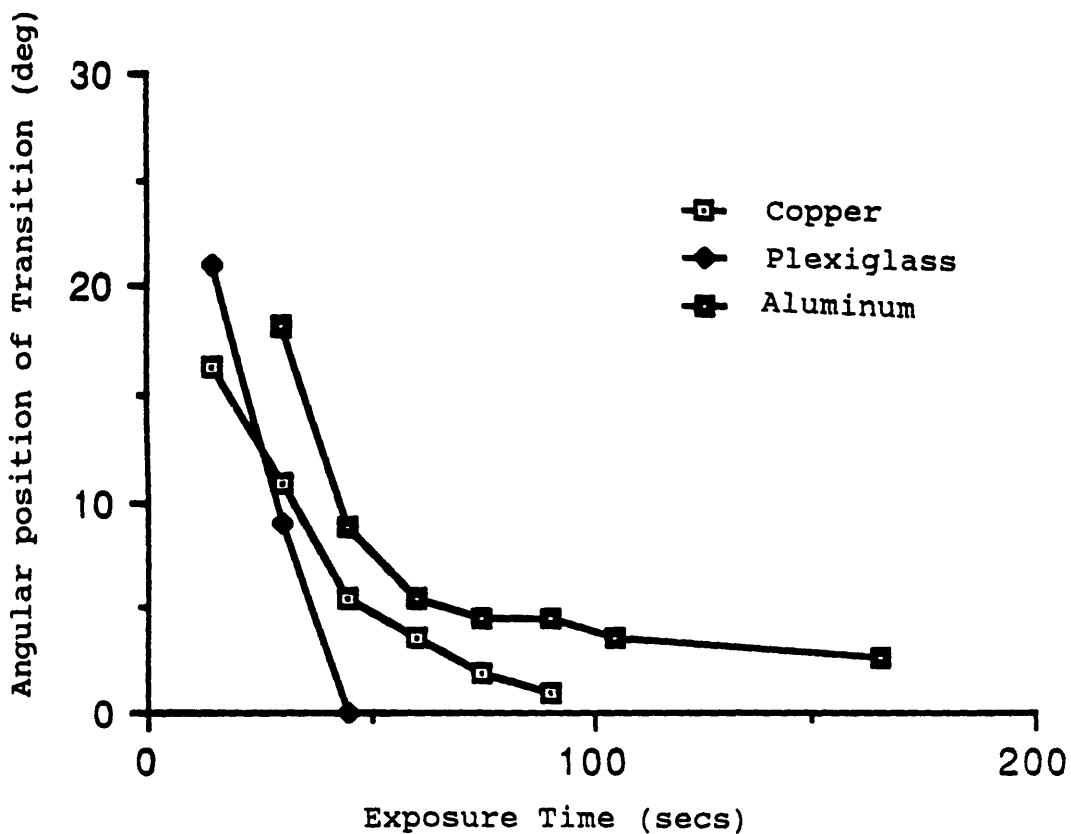
Figure 5-10   Angular Position Time History of Smooth-Rough
               Transition for Copper, Aluminum, and
               Plexiglass Cylinders

In general, the differences in the ice accretion behavior due to the substrate thermal properties were observed to be most significant during the initial phase of ice accretion. As the accretion grows the effect of the different initial conditons tend to wash out. After extended icing encounters the accretion will tend towards a shape controlled by the environmental parameters and the properties of the ice and rather than those of the substrate.

(2) Uniced Surface Roughness

A typical comparison of final ice profiles for the polished (smooth) and knurled(rough) cylinders is shown as figure 5-11. The rough zone on the knurled cylinder were broader and started closer to the stagnation line than for the polished cylinder.

A striking feature of the ice accretion on the knurled cylinder was the propagation of the trapezoid roughness elements into the ice surface in the rough zone. However, in the smooth zone close to the stagnation point the ice surface did not repeat the trapezoid pattern.

An assymmetry is observed in the polished cylinder ice growth between the upper and lower surfaces. This is thought to be due to the smooth surface on the polished cylinder allowing gravity to influence the surface water flow near the stagnation point, resulting in more water flowing to the lower surface.
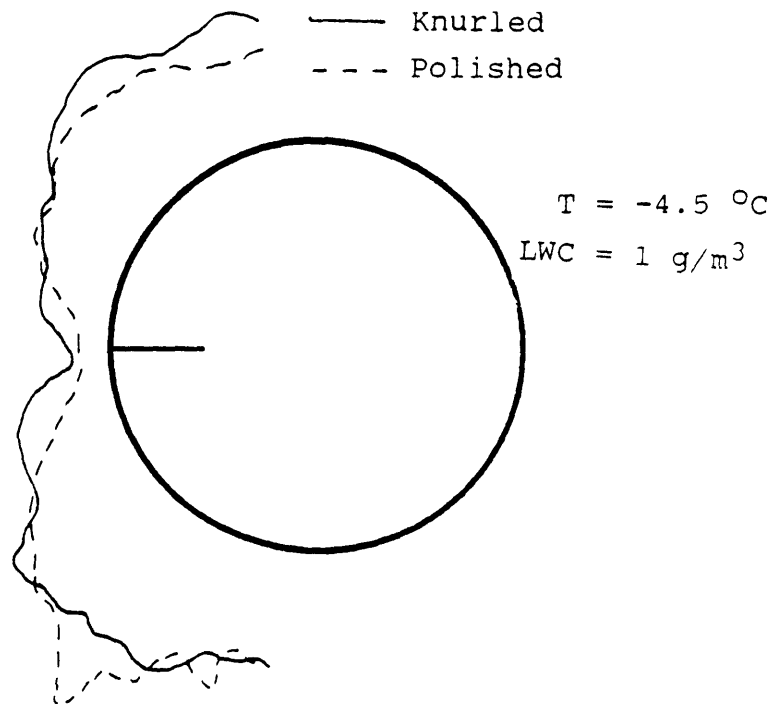
Figure 5-11   Typical Final Ice Shape Comparison for Polished
and Knurled Cylinder

The zones of smooth and rough ice growth discussed in
Section 5.3 were observed in both the polished and knurled
cases. Figure 5-12 plots the angular position of the
transition versus time.

Initially the transition moves at the same rate for both,
however, after about 60 seconds the rough zone for the
knurled cylinder still moves at a constant rate while for the
polished surface the rate of progression slows down. The
larger growth of the rough zone close to the stagnation point
for the knurled cylinder is indicative of heat transfer
enhancement in its rough zone. This may be explained by the
observation that the trapezoidal element pattern of the
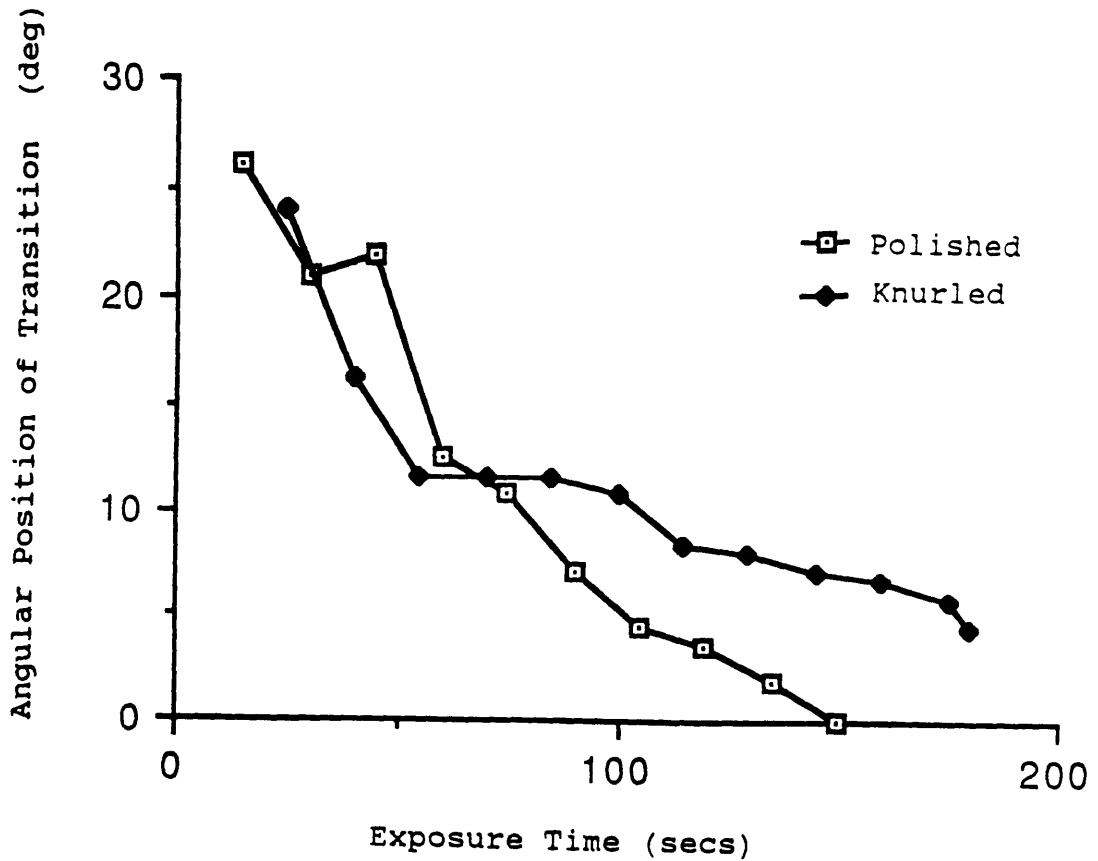
Figure 5-12   Angular Position Time History of Smooth-Rough

Transition for Polished and Knurled Cylinder

uniced knurled cylinder was clearly apparent in the ice

accretion within the rough zone.   The trapezoids enhance heat

transfer[18] more effectively on the knurled surface than on

the polished where the roughness is generated by the

hemisphere like water beading mechanisms.

(3) Uniced Surface Resistance

Figure 5-13 shows the final ice shape comparison for two

combinations of cylinders; the gloss and matt acrylic paint

surface; and the matt acrylic paint and waxed surface. The

Matt Acrylic Paint
Wax

T = -5.6 °C

LWC = 0.95 g/m³

Gloss Acrylic Paint
Matt Acrylic Paint

T = - 5 °C
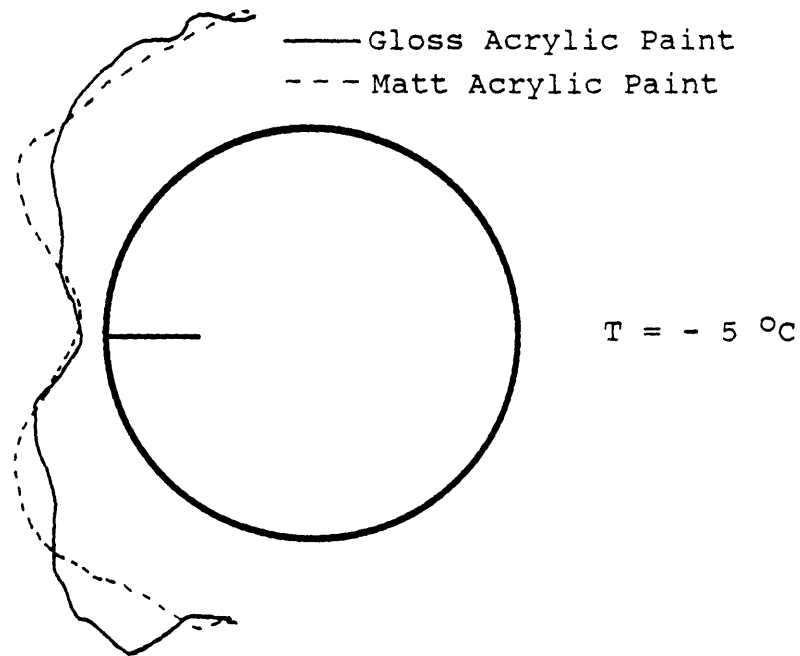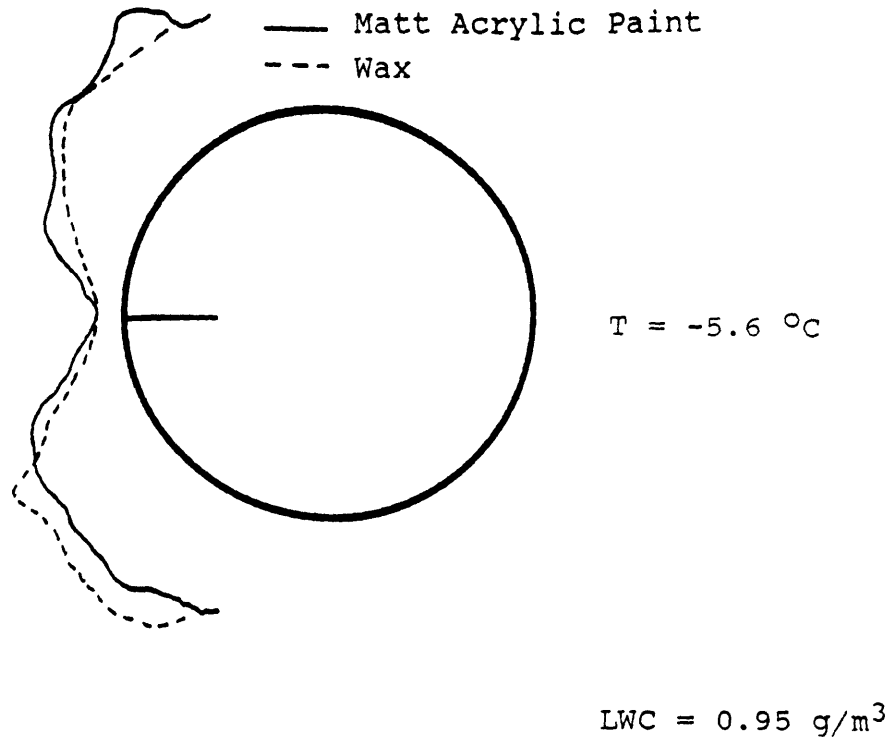
Figure 5-13   Typical Final Ice Shape Comparison for Matt &
Gloss, and Matt & Waxed Surface Cylinders

differences in final form was slight and of the same order of the repeatability of the tests (see figure 5-4). The similarity of the final glaze ice shape is thought to be due to the initial effects of the surface resistance washing out rapidly. Also, the difference in resistance factor R_f between the individual surfaces used was small compared to the differences to the surface resistance of water on ice shown in figure 5-5 (R_f =0.12 for ice at T=-10°C). Therefore, once ice has formed the behavior of water on ice will control the mode of transport and there will be no further influence of the uniced surface's resistance.

Figure 5-14 shows the angular position of the smooth-rough transition for the two sets of cylinders. Although the final ice formations are similar there is a difference in behavior during the initial phase of ice accretion. For the smooth-rough transition the smaller the resistance factor of the uniced surface the further forward the transition is at a given time and the earlier it reaches its asymptotic position. This is observed for both the comparisons where the transition is always located further downstream on the gloss surface (R_f=0.45) compared to the transition on the Matt (R_f=0.42). The rough zone grows most quickly for the wax surface (R_f=0.28) which has the lowest resistance factor. This indicates that the lower the initial uniced surface resistance the more quickly the rough zone develops. More water is supplied earlier to the roughness zone to form the stationary water beads. It is the freezing of the water drops which enhance heat transfer

$T = -5.6\ ^\circ C$

$LWC = 0.95\ g/m^3$

$T = -5\ ^\circ C$
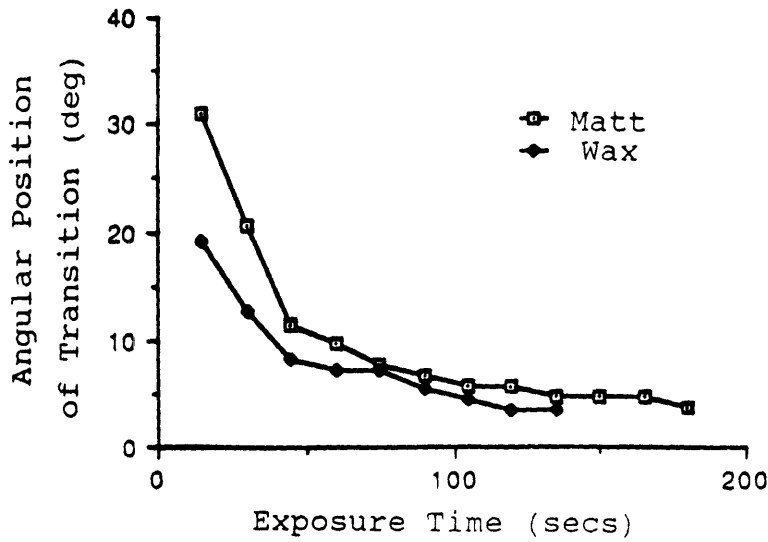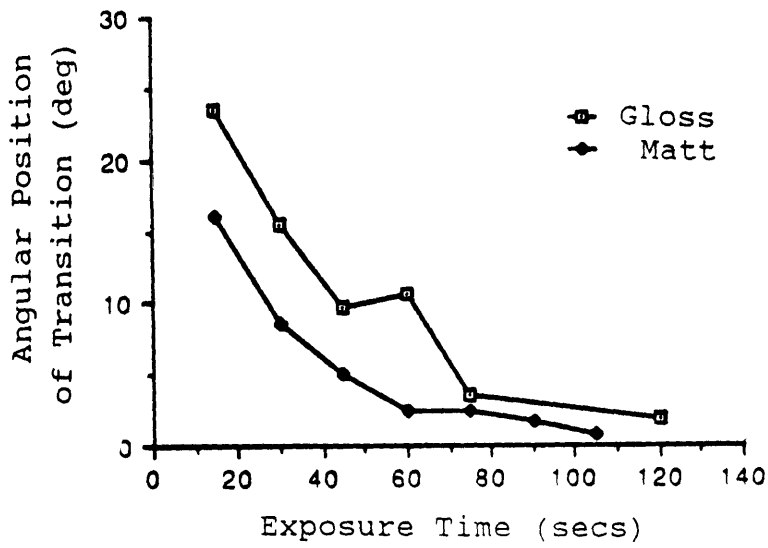
Figure 5-14   Angular Position Time History for Smooth-Rough

Transition for Matt & Gloss, and Matt & Wax

Cylinders

5.6 Surface Tension Effects on Glaze Ice Accretion

The importance of surface water behavior was investigated
in a different manner by reducing the surface tension of the
cloud spray water supply. This was accomplished by the
addition of Photoflo, which halved the surface tension, and
studying the effect on the resulting ice accretion. Final
glaze ice profile comparisons between normal icing cloud and
the Photoflo modified cloud exposures are shown in figure
5-15 for the copper cylinder. The addition of Photoflo
resulted in an opaque white ice with a smaller scale surface
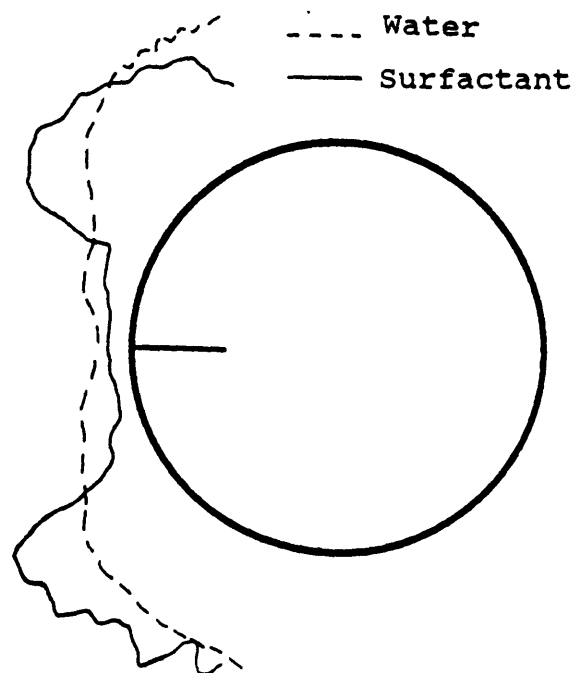
Figure 5-15   Typical Final Ice Shape Comparison for Cloud
              water Supply with and without Surfactant

roughness and a significantly different profile than for the normal cloud. The horns were more pronounced and sharply defined. Figure 5-16 shows Photoflo ice profiles for the copper cylinder at three values of temperature. At the lower temperature, the glaze ice horn has become so pronounced that it no longer collected all the impinging water and a second horn was therefore able to develop behind it.

Figure 5-17 shows the time history of the smooth-rough transition for the Photoflo and normal icing cloud. The transition for the Photoflo cloud is always located aft of that for the normal icing cloud during the initial transient phase its asymptotic position is further away from the stagnation point. The reduction of the surface tension results in a lower initial surface resistance. However, the surface tension is not a transient effect and will also reduce the surface resistance of water flow on the ice surface. It also controls the maximum height and size of the stationary water beads in the rough zone. The lower surface resistance of Photoflo explains the smaller scale roughness observed in the rough zone. The smaller scale roughness for Photoflo will not enhance heat transfer as much as the larger water beads on the normal ice surface and this appears to be important in determining the position of the smooth-rough transition. This is consistent with the surface roughness size controlling the location of the transition observed for the knurled and polished cylinders. A possible explanation for the more pronounced development of the horns is that the reduced surface tension supplies more water to the rough zone

LWC = 0.95 g/m^3

T = - 5 ^{o}C

T = - 7°C

T = - 9 ^{o}C
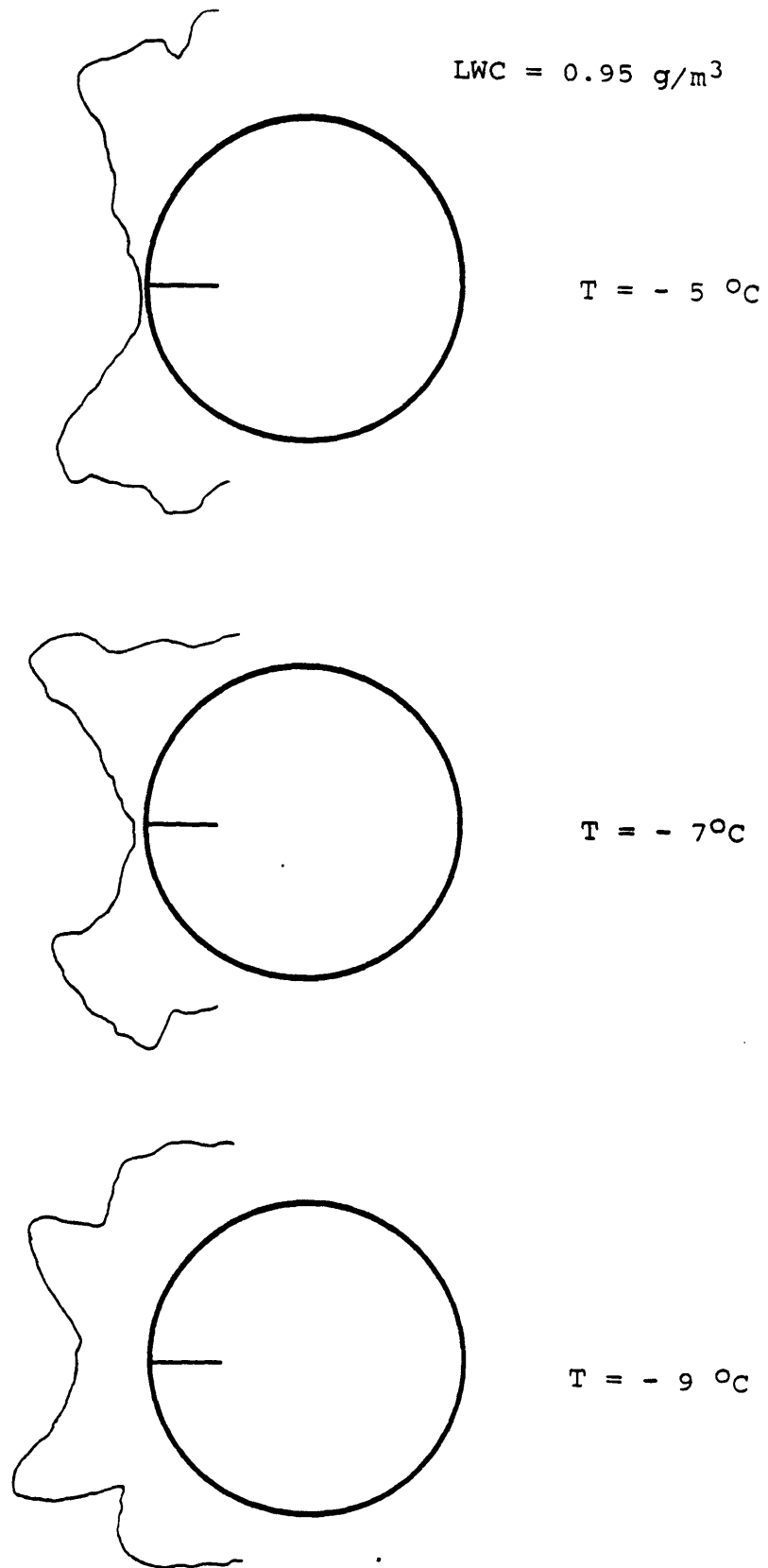
Figure 5-16   Effect of Air Temperature Variation on Final
Ice Shape with Surfactant Added to the Cloud
Water Supply
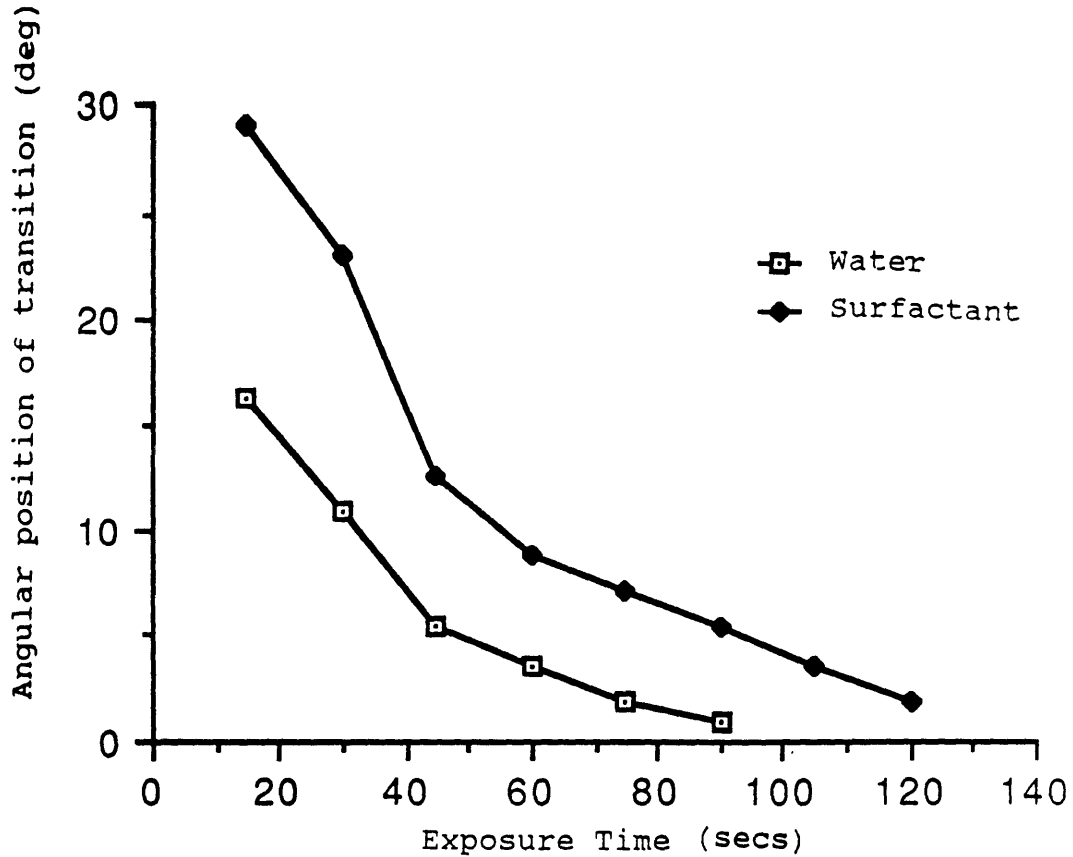
Figure 5-17   Angular Position Time History of smooth-rough
               Transition for Cloud Water Supply with and
               without Surfactant

and allows the horns to grow more rapidly and collect more impinging mass by protruding into the external flow.

The different and unusual ice accretions obtained at a reduced value of surface tension is additional evidence that surface water behavior is an important factor in the glaze ice accretion process and must be considered in physically realistic models.

5.7 Parametric Study of Smooth-Rough Transition

One of the unique features of this investigation has been the observation of the transition between the smooth and rough zones of accreting ice surface. The results obtained for the aluminum test article with the gloss acrylic paint surface were used to examine the effect of liquid water content, air temperature, and velocity on the behavior of the smooth-rough transition.

WET: LWC = 1.1 g/m^3 T = - 4.5°C

DRY: LWC = 0.7 g/m^3 T = - 9 °C
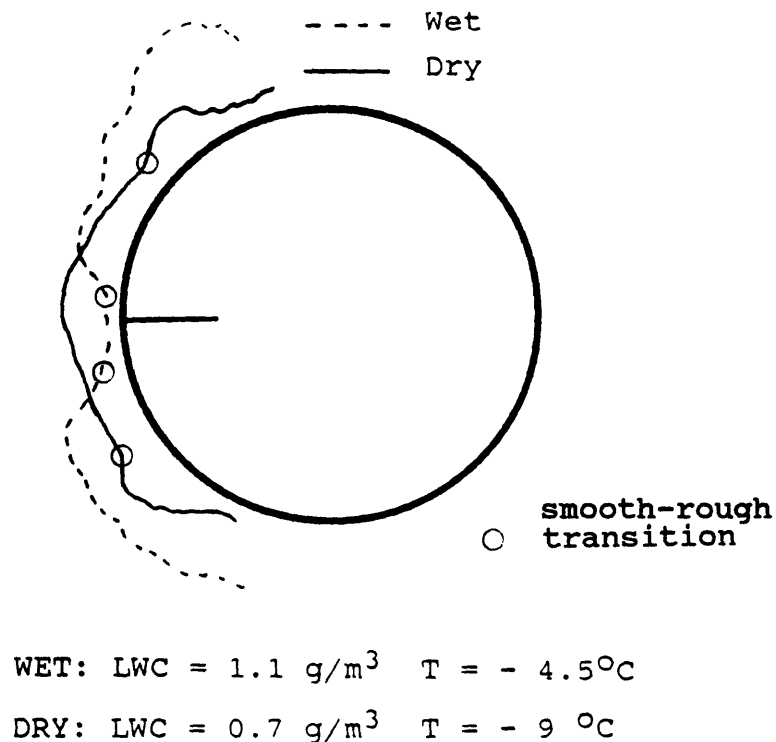
Figure 5-18   Typical Final Ice Shape Comparison for "wet" (high LWC and T) and "dry" (low LWC and T)

Figure 5-18 compares ice accretions obtained at "warm"
($T=-4^\circ C$) and high impinging mass ($LWC=1.2$ g/m^3), and "cold"
($T=-10.5^\circ C$) and low impinging mass ($LWC=0.7$g/m^3) conditions.
These conditions will be refered to as "wet" and "dry"
respectively. This designation is used because for "wet"
conditions there will be more unfrozen water at the
stagnation point than for "dry" conditions. An interesting
observation is that for the "wet" case the smooth-rough
transiton is located close to the stagnation point, whereas
it is barely discernable for the "dry" case being located
aft. As the freestream velocity is the same for both cases
the laminar heat transfer coefficient in the stagnation
region will be the same and Q_{conv} will therefore be
correspondingly greater for the lower air temperature. This
is seen in the greater ice accretion in the smooth zone for
the "dry" conditions. However, the smooth-rough transition
is near to the stagnation point for the "wet" case and
consequently there is more ice accretion for this position
than for the "dry" case. This implies that there is heat
transfer enhancement in the rough zone which gives rise to
the greater ice accretion and consequently that the boundary
layer flow in the rough zone is turbulent

Figure 5-19 shows the time history of the angular
position of the smooth-rough transition for variation with
air temperature, velocity, and liquid water content. For each
comparison the other two cloud variables were constant. The
three plots show that increasing the amount of water arriving
at the surface (high velocity and high liquid water content)
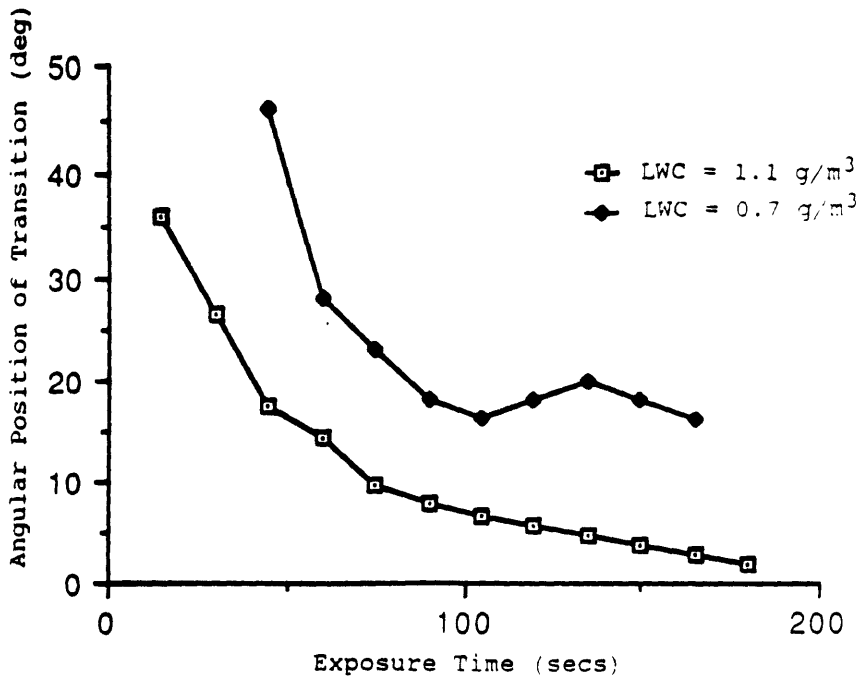
a) Variation with Liquid Water Content

Figure 5-19   Angular position Time Histories for smooth-
rough transition variation with LWC, T and U
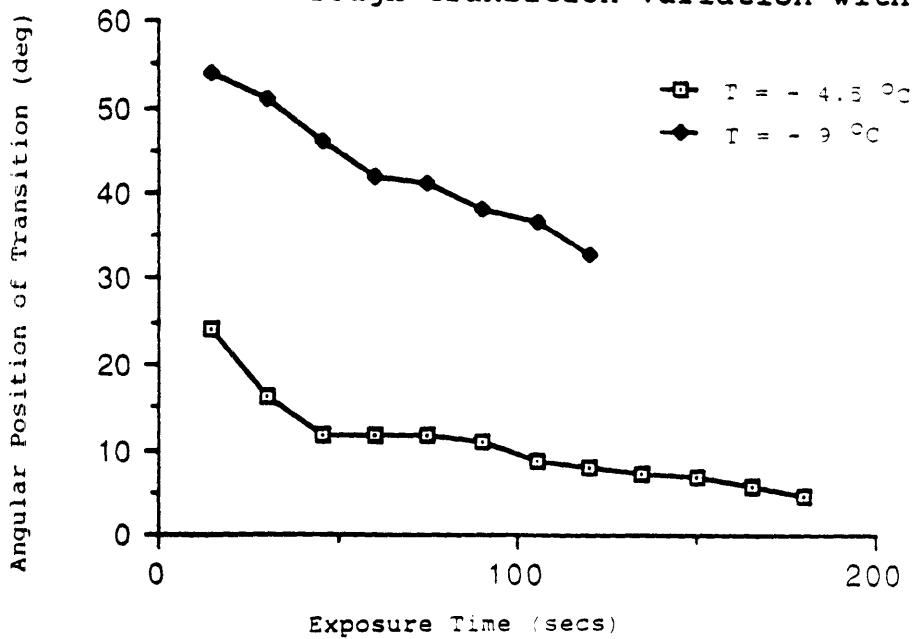
b) Variation with Air Temperature

Figure 5-19   Angular position Time Histories for smooth-
rough transition variation with LWC, T and U

109

Angular Position of Transition (deg)

80

60

□ U = 100 Kts
◆ U = 150 Kts

40

20

0

0   100   200

Exposure Time (secs)
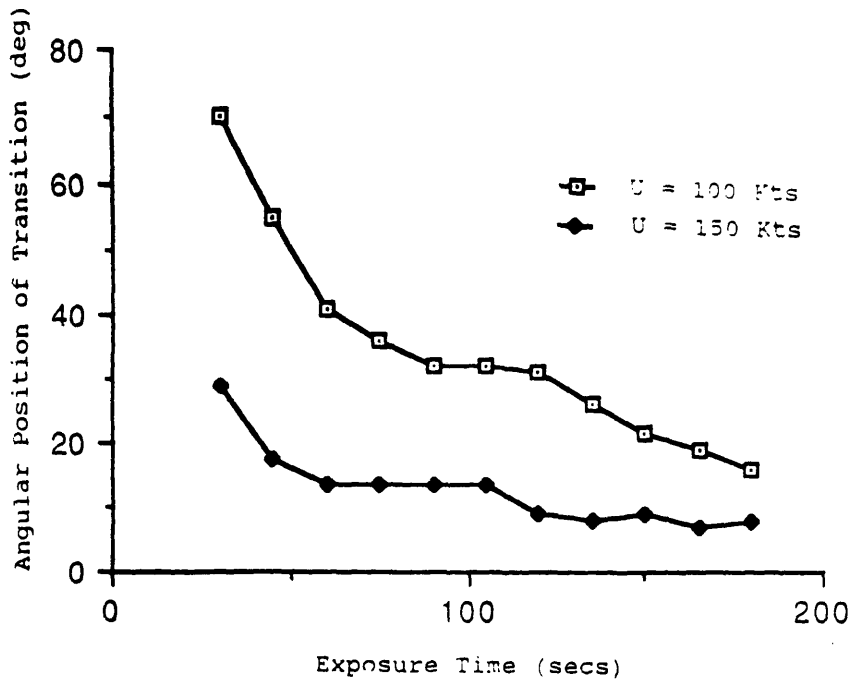
c) Variation with freestream Velocity

Figure 5-19   Angular position Time Histories for smooth-
rough transition variation with LWC, T and U

and increasing the air temperature nearer to freezing (warm temperature) moves the position of the smooth-rough transition closer to the stagnation point. The effect of high velocity, high LWC and a 'warm' air temperature is to increase the surface flux of water $\dot{M}_{out}$ out of the smooth zone. The heat transfer in the smooth zone is controlled by laminar heat convection. The fact that a higher flux of water into the rough zone causes the rough zone to occur nearer the stagnation point implies that the enhancement of heat transfer is controlled by the surface supply of water into the rough zone. The incoming water flux into the rough

110

zone is thought to control the growth and hence size of the stationary water beads which enhance heat transfer.

A larger mass flux of water in the smooth zone causes greater loss of momentum from the laminar boundary layer and the laminar-turbulent transition of the boundary layer will occur further forward. This is consistent with the rough zone being closer to the stagnation point for high mass flow in the smooth zone.
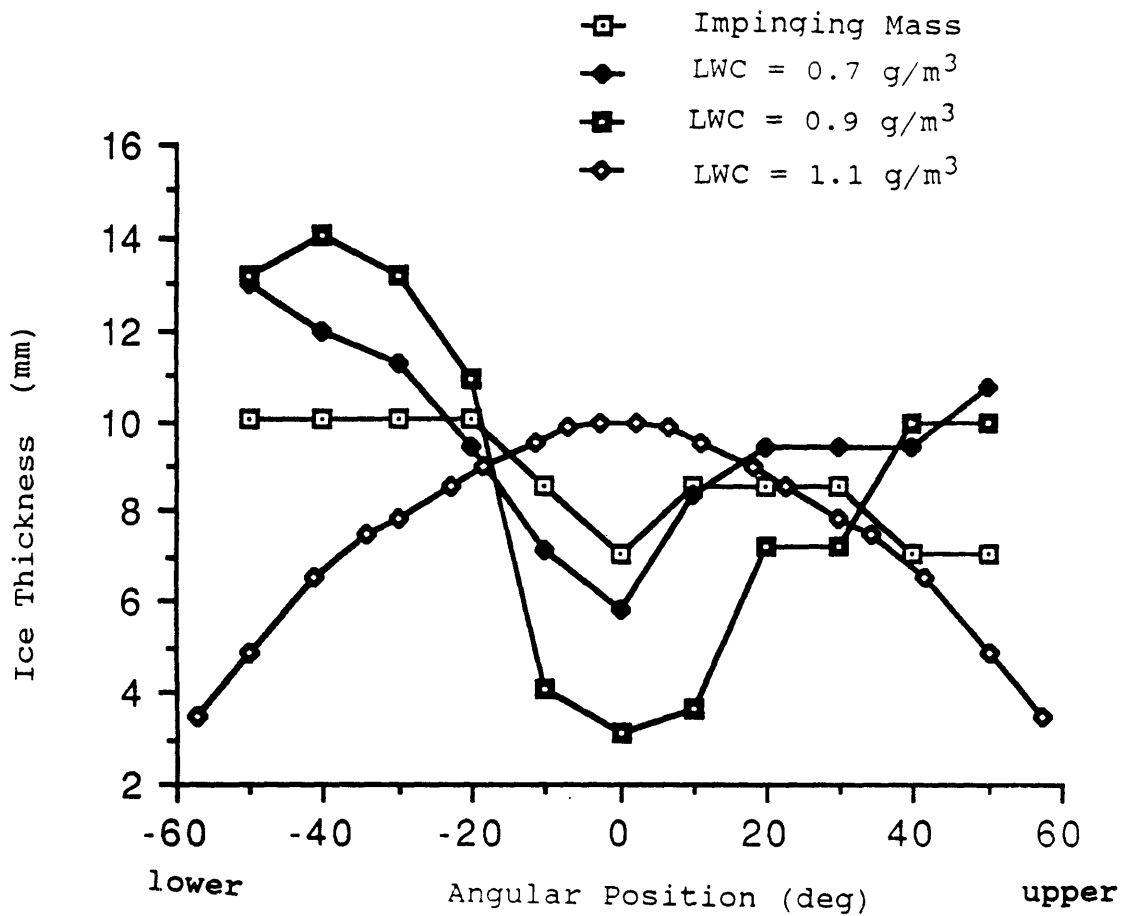
Figure 5-20   Normalised Ice Thickness variation with Angular Position for Three values of LWC and the impinging mass

111

The final distribution of frozen water for three values of liquid water content is shown in figure 5-20 where the radial thickness of ice has been normalised with the value of liquid water content and is plotted against the angular position from the stagnation point for both the upper and lower surface on the cylinder. The location of the impinging mass distribution for the three minute exposure was calculated using the procedure detailed by Lozowski [23] and is included. The particle distribution was assumed to be a Langmuir D distribution with an MVD of 30 micron. This allows a comparison to be made of where the water impacts and where it freezes. The redistribution of water from the smooth to the rough zone can be clearly seen for high liquid water contents. More water accretes for the high liquid water case as the ice accretion protrubes into the freestream and hence collects more impinging water. This result also shows that the larger the mass flux in the smooth zone the more pronounced the rough zone horns will be. This figure also clearly shows the assymetry in the ice shape produced by gravity. More ice accreting on the downward facing surface for all three cases.

The transient behavior of the smooth-rough transition was observed in section 5.5 to be dependent on the thermal response and surface resistance of the initial uniced surface. However, the transient effect on the total ice accretion washed out as the icing encounter progressed. It was also observed that the lower the surface resistance and the longer the thermal response the further forward the

transition is at a given time.

The initial rapid progression and then gradual slowing of movement of the smooth-rough transition is similar to an exponential decay behavior. The initial rapid growth of the rough zone is controlled by the time constant T of the system and its asymptotic position of the transition by the magnitude of the icing cloud parameter. For the movement of the smooth-rough transition this can be represented by:

$$P(t) = P_f + (P_o - P_f) e^{-t/T} \qquad (5-1)$$

Where P_f is the final position of the transition, P_o the initial position, $P(t)$ the position at time t, and T the time constant. The time constant for the smooth-rough transition is dependent on the surface resistance and thermal properties of the uniced surface. The lower the surface resistance and the slower the thermal response the smaller the value of T and the more rapid the initial progression of the transition.

The effect of the uniced surface roughness was different. It appeared to affect the final asymptotic position of the smooth-rough transiton rather than the transient behavior. This is thought to be due to the propagation of the trapezoidal roughness element in the rough zone ice surface which enhances heat transfer more than the frozen water beads and hence alter the heat balance which determines the location of the smooth-rough transition.

In general, the behavior of water on a glaze ice surface was observed to depend on the thermal properties,

surface resistance and roughness of the uniced surface for an initial transient period. For the conditions investigated and the cylindrical geometry used this transient period was of the order of 60 seconds.

The migration of the smooth-rough transition can be seen in the series of three photographs taken from the NASA investigation and shown as figure 5-21. The photographs are of a glaze ice surface close to the stagnation point of a representative airfoil. The individual photographs taken at 30,50 and 75 seconds show the stationary water beads in the rough zone and the movement of the transition towards the stagnation point.

Figure 5-22 is a schematic representation of the transition zone seen in the photographs. The following mechanism is proposed for the movement of the transition:

It is the stationary water beads in the rough zone which control the enhancement of the turbulent heat transfer. The larger their height the more heat transfer enhancement occurs. The growth of such beads is controlled by the surface flux of water into the rough zone. The boundary layer over the rough zone is turbulent which allows the heat transfer to be enhanced and regions of dry ice surface to be cooled below freezing so that stationary water beads can form.

In the smooth zone, heat transfer is by laminar heat convection, the magnitude of which is significantly lower than that for turbulent flow. The film flow of water causes the boundary layer to lose momentum which will influence the
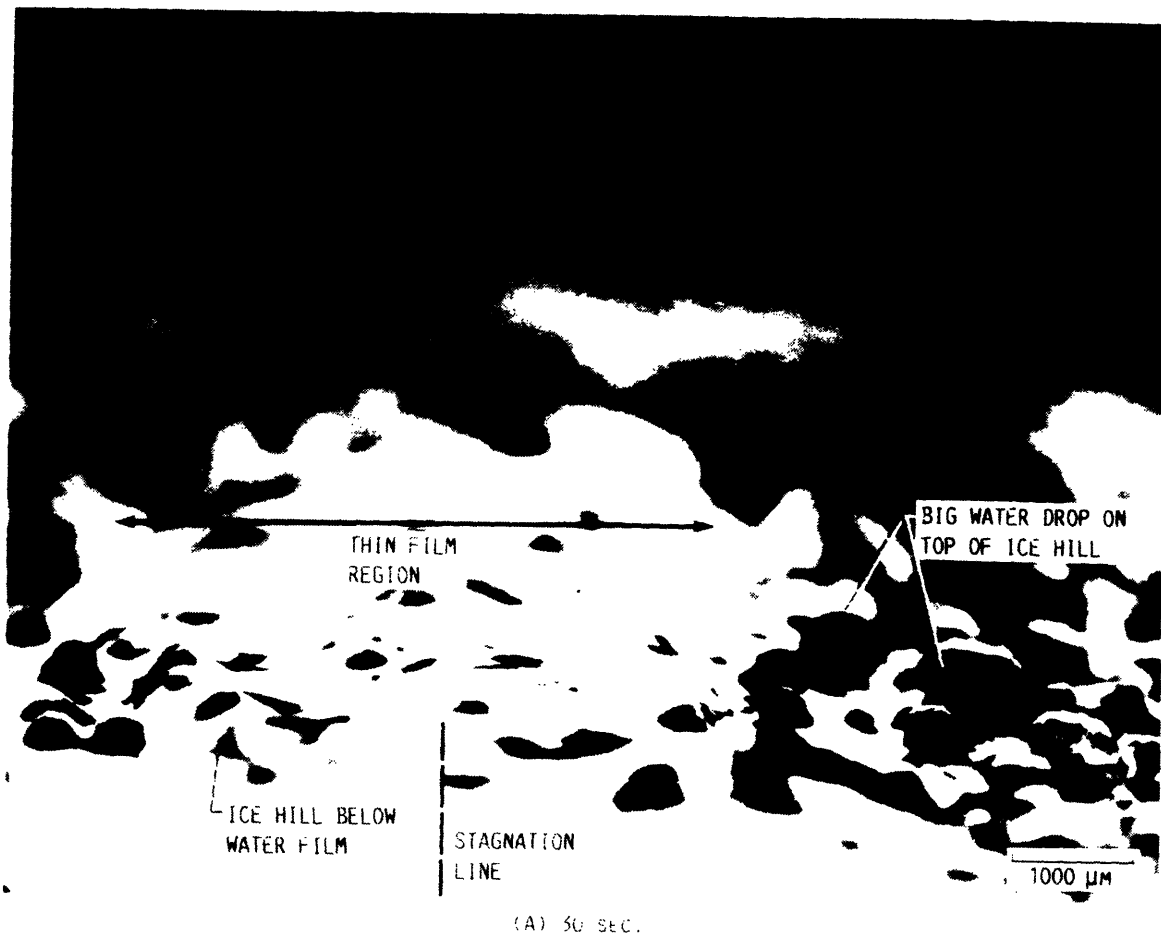
114

Labels within the figure:

THIN FILM REGION

BIG WATER DROP ON TOP OF ICE HILL

ICE HILL BELOW WATER FILM

STAGNATION LINE

1000 μM

(A) 30 SEC.

a)   T = 30 seconds

Figure 5-21   Photographs of Time Development of the
               Smooth-Rough Transition from NASA[9]

BIG WATER DROP ON
TOP OF ICE HILL

ROUGH SURFACE
SUGGESTS EXPOSED ICE

STAGNATION
LINE

1000 μM
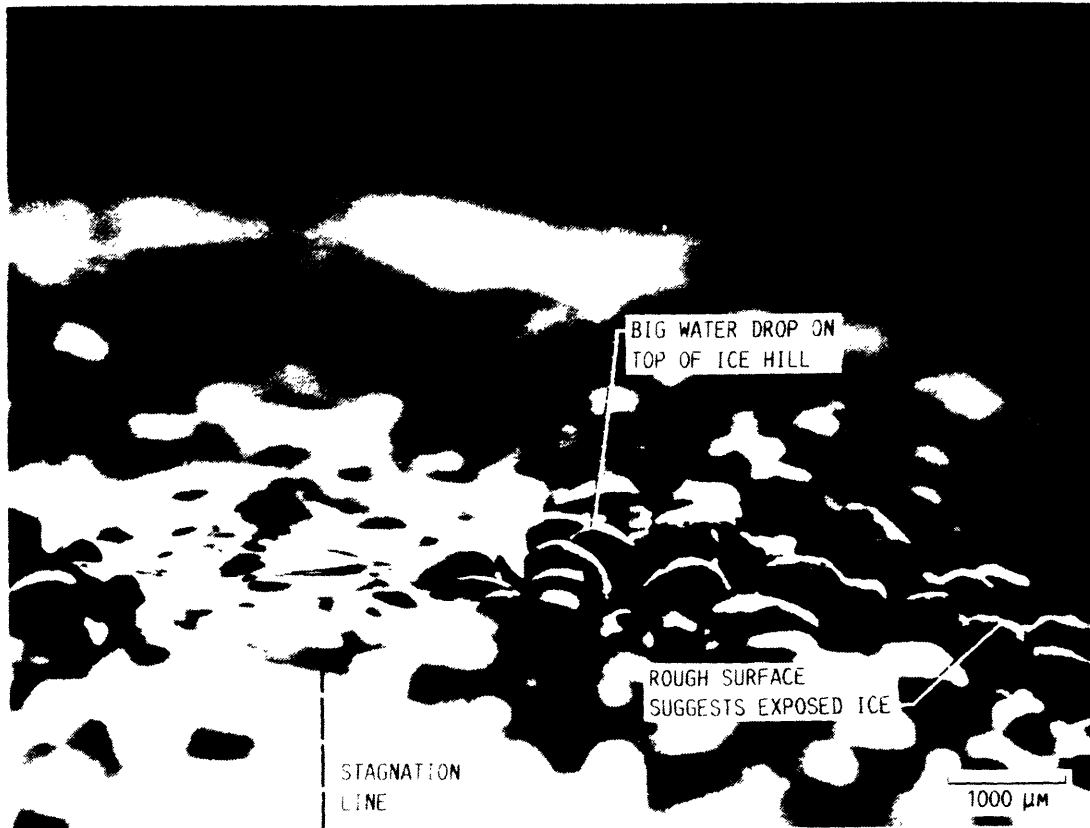
(B) 50 SEC.

b)   T = 50 seconds

Figure 5-21   Photographs of Time Development of the
Smooth-Rough Transition from NASA[9]

116

THIN FILM
REGION

STAGNATION
LINE

ROUGH SURFACE
SUGGESTS EXPOSED
ICE
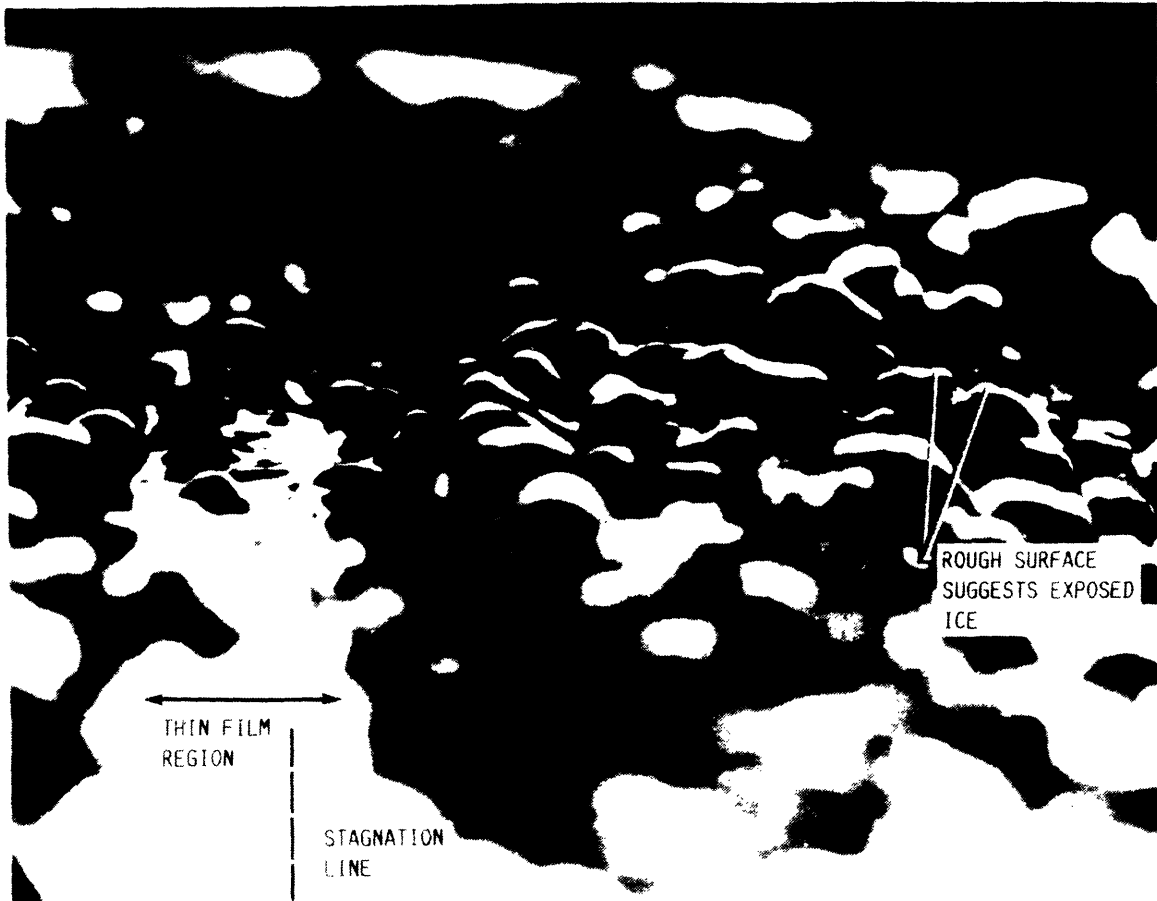
(C) 75 SEC.

c)   T = 75 Seconds

Figure 5-21   Photographs of Time Development of the
               Smooth-Rough Transition from NASA[9]

117

LAMINAR   TRANSITION   TURBULENT

h_{lam} M_{out} h_{turb}

k

Water Q_{cond} T < 0°C

0°C

$\Delta S \sim$ 1mm
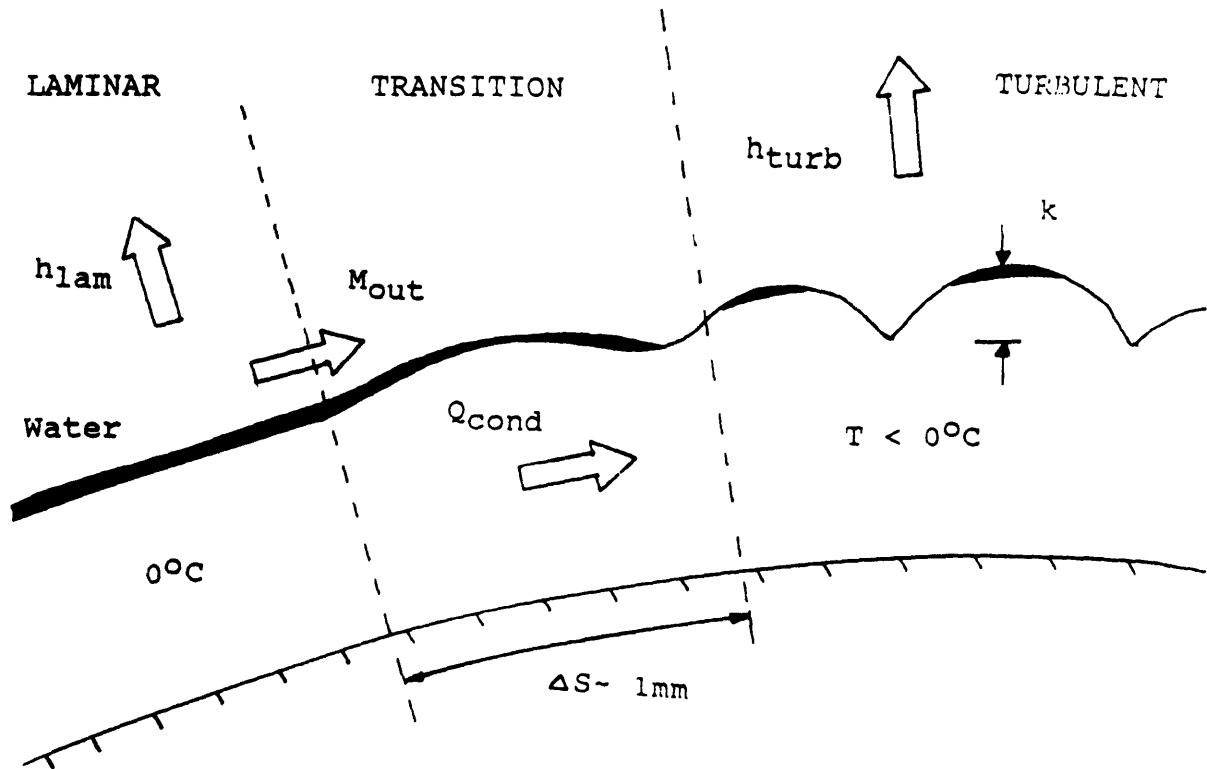
Figure 5-22   Schematic Representation of Smooth-Rough

Transition on Glaze Ice Surface

location of where the boundary layer transition occurs. The
smooth zone surface temperature is at the freezing point and
the mobility of water will not be restricted.

The discontinuity in heat transfer between the smooth and
rough zone will give rise to a streamwise temperature
gradient and heat will be conducted from the smooth to the
rough zone. This will tend to cool the ice at the edge of the
smooth zone and hence restrict the mobility of water.

The rate at which the transition will move towards the
stagnation point depends on the incoming mass flux of water

into the upstream boundary of the rough zone. The larger this term is, the greater the heat transfer required to freeze the incoming mass flux and keep the rough surface temperature below freezing. The magnitude of the heat transfer discontinuity across the transitions will be determine the cooling of the edge of the smooth zone. This discontinuity is determined by the external flowfield. This process will be initially large at the begining of the exposure and will reduce as the transition moves upstream which is consistent with the exponential decay observed.

As heat transfer enhancement requires turbulent flow there will be a Reynolds number dependence on the upstream limit for which turbulent flow can occur. Below a critical Reynolds number based on the cylinder diameter and freestream velocity the laminar boundary layer is unconditionally stable and heat transfer enhancement will not be possible.

Chapter Six

INFLUENCE OF SURFACE WATER BEHAVIOR ON GLAZE ICE ACCRETION

6.1 Introduction

The wind tunnel icing experiments showed that distinct
zones of surface water behavior occur on an accreting glaze
ice surface. Current ice accretion codes do not physically
model the water behavior on the surface and require the use
of an input roughness to attempt to match the predicted ice
shape to the real ice shape.

To illustrate this, four test cases were run[35]
using a single 180 second time step iteration with the
LEWICE[3] code and compared to the results obtained in the wind
tunnel experiments. For these simulations two values of
roughness were used. A 'smooth' value of 0.074mm to
replicate the polished aluminium surface and a 'rough' value
of k=0.3mm evaluated using the equivalent sand grain
roughness for the trapezoid element height and geometry of
the knurled surface from the data given by Schlichting. Two
air temperatures of -4.5°C and -9°C were used.

Figure 6-1 shows the comparisons for the two polished
tests. At the colder temperature the code prediction is
closer to the experimental ice shape. In both cases the
predicted position of the ice horns is located aft of the

Roughness $K_s = 0.074$ mm

LWC $=1.1$ g/m^3
U $= 77$ m/s
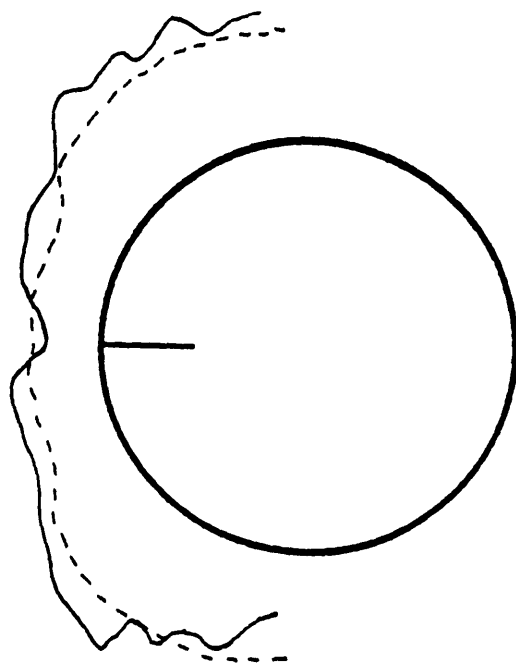
T $= - 9^\circ$ C

– – –LEWICE

———POLISH
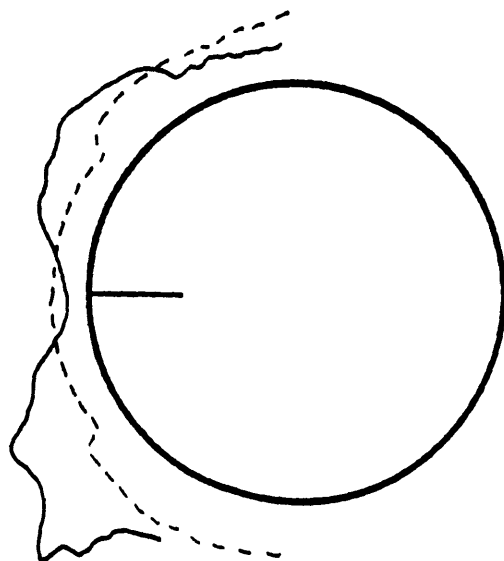
T $= - 4.5$ $^\circ$C

Figure 6-1   Final Glaze Ice Comparison for Polished
Cylinder and LEWICE at two air temperatures

experimental rough zone. This implies that the region of enhanced heat transfer, controlled by the input surface roughness, is not located correctly. The assymetry of the experimental accretion at the warm temperature can be clearly seen and is not predicted by the code. The two comparisons shown in figure 6-2 for the knurled cylinder again gave better agreement for the cold temperature when there is less surface flow. The input roughness comparable to the knurled element size in fact over predicts the heat transfer and ice accretion. In all four comparisons the code does not predict correctly the location of the smooth-rough transition.

The performance of the code in modeling the location of the smooth-rough transition which controls the ice accretion shows the difficulty in only using a single input roughness to match predicted and experimental ice shapes. The work conducted in this investigation suggests that a simple multiple zone modification to existing ice accretion models so that the physical behavior of surface water is included explicitly should improve the accuracy of glaze ice modeling.

6.2 Multiple Zone Modification To Ice Accretion Model

Observed in the direct comparison experiments were three different zones of water behavior on a glaze ice surface. The smooth zone close to the stagnation point where there is a film of water covering the ice surface; a rough zone where there is no flow downstream out of the zone and the unfrozen

Roughness K_s = 0.3 mm   LWC = 1.1 g/m^3
                                  U = 77 m/s
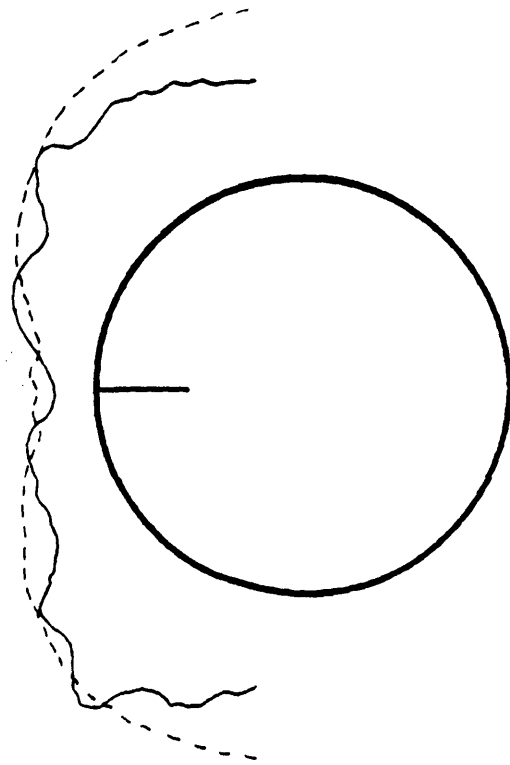
T = - 9 $^{\circ}$C

- - - - LEWICE

——— KNURL
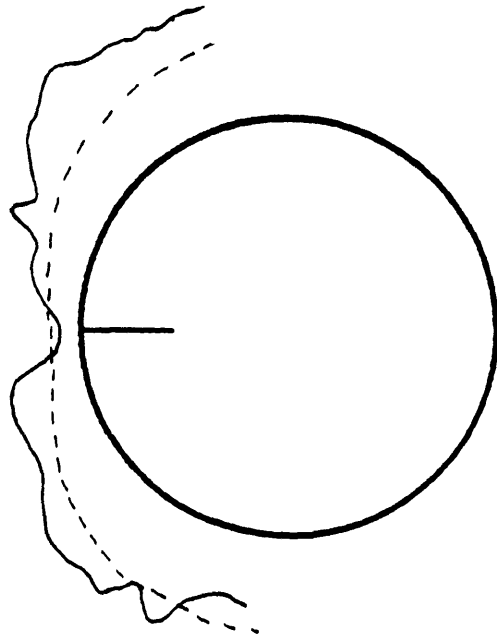
T = -4.5 $^{\circ}$C

Figure 6-2   Final Glaze Ice Shape Comparison for Knurled
               Cylinder and LEWICE at two air temperatures

water present is coalesced into stationary water beads which freeze and generate roughness; and an initial runback zone which forms prior to significant growth of the rough zone.

Based on this observed surface water behavior during glaze ice accretion, a simple modification to the existing ice accretion model is proposed which may improve the curent model's accuracy within the glaze ice regime. In this proposed "Multi-Zone" model the accreting ice surface is divided into two or more discrete zones which have varying surface water behavior and surface roughness. This is in contrast to current techniques which assume the surface has a uniform roughness and surface water runback.

In the simplest version of the model, the surface is divided into two zones. There is a smooth wet zone centered about the stagnation region where thin film runback occurs and a rough zone of enhanced heat transfer for the remainder of the accreting surface. Figure 6-3 show a schematic representation of such a two zone model. The three individual components are discussed below. A physical method of locating the position of the smooth-rough transition and of determining surface roughness in the rough zone are essential components to the implementation of the two-zone modification.

```
                  ┌─────────────────────────┐
                  │   CALCULATE  FLOWFIELD   │       STEP 1
                  │      AROUND  BODY        │
                  └─────────────────────────┘
                              │
                              ▼
                  ┌─────────────────────────┐
                  │  IMPINGING  MASS  FLUX   │       STEP 2
                  │      DISTRIBUTION        │
                  └─────────────────────────┘
                              │
                              ▼
                  ┌─────────────────────────┐
                  │         LOCATE           │
                  │     SMOOTH  ROUGH        │
  INCREMENT TIME  │       TRANSITION         │
                  └─────────────────────────┘
   t = t + Δt                 │
                              ▼
                  ┌─────────────────────────┐
                  │        CALCULATE         │
                  │  SMOOTH ZONE   Ṁfreeze   │       STEP 3
                  │    ICE ACCRETION RATE    │
                  └─────────────────────────┘
                              │  Ṁout
                              ▼
                  ┌─────────────────────────┐
                  │        CALCULATE         │
                  │  ROUGH ZONE    Ṁfreeze   │
                  │    ICE ACCRETION RATE    │
                  └─────────────────────────┘
                              │
                              ▼
                  ┌─────────────────────────┐
                  │        CONSTRUCT         │       STEP 4
                  │      NEW ICE SHAPE       │
                  └─────────────────────────┘
```
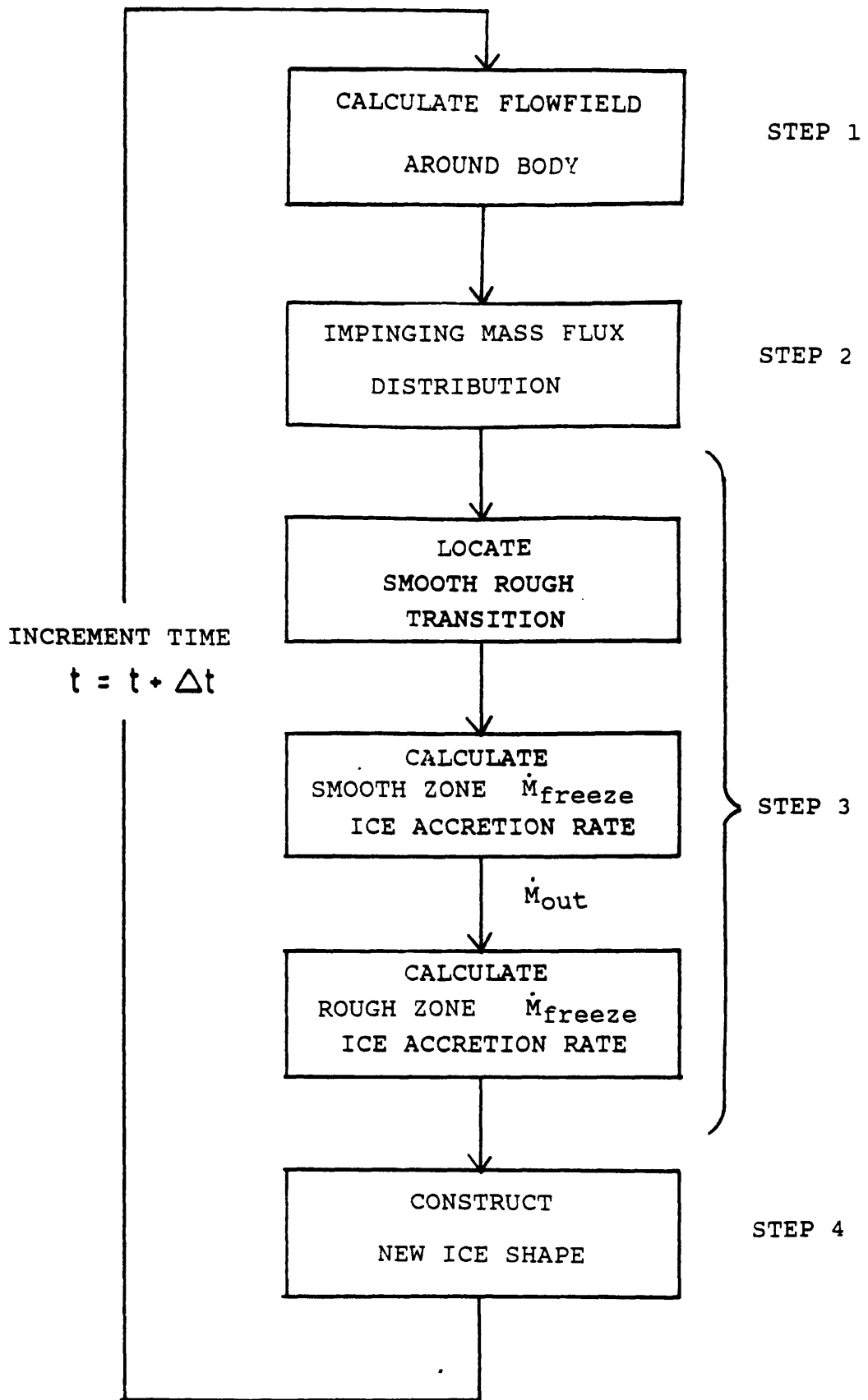
Figure 6-3   Schematic Representation of Proposed Multi-Zone
               Ice Accretion Algorithm

6.2.1 Smooth-Rough Transition

The parametric study of the final position and transient behavior of the smooth-rough transition showed that the movement of the transition was controlled by a heat and mass balance across the transition between the smooth-rough zone and its rate of progression decayed exponentially. The mass flux of water from the smooth to the rough zone controls the size and hence heat transfer enhancement in the rough zone. The magnitude of the film flow also influences the transition of the boundary layer from laminar to turbulent flow. Further work is required to quantify the behavior of the smooth-rough transition.

6.2.2 Smooth Zone

In the quasi-steady state the film flow in the smooth zone is identical to the Messinger uniform runback assumption. The surface flux out of a control volume being equal to the difference between the total incoming mass flux and the mass of ice frozen.

In the smooth zone the heat transfer is that for a smooth surface. The heat transfer by convection will not be enhanced in the smooth zone if the boundary layer flow is laminar. However, the transition to turbulent flow will be affected by the airflow above the smooth zone. As discussed in Section 2.4 transition is affected by mechanisms which cause the loss of momentum from the boundary layer. The surface of the

smooth zone covered by a film of water will have a low
effective surface roughness. However, the surface shear
stress driving the film of water will remove momentum from
the boundary layer. The larger the value of the surface
water flux the greater the loss of the momentum and the
earlier the boundary layer will transition. Dependent on the
Reynold's Number there may be an upstream limit before which
turbulent flow is not possible and heat transfer enhancement
will not occur.

6.2.3 Rough Zone

The remaining ice surface consists of a "rough" zone
where surface tension effects dominate the surface water
behavior and stationary water beads freeze and generate
roughness. The overall heat transfer within this region is
sufficient to freeze both the impinging mass flux and surface
flow out of the smooth zone. In the rough zone there is no
flow downstream so that the overall heat transfer for the
entire rough zone must be sufficient to freeze all of the
incoming mass flux which includes the impinging mass flux
within the rough zone and the surface water flux from the
smooth zone. That is:

$$\dot{M}_{freeze}{}^{r} > \dot{M}_{out}{}^{r} + \dot{M}_{imp}{}^{r} \qquad (6\text{-}1)$$

127

Where the superscript $'r'$ indicates the total amount for the rough zone. To model surface water flow in the rough zone the essential requirement is in determining the correct heat transfer coefficient. The distribution of water will determine the local ice accretion rate on the surface. The largest accretion rate will be at the smooth-rough transition where the heat transfer rate is the highest and incoming mass flux greatest. The enhancement of heat transfer will be dependent on the ratio of the roughness element height to the turbulent boundary layer thickness. As discussed in Section 4.2 and 5.7 the roughness element height will be dependent on the incoming mass flux of water and the local dry ice surface temperature. This is consistent with the mass distributions plotted as figure 5-20 in Section 5.7. In these the highest mass accretion rates and hence highest heat transfer occured in the rough zone at the wettest conditions.

How to model the distribution of water in the rough surface region is an area that requires investigation. If the location of the smooth-rough transition can be determined it may not be necessary to calculate explicitly the heat transfer coefficient as all the incoming water into the rough zone freezes. All that is necessary would be to determine the distribution of water to calculate the local ice accretion rate.

Chapter Seven

SUMMARY AND CONCLUSIONS

Chapter One gives a background discussion on the aircraft
icing problem and current methods of modeling ice accretion
for the certification of aircraft systems. The presence of
unfrozen surface water and how it is dealt with is seen to be
a contributory reason for unsatisfactory of modeling of glaze
ice accretion through the generation of surface roughness.

Local heat and mass transfer on a glaze ice surface
is analysed in Chapter Two. The heat transfer coefficient h
is the most important variable in determining the local ice
accretion rate. The magnitude of the heat transfer
coefficient is dependent on whether the local flow is laminar
or turbulent. In turbulent flow the heat transfer will be
significantly enhanced by the presence of surface roughness.
The roughness of a glaze ice surface controls the heat
transfer enhancement and current codes use empirical matching
techniques to evaluate its value and this introduces errors
into the prediction of ice accretion.

The flux of water along the ice surface is discussed in
Chapter Three. Four possible modes of surface transport are
flow as a film,rivulets, bead and stationary water are
presented. The forces which determine the mode of transport
are external forces due to acceleration, flow induced

pressure gradients and surface shear stress which act on the water and are opposed by the surface resistance to motion of the water. The relative strengths of the surface resistance and external force will determine the particular mode of transport. The surface resistance to motion is dependent on the contact angle, contact angle hysteresis and surface tension of the water. If the surface resistance is large compared to the external force acting stationary water beads will occur.

In Chapter four the surface resistance of water was investigated. Measurements were made of contact angle and contact angle hysteresis for water on ice for a range of ice surface temperatures between $0^{\circ}C$ and $-15^{\circ}C$. There was a strong variation for θ and $\Delta\theta$ with ice surface temperature. The corresponding increase in surface resistance as the ice temperature is decreased below freezing which allows the presence of stationary water beads on an ice surface. The subfreezing temperature of the dry ice surface surrounding a water bead provides sufficent resistance to prevent its motion. The freezing of stationary water beads is the mechanism which generates a rough surface during glaze ice accretion. This was seen in observations made from a NASA investigation of glaze ice surface behavior.

The maximum size of stationary water beads was measured for uniform flow over a flat plate boundary layer in which the only external force was a surface shear stress in order to determine the influence of surface resistance. An approximate relationship was established which gave a power

law dependence between the droplet diameter and the material surface resistance.

Direct comparison experiments on 1" diameter cylinders in an icing wind tunnel described in Chapter five. These experiments allowed detailed observations to be made of the development of glaze ice surfaces and how it is influenced by the icing cloud conditons and the initial uniced cylinder. The glaze ice surface was observed to have distinct zones of surface water behavior. They were: a smooth wet zone in the stagnation zone where thin film runback of water occured; a rough zone where surface resistance causes coalescence of the surface water into beads; and a runback zone where surface water ran back as rivulets. The location of the transition point between the smooth and the rough zone was seen to migrate with time towards the stagnation point. The rate of migration decreased exponentially with time and was its position during a transient period dependent on the surface resistance and thermal properties of the initial uniced surface. Its final asymptotic position depended on the icing cloud parameters which control the mass flow of water in the smooth zone. The larger this mass flux the further forward the rough zone propagated.

The freezing of the coalesced water beads in the rough zone generated a characteristic rough surface and caused enhanced heat transfer. The size the beads grow to will depend on the incoming mass flow and the heat transfer enhancement they induce which controls the rate at which they freeze.

Other observations made were the following. For an initially uniced knurled surface the roughness geometry was observed to propagate on the rough zone ice surface.

Large variations in ice accretions was seen when the surface tension of the water was changed. This provide additional evidence for the importance of surface water behavior to glaze ice accretion. For warm conditions there was a noticeable assymetry in the accreted ice. More ice forming on the lower surface of the cylinder. This was due to the effect of gravity on the flow of water in the smooth zone.

Based on this investigation a simple multiple zone modification to the current glaze ice accretion model is proposed. The component parts of the model are discussed in Chapter 6. The model incorporates discrete zones of surface water behavior each with a characteristic surface roughness.They are as follows:

1) A smooth zone close to stagnation zone where unfrozen water runsback as a thin film. The dynamics of the film are controlled by the gravitational, pressure gradients and surface shear stress forces. The heat transfer coefficient is that for laminar flow. This is equivalent in current models, for steady state icing, to the Messinger approximation of uniform runback. The mass flux of water flowing along the surface controls the transition of the boundary layer from laminar to turbulent flow.

2) A rough zone where all the water entering the rough

zone, either from the smooth zone or direct impingement of cloud droplets, coalesce as stationary beads which freeze. Heat transfer is by turbulent convection enhanced by the roughness caused by the stationary water beads. The amount of heat transfer enhancement possible is dependent on the airstream velocity, temperature and liquid water content. The heat and mass balance across the smooth-rough transition will determine its location and the rate at which it moves.

The limitations to the conclusions obtained in this investigation are that the results are based on glaze ice accretions formed on a small 1" diameter cylindrical geoemetry at two Reynolds number. The transient behavior of more aerodynamic bodies could well be different. The larger the downstream distance over which surface flow occurs may make a significant difference to the migration of the transition. The limited range of glaze ice conditions investigated allowed trends to be observed but not exactly defined. The calibration and accuracy of icing wind tunnel used will make the results, although self consistent, difficult to match accurately with other work.

In conclusion, the surface water behavior on a glaze ice surface was seen to control the location of distinct zones of ice surface each with a characteristic roughness and mechanism of heat transfer. The freezing in the smooth zone near to the stagnation point was by laminar heat convection and the film flow of water was important in determining the location of the rough zone. In the rough zone the freezing

of stationary water beads generate a rough surface which
enhance turbulent heat transfer and allowed greater ice
accretion to occur.

REFERENCES

1. Bragg, M.B., Gregorek, G.M., and Shaw, R.J.," An Analytical Approach to Airfoil Icing", AIAA Paper 81-0403, January 1981

2. MacArthur, C.D. ,"Numerical Simulation of Airfoil Ice accretion.", AIAA Paper 83 0112, January 1983.

3. Ruff, G.A., "Development of an analytical ice accretion prediction method (LEWICE)."Sverdrup Technology, Inc., LeRC Group Progress Report, February 1986.

4. Chang, H-P.,and Kimble, K.R.,"Influence of Multidroplet Size Distribution on Icing Collection Efficiency", AIAA-83-0110, January 1983.

5. Kirby, M.S.," An experimental and theoretical study of the ice accretion process during artificial and natural icing conditions", S.M. Thesis, M.I.T. May 1986.

6. Messinger, B.L.,"Equilibrium Temperature of an Unheated Icing Surface as a Function of Airspeed" Journal of the Aeronautical Sciences, Jan.1953, pp24-42.

7. Ludlam, F.H.," The Heat Economy of a Rimed Cylinder," Quarterly Journal of the Royal Meteorological Society, Vol 77, 1951, pp. 663-666.

8. Macklin, W.C. and Payne, G.S.," A Theoretical study of the Ice Accretion Process", Quarterly Journal of the Royal Meteorological Society, Vol 93, 1967 pp. 195-213

9. Olsen, W.A., and Walker, E.,"Experimental Evidence for Modifying the Current Physical Model for Ice Accretion on Aircraft Structures", NASA TM 87184.

10. Kirby, M.S., and Hansman, R.J.," Experimental Measurements of Heat Transfer from an Iced Surface During Artificial and Natural Cloud Icing Conditions", AIAA 86-1352, June 1986.

11. Rohsenow, W.M., Choi H.Y.,"Heat, Mass and Momentum Transfer", Prentice-Hall, 1961.

12. Kirchner, R.D.,"" Aircraft Icing Roughness features and Its Effect on the Icing Process.", AIAA 83 0111, January 1983.

13. Van Fossen G.J., Simoneau, R.J., Olsen, W.A., and Shaw,R.J," Heat Transfer Distributions Around Nominal Ice Accretion Shapes Formed on a Cylinder in the NASA Lewis Icing Research Tunnel", AIAA Paper 84-0017, January 1984.

14. Smith, A.M.O., and Clutter, D.W.," The smallest height of roughness capable of affecting boundary-layer transition", <u>Journal of Aeronautical Science</u>, 26, 229-256.

15. Von Doenhoff, A.E., Horton, E.A., " A Low-Speed Experimental Investigation of the Effect of Sandpaper Type of Roughness on Boundary Layer Transition", NACA TN 3858, 1956.

16. Simpson, R.L.," A Generalised Correlation of Roughness Density Effects on the Turbulent boundary layer", <u>AIAA Journal</u>, Vol. 11, 1973.

17. Nikuradse, J.,"Stromungsgesetze in Rauher Rohren", VDI-Forsehungsheft 361 (1933). (also" Laws of Flow in Rough Pipes", NACA TM-1292).

18. Schlichting, H.," Boundary Layer Theory", 7th Ed., McGraw Hill, 1979.

19. Coleman, H.W., Hodge, B.K., Taylor, R.P., " A Re-Evaluation of Schlichting's Surface Roughness Experiment", <u>Journal of Fluids Engineering</u>, Vol. 106, March 1984, pp.60-65.

20. Ed., Good R.J., Stromberg, R.R., " Surface and Colloid Science", Plenum, Vol 11, 1979.

21. Bandyopadhyay, P.R., "Rough-wall turbulent boundary layers in the transition regime", <u>Journal of Fluid Mechanics</u>, Vol. 180, 1987, pp.231-266.

22. Gent, R.W., Cansdale, J.T.," The development of Mathematical Techniques for Helicopter Rotor Icing," AIAA Paper 85-0336, Jan. 1985.

23. Lozowski, E.P., Stallabrass, J.R., Hearty, P.F., "The Icing of an Unheated Non-Rotating Cylinder in Liquid Water Droplet - Ice Crystal Clouds", National Research Council of Canada (NRC) Report LTR-LT-86, Feb 1979.

24. Achenbach, E.," The Effect of Surface Roughness on the Heat Transfer from a Circular Cylinder to the Cross Flow of Air," <u>International Journal of Heat and Mass Transfer</u>, Vol 20, 1977, pp. 359-369.

25. Zuber, N., Staub, F.W.," Stability of Dry Patches Forming in Liquid Films Flowing over Heated Surfaces.", <u>International Journal of Heat and Mass Transfer</u>, Vol 9, 1966, pp897-905.

26. Young, T., Philosophical Transactions of thhe Royal Society, (London), 95, 65 (1805).

27. Ed. Matijevic, E.,"Surface Colloid Science Vol. 2",
    Wiley, 1969, pp85-115.

28. Dussan V, E.B., Chow, R.T.," On the ability of drops
    to stick to non-horizontal surfaces of solids. ", <u>Journal
    of Fluid Mechanics</u>, Vol. 137, 1983, pp.1-39.

29. Dussan V, E.B.," On the ability of drops to stick to
    non-horizontal surfaces of solids. Part 2. Small drops or
    bubbles having contact angles of arbitary size.", <u>Journal
    of Fluid Mechanics</u>, Vol. 151, 1985, pp.1-20.

30. Dussan V, E.B.," On the ability of drops to stick to
    surfaces of solids. Part 3. The influence of the motion
    of the surrounding fluid on dislodging drops.", <u>Journal
    of Fluid Mechanics</u>, Vol. 174, 1987, pp.381-397.

31. Batchelor, G.K., "An Introduction to Fluid Dynamics",
    Cambridge University Press, 1967.

32. Greiner, C.M., "The statics and dynamics of sessile
    bubbles on inclined surfaces", S.M. Thesis, M.I.T., June
    1985.

33. Hobbs, P.V.," Ice Physics", Oxford University Press,
    1974.

34. Duncan, W.J., Thom, A.S., Young, A.D.,"Mechanics of
    Fluids", 2nd Ed. Edward Arnold, 1970

35. Riley J., Safety Analysis Branch, Frederal Aviation
    Administration Technical Center.

FILM FLOW WITH WATER IMPINGMENT AND FREEZING
TRANSPORT EQUATIONS

Consider the Control Volume shown as figure 3-2. The thickness of the water film t at a given downstream position s is given by t(s) where t is only a function of position and the flow is steady , or only changing slowly and can be considered as quasi-steady. The force balance on an element at height y in the film which has a thickness dy and length ds is shown as A-1:

$$dyds(d\Upsilon/dy - dp/dx) \quad - \quad g\sin\phi\ dsdy = 0 \qquad \text{A-1}$$

Where ϕ is the angle the surface makes to the horizontal and Υ is the shear stress at y. The shear stress is the product of the local velocity gradient and the water's dynamic viscosity shown as A-2:

$$\Upsilon \quad = \quad \mu_{water}\ dU/dy \qquad \text{A-2}$$

Substituting into A-1 and integrating with respect to y twice and then applying the boundary conditions that:
1) The velocity at the surface is zero (no-slip) U(0)=0
2) The shear stress is continuous across the water-air interface and the local curvature is small so that

$$\mu_{air}\ dU(t)/dy|_{air} = \mu_{water}\ dU(t)/dy|_{water} \qquad \text{A-3}$$

This gives the velocity at height y and downstream position s for a film of thickness t as:

$$U(y) = \frac{1}{\mu_{water}}\left(\frac{y^2}{2} - t\,y\right)\left(\left(\frac{dp}{dx}\right) + g\sin\phi\right) + \frac{\mu_{air}}{\mu_{water}}\frac{y}{}\left.\frac{dU(t)}{dy}\right|_{air} \qquad \text{A-4}$$

The mass flux at s is simply the integral of A-3 over the thickness of the film t multiplied by the water density.

$$M_{in} = \int_{o}^{t} \rho\ U(y)\ dy = \frac{t^2\rho}{\mu_{water}}\left(\frac{\mu_{air}}{2}\left.\frac{dU(t)}{dy}\right|_{air} - \frac{t}{3}\left(\frac{dp}{ds} + g\sin\phi\right)\right) \qquad \text{A-5}$$

To determine how the thickness of the film changes with position s and the actual thickness it is necessary to consider the Mass balance given as 2-3. As the mass flux of water out of the control volume $\dot{M}_{out} = \dot{M}_{in} + d(\dot{M}_{in})/ds$ s. The mass balance can be written in the limit as s 0:

$$d(\dot{M}_{in})/ds \quad = \quad \dot{M}''_{imp} - \dot{M}''_{freeze} \qquad \text{A-6}$$

Differentiating A-5 with respect to s , substituting into A-6 and rearranging to give the rate of change of thickness dt/ds with position gives A-7. As the rate of change of air velocity gradient is small this term has been neglected.

$$\frac{dt}{ds} = \frac{\dot{M}''_{imp} - \dot{M}''_{freeze} - \frac{t^3\rho}{\mu_{water}}\left(\frac{d^2p}{ds^2} + g\cos\phi\frac{d\phi}{ds}\right)}{\frac{t\rho}{\rho_{water}}\left(\frac{\mu_{air}}{2}\left.\frac{dU(t)}{dy}\right|_{air} - \left(t\left(\frac{dp}{ds} + g\sin\phi\right)\right)\right)} \qquad \text{A-7}$$

APPENDIX II

DIRECT COMPARISON TESTS CONDUCTED IN DATA PRODUCTS ICING WIND TUNNEL

Test Articles Designation   Material/Surface

St=Standard Aluminum/Gloss Acrylic
Px=Plexiglass/Gloss Acryllic
Po=Aluminum/Polished
Kd=Aluminum/Knurled
Mt=Aluminum/Matt Acrylic
Wx=Aluminum/Waxed
Sc=Aluminum/Scale 1/2" O.D.

Individual Tests

#	TIME (min)	ICING CLOUD T °F	LWC g/m³	Vel Kts	CYLINDERS (Camera) B	C	COMPARISON
1	3.5	22	1.15	143	Cu	Px	Thermal
2	3	24	1.14	143	Mt	Wx	Resistance
3	3	25	1.09	149	Wx	Mt	Resistance
4	3	24	1.07	153	St	St	
5	3	24	1.09	150	Po	Kd	Rough
6	3	24	1.14	143	Kd	Po	Rough
7	4	25	0.64	142	Kd	Po	Rough
8	4	24	0.89	143	Kd	Po	Rough
9	4	23	0.85	149	Po	Kd	Rough
10	4	25	0.82	154	Cu	Px	Thermal
11	4	25	0.87	146	Mt	Wx	Resistance
12	3	25.5	0.84	152	Mt	St	Resistance
13	3	26	0.82	155	St	Mt	Resistance
14	4	24	0.83	154	Sc	St	Scale
15	3	21	1.15	142	Kd	Kd	Roughness
16	3	21.5	1.10	149	Po	Po	Roughness
17	3	25.5	1.16	141	Kd	Kd	Roughness
18	3	23.5	1.11	147	Kd	Kd	Roughness
19	3	23	1.07	153	Px	Cu	Thermal
20	3	23.5	1.08	151	Px	St	Thermal
21	3	16	1.13	144	Px	Cu	Thermal
22	2	17	1.13	144	Cu	Px	Thermal
23	2	15	1.17	139	Kd	Po	Roughness
24	2	16	1.10	149	Po	Kd	Roughness
25	2	16.5	1.10	148	St	Mt	Resistance
26	2	16	1.10	149	Mt	St	Resistance
27	2	15	1.11	148	Px	St	Thermal
28	3	17	1.18	138	Kd	Kd	Roughness
29	1	15	1.11	147	Kd	Kd	Roughness
30	2	17	1.11	147	Wx	Mt	Resistance
31	2	17	1.10	148	Mt	Wx	Resistance
32	2	16.6	1.09	149	Po	Po	Roughness
33	2	24	1.45	113	Cu	Px	Thermal
34	2	22	1.52	107	Px	Cu	Thermal

35	2	24	1.60	102	Kd	Po	Rough
36	2	23	1.50	109	Mt	St	Resistance
37	2	22	1.48	110	Mt	Wx	Resistance
38	3	23	1.16	109	Px	Cu	Thermal
39	3	23	1.22	104	Kd	Po	Rough
40	3	23	1.18	108	Mt	St	Resistance
41	3	23	1.18	108	Mt	Wx	Resistance
42	3	14.5	1.19	106	Px	Cu	Thermal
43	3	13	1.19	107	Cu	Px	Thermal
44	3	15	1.23	103	Kd	Po	Rough
45	3	13	1.21	105	Mt	St	Resistance
46	3	15	1.21	105	Mt	Wx	Resistance
47		Conditions Not Constant					
48	3	25	0.7	156	Cu	Px	Thermal
49	3	24.5	0.66	165	Px	Cu	Thermal
50	3	25	0.67	163	Mt	St	Resistance
51	3	25	0.68	160	Po	Kd	Rough
52	3	25	0.67	163	Mt	Wx	Resistance
53	3	23	0.67	163	Px	St	Thermal
54	5	15	0.67	161	St	St	
55	2	23	0.84	163	Cu	Px	Thermal
56	2	24	0.84	164	Cu	Px	Thermal
57	3	22	0.95	162	Cu	Px	Thermal
58	3	22	1.01	152	Kd	Po	Rough
59	3	22	0.94	165	Sc	St	Scale
60	3	22	0.94	163	Mt	St	Resistance
61	3	23.5	0.94	164	Mt	Wx	Resistance
62	3	24	0.95	162	Cu	Px	Surfactant
63	3	21	1.0	155	Kd	Po	Surfactant
64	3	22	0.95	163	Mt	St	Surfactant
65		Conditions Not Constant					
66	3	22.5	0.94	165	Sc	St	Surfactant
67	3	24	0.94	164	Wx	Mt	Surfactant
68	3	17	0.97	159	Cu	Px	Surfactant
69	3	16	0.97	159	Kd	Po	Surfactant
70	3	15	0.95	162	Mt	St	Surfactant
71	3	17	0.95	163	Sc	St	Surfactant
72	3	18	0.97	160	Wx	Mt	Surfactant
73	3	21	0.96	162	Cu	Px	Surfactant
74	3	20	0.97	159	Kd	Po	Surfactant